

Mari Sofie Skomedal

Improving quantitative EDS of III-V heterostructure semiconductors in low voltage STEM

Master's thesis in Nanotechnology
Supervisor: Antonius T.J. van Helvoort
June 2022

NTNU
Norwegian University of Science and Technology
Faculty of Natural Sciences
Department of Physics



Norwegian University of
Science and Technology

Mari Sofie Skomedal

Improving quantitative EDS of III-V heterostructure semiconductors in low voltage STEM

Master's thesis in Nanotechnology
Supervisor: Antonius T.J. van Helvoort
June 2022

Norwegian University of Science and Technology
Faculty of Natural Sciences
Department of Physics

Abstract

Quantitative compositional analysis in energy dispersive X-ray spectroscopy (EDS) integrated in scanning transmission electron microscopes (STEM) is commonly based on the Cliff-Lorimer ratio method. Although practical, this method is significantly limited by the use of calculated sensitivity factors. To improve the accuracy, a factorless approach was recently suggested for ternary III-V heterostructure semiconductors named Internal composition determination (ICD). In this work, quantitative EDS of III-V heterostructures is done by applying ICD at low voltages (5-30 kV) typical for SEMs for the first time. Additionally, the analysis is refined by characterizing the EDS detection set-ups with a NiO sample prior to quantification. Three STEM set-ups are used, namely the Jeol JEM2100 and Jeol JEM2100F with an Oxford X-Max 80 detector at 200 kV, and the Hitachi SU9000 with an Oxford Ultim Extreme 100 mm² detector at 5-30 kV. All analysis is done in open-source python library HyperSpy and the applied code is included.

Characterization of the EDS detection systems reveals Cu_{K α} and Fe_{K α} stray peaks and internal fluorescence Si_{K α} peaks in all recorded data. Additionally, the SU9000 has a high degree of Al and Au strays due to the used holder. The detectors have the expected energy resolution of ~ 130 eV, and a channel size of ~ 10 eV. Shadowing of the detectors is observed up to tilt angles of 15°. These results indicate, especially for the SU9000 and the 2100F that the setup can be optimized by repositioning the detector or having optimized holders for EDS studies. The Al stray is deteriorating quantitative analysis of AlGaAs based heterostructures. Post-processing routes to handle the Al stray artifacts are discussed. A general Jupyter Notebook for EDS detector characterization with a NiO thin film was developed.

ICD quantification was successfully implemented on EDS data taken in a low voltage STEM and thin specimens. For an axially heterostructured GaAs/GaAsSb nanowire, sensitivity factors, concentration profiles, and relative thickness profiles are calculated with minimal input parameters. Concentration profiles show a periodic increase in Sb content within each GaAsSb insert layer to a maximum Sb concentration value. ICD as it is currently implemented, performs less well than at 200 kV as the predicted composition fluctuates more than observed for Cliff-Lorimer on the same data sets for different voltages and tilts. A possible cause is the noise in the data, which requires denoising prior to ICD and optimizing the algorithm.

Sammendrag

Kvantitativ sammensetningsanalyse i energidispersiv røntgenspektroskopi (EDS) integrert i sveipetransmisjonselektronmikroskopier (STEM) er vanligvis basert på Cliff-Lorimer som er en forholdsbasert metode. Selv om den er anvendelig, begrenses denne metoden betydelig av bruken av beregnede sensitivitetsfaktorer. For å forbedre nøyaktigheten har en faktorløs tilnærming nylig blitt foreslått for ternære III-V heterostrukturerte halvledere kalt Intern sammensetningsbestemmelse (ICD). I dette arbeidet blir kvantitativ EDS av III-V heterostrukturer gjort ved å anvende ICD, for første gang på lave spenninger (5-30 kV) typiske for SEM. I tillegg blir metoden tilpasset ved å karakterisere EDS-deteksjonsoppsettene med en NiO prøve i forkant av kvantifiseringen. Tre STEM oppsett blir brukt, nemlig Jeol JEM2100 og Jeol JEM2100F med en Oxford X-Max 80 detektor på 200 kV, og en Hitachi SU9000 med en Oxford Ultim Extreme 100 mm² detektor på 5-30 kV. All analysen er gjort i det Python baserte åpne kildebiblioteket HyperSpy og den anvendte koden er inkludert.

Karakterisering av EDS-deteksjonsoppsettene avdekker kunstige topper fra Cu K_{α} og Fe K_{α} , og intern fluorescens topp for Si K_{α} i alle registrerte data. I tillegg har SU9000 en høy grad av kunstig Al- og Au-stråling på grunn av den brukte holderen. Detektorene har en forventet energiopløsning på ~ 130 eV, og en kanalstørrelse på ~ 10 eV. Skyggelegging av detektorene blir observert for helningsvinkler opp til 15°. Disse resultatene indikerer, spesielt for SU9000 og 2100F, at oppsettet kan optimeres ved å endre posisjonen til detektoren eller optimere holdere for EDS studier. Den kunstige Al-strålingen forverrer kvantitativ analyse av AlGaAs-baserte heterostrukturer. Rutiner for etterprosessering for å håndtere Al-strålingen blir diskutert. En generell Jupyter Notebook for EDS detektor karakterisering med en NiO tynn film har blitt utviklet.

Vellykket implementering av ICD kvantifisering ble gjort på EDS data tatt i en lav-spennings STEM og tynne prøver. Sensitivitetsfaktorer, konsentrasjonsprofiler og relative tykkelsesprofiler ble beregnet for aksielle heterostrukturerte GaAs/GaAsSb nanotråder. Konsentrasjonsprofilene viser periodisk økning i innhold av Sb innenfor hvert GaAsSb lag til en maksimum konsentrasjonsverdi av Sb. ICD presterer, slik det er implementert for øyeblikket, mindre bra enn på 200 kV, ettersom de predikerte sammensetningene varierer mer enn det som er observert med Cliff-Lorimer på samme datasett for ulike spenninger og helningsvinkler. En mulig årsak er støy i dataen, noe som krever støyreduksjon før ICD og optimering av algoritmen.

Preface and acknowledgements

This master thesis is my final work for the 5-year Master of Science (MSc) in Nanotechnology, with specialization within Nanoelectronics, at the Norwegian University of Science and Technology (NTNU). The work presented in this report has been carried out from January to June of 2022 at the TEM Gemini Center at the department of physics, the NORTEM Facility and NTNU Nanolab. Thanks to the Research Council of Norway for supporting the national infrastructures NORTEM, project number 197405, and NorFab, project number 245963. All experimental data collection has been performed by me, unless otherwise stated. The heterostructures were grown by D. Ren and M. Munshi at IES at NTNU, the TEM specimens were prepared by J.S. Nilsen and the data from Jeol JEM2100F were recorded by A.T.J. van Helvoort, who also helped setting up the STEM at the Jeol JEM2100.

There are several people that have made this thesis possible. First of all, I would like to thank my supervisor Prof. Antonius T. J. van Helvoort. His extensive knowledge and enthusiasm for this topic has motivated and guided me throughout this entire work. Without exception, I have always left our weekly meetings with new excitement and understanding of the subject.

I would also like to thank the engineers and technical staff that have given me excellent training and guidance on the instruments i have used during this work. This includes Emil Christiansen and Bjørn Gunnar Soleim at the TEM Gemini Center who have thought me almost everything I know about the Jeol JEM2100, and Verner Håkonsen at NanoLab who have always come to my rescue down in the cleanroom and helped me with the Hitachi SU9000 S(T)EM.

Thank you to my parents and my sister for your constant support. I also want to thank Timini Kull17 for our last five years together. Thank you all, this masters degree would not have been a reality without any of you.

Mari Sofie Skomedal

Mari Sofie Skomedal

Trondheim, 20.06.22

Abbreviations

AEM	Analytical electron microscope
BF	Bright-field
BFP	Back focal plane
BSE	Backscattered electron
C-L	Cliff-Lorimer
DP	Diffraction pattern
EDS	Energy dispersive X-ray spectroscopy
EELS	Electron energy loss spectroscopy
FCC	Face-centered cubic
HT	High tension
HV	High voltage
ICD	Internal Composition Determination
LED	Light-emitting diode
LV	Low voltage
MBE	Molecular beam epitaxy
NW	Nanowire
OA	Optic axis
PCA	Principal component analysis
SADP	Selected area diffraction pattern
SE	Secondary electrons
SEM	Scanning electron microscope
SDD	Si-drift detector
STEM	Scanning Transmission electron microscope
TEM	Transmission electron microscope
UHV	Ultra-high vacuum
VLS	Vapour-liquid-solid
ZB	Zinc blende

Table of Contents

Abstract	i
Sammendrag	iii
Preface and acknowledgements	v
Abbreviations	vii
1 Introduction	1
2 Theory	4
2.1 Semiconductor materials	4
2.1.1 III-V semiconductors	4
2.1.2 Heterostructured GaAs-based NWs	6
2.2 Energy dispersive X-ray spectroscopy	11
2.2.1 X-ray generation	12
2.2.2 EDS detection and system	19
2.2.3 Quantitative EDS	22
2.2.4 EDS setup and detector characterization	27
2.3 Crystallography	32
2.3.1 Crystal structures	32
2.3.2 Reciprocal lattice	35
2.3.3 Diffraction	35
2.4 Electron microscopy	39
2.4.1 Scanning electron microscope	40

2.4.2	Transmission electron microscope	42
2.4.3	Scanning transmission Electron Microscope	45
3	Experimental	47
3.1	Material and specimen	47
3.1.1	NiO thin film on Mo grid	47
3.1.2	Axial heterostructure GaAs/GaAsSb NWs	47
3.1.3	Radial heterostructure GaAs/AlGaAs NWs	48
3.2	Microscopes and detectors	49
3.3	Measurement series	50
3.3.1	EDS detector characterization	50
3.3.2	Quantitative EDS of III-V heterostructures	51
3.4	Data processing	52
4	Results	55
4.1	EDS detection system and setup	55
4.1.1	Preliminary sample inspection	55
4.1.2	EDS characterization	57
4.2	Heterostructure GaAs/GaAsSb NWs	62
4.2.1	Preliminary sample inspection	62
4.2.2	Quantitative EDS analysis	65
4.3	Heterostructure GaAs/AlGaAs NWs	70
5	Discussion	73
5.1	EDS detection system and setup	73
5.1.1	Preliminary sample inspection	73
5.1.2	EDS characterization	75
5.2	Heterostructure GaAs/GaAsSb NWs	82
5.2.1	Preliminary sample inspection	82

5.2.2	Quantitative EDS analysis	83
5.3	Heterostructure GaAs/AlGaAs NWs	90
6	Future work	92
6.1	Develop alternative detector characterization standard test	92
6.2	Investigating denoising effects for ICD for LV STEM	93
6.3	Deal with Al strays in SU9000	93
7	Conclusion	97
	Bibliography	98
A	Appendix	106
A.1	Jupyter Notebooks for detector characterization	106
A.2	Jupyter Notebook for initial inspection and editing of EDS map data	113
A.3	Jupyter notebook for Internal Composition Determination	116
B	Appendix	127
B.1	Concentration profiles from SU9000 denoised using PCA	127
B.2	k-factors for Cliff-Lorimer quantification in Aztec	131

1 | Introduction

Over the last few decades, III-V semiconductor compound materials such as GaAs and GaN have received increasing attention due to the ability to tune their optical and electric properties that can be controlled through alloying and geometry. For application in lasers or LEDs, the emission spectrum can consequently be tuned for specific wavelengths by controlling the composition ratios in the ternary compound [1, 2]. Alternatively, the gap can be tuned for optimized efficiency in the solar spectrum for application in solar cells [3]. With the continuous downscaling of electrical components and development within nanotechnology, the introduction of nanowires (NWs) in such devices is a growing field. This is partly due to their ability to accommodate strain, enabling defect-free growth on lattice-mismatched substrates improving device efficiency and reducing costs [4, 5]. Furthermore, creating low-strain combinations of semiconductors with different band gaps, or so-called heterostructures, can be easier within nanowires (NWs) than in thin film geometry. Heterostructured NWs also open for more design freedom as three-dimensional axial [6, 7] and radial [8, 9] heterostructures can be achieved.

To optimize and control the device behavior, all such applications require reliable quantitative composition characterization techniques with nm-scale spatial resolution. This can be achieved by energy dispersive X-ray spectroscopy (EDS) in electron microscopes, both scanning electron microscopes (SEM) and transmission electron microscopes (TEM). The incident electron beam creates X-rays due to inelastic interactions with the illuminated matter. EDS is the most widespread composition analysis technique integrated in most modern-day electron microscopes. It is commonly used due to its simplicity compared to alternative methods such as cathodeluminescence (CL) and electron energy loss spectroscopy (EELS).

In order to translate X-ray intensities at a specific energy characteristic of the illuminated element, to quantitative compositions, Cliff-Lorimer (C-L¹) is the most commonly used method for thin (< 100 nm) specimens in TEM. This method is based on the thin-foil criteria, which requires the specimen to be sufficiently thin for absorption and fluorescence effects to be ignored. Using this assumption, the composition ratio can be expressed to be proportional to the intensity ratio of the characteristic X-ray lines of the two elements with a proportionality constant that are sensitivity factors called k-factors [10]. Accurate² determination of k-factors is consequently crucial for accurate composition analysis. Calculated k-factors are generated within the detector

¹C-L abbreviation for Cliff-Lorimer not to be confused with CL (cathodeluminescence).

²Accurate in this context means how close it is to the real value.

software, limiting the transparency and accuracy of the compositional analysis. Higher accuracy can be achieved by determining k-factors experimentally with multi-element standards. Regardless, achieving higher precision with experimental determination of k-factors compared to calculated is a tedious and difficult affair [11]. Either way, standard methods for determination of k-factors will leave the quantitative calculations with a relative error of 5% [11].

To counter the disadvantages of Cliff-Lorimer, Watanabe suggested an alternative called the ζ -factor method, where the sensitivity factors have a more physical basis. The advantages of the ζ -method compared to Cliff-Lorimer is that it uses pure-element standards, as well as it determines the mass thickness simultaneously as the composition. However, this method also relies on accurate determination of sensitivity factors, in addition to the probe current. Other approaches have been developed over the last decade to resolve the sensitivity factor issues in the mentioned quantification methods [12–14], but all rely on standards with a known thickness or advanced simulation tools, making them difficult to apply by a microscope user. To summarize, using sensitivity factors makes quantification procedures easier, but the overall accuracy is reliant on the accuracy with which the factor can be determined.

In order to overcome these challenges, an alternative factorless thin film X-ray analysis procedure with minimal input parameters was outlined by J. Nilsen for internal determination of ternary III-V compound materials [15]. This is called Internal composition determination (ICD), as it makes use of an internal area with known concentration, i.e. the binary compound, as a reference area for analysis of the ternary compound. Additionally, the algorithm is using a benchmark element with a constant concentration. Consequently, the algorithm has a theoretically easy built-in absorption correction, without the need for external sensitivity or correction factors. The method is proven to improve the accuracy of quantitative EDS compared to Cliff-Lorimer for 200 kV TEM EDS and has additional advantages such as determination of thickness and sensitivity factors. Although in principle the approach is generic, it is unknown if it is generally applicable in other set-ups, such as low voltage ranges typical for SEMs.

In this work, the ICD method is for the first time used and evaluated at low acceleration voltages in a SEM. Similar samples as J. Nilsen used in developing the ICD method are used. Specifically, two different GaAs-based nanowires are studied, namely a GaAsSb axial heterostructure, and a radial heterostructured AlGaAs NW. The method is applied to EDS measurements from high tension (HT) TEM (200 kV) as a reference, and in a low voltage (LV) scanning transmission electron microscope (STEM) (5-10-15-30 kV) to systematically investigate how the ICD method performs. It is of specific interest to develop the factorless ICD method to LV electron microscopes and investigate whether the algorithm achieves higher accuracy quantitative analysis. Its reliability is compared to the standard Cliff-Lorimer method with calculated k-factors.

The EDS detection system in the SU9000 STEM has previously not been used for ICD analysis, and has features that can improve the analysis as a windowless detector. Therefore, a second focus

point of this work was to characterize the EDS detectors used that allow comparison between set-ups. The characterization is based on a standard test using a NiO thin film on Mo TEM grid [16]. Here, fundamental detector features such as shadowing and energy resolution, as well as stray radiation within the column are identified. Subsequently, the EDS setup is optimized and EDS data calibrated for the subsequent compositional analysis. For this work, a general detector characterization Jupyter Notebook was developed, that calculates all relevant detector and microscope features based on an EDS spectrum from the NiO test specimen.

This thesis is built up as follows. First, the required theory on III-V semiconductor NWs, EDS, electron microscopy and crystallography is given with a focus on quantitative EDS analysis. Then, an overview of the experimental setup and measurement series is given. Subsequently, the results from both EDS characterization and the quantitative analysis using the ICD method are provided, followed by a discussion of the observations. Lastly, suggestions for future work and the conclusions are given. In the appendix, the used and developed python-based code is given such that the results of this work can be verified. This code can also be applied to other material systems and setups. Thereby the outcome of this work goes beyond ICD, the studied heterostructure NWs and the detectors used, as composition variations at the nm scale are crucial in understanding and optimizing technical advanced materials.

2 | Theory

In this chapter, a theoretical background for the present work is presented. First, a general description of the materials subjected to the compositional analysis is given. Subsequently, a detailed review of compositional analysis using EDS is provided. Lastly, an overview of crystallography and diffraction, followed by general imaging in electron microscopes is given. Large parts of this chapter is based on theory previously written by the author [17].

2.1 Semiconductor materials

Here, a general introduction to III-V semiconductor materials is presented, followed by an in depth description of the specific materials central to this work. The theory is mainly based on [18], unless otherwise stated.

2.1.1 III-V semiconductors

Semiconductors are materials defined by an electrical conductivity between metals and insulators. This is due to the energy band gap between the valence and conduction band, which is smaller than that of an insulator. Semiconductors with no impurities or lattice defects are called intrinsic semiconductors. In such materials, the valence band is filled and there are no allowed states in the conduction band at 0 K. At room temperatures, a semiconductor with energy gap of for example $E_g = 1$ eV will have a significant number of electrons that are thermally excited across the energy gap into the conduction band. Carriers can also be generated by purposely introducing impurities into the crystals. Such altering of the crystal to have a predominance of either electrons or holes is called doping, and the semiconductor material is called extrinsic.

Elemental semiconductors composed of single species atoms such as silicon and germanium can be found in the IV column of the periodic table. Compound semiconductors on the other hand are materials consisting of atoms from different columns. III-V semiconductors are such alloy materials consisting is of atoms from column III and V. Gallium arsenide (GaAs) is an examples of a III-V semiconductor material that is often used in optoelectric devices. This is in large part due to its direct band gap. A direct band gap is defined by having the same electron momentum vector \mathbf{k} for the valence band maximum and the conduction band minimum. For an indirect semiconductor,

the conduction band minimum have a different \mathbf{k} -value than the valence band maximum, requiring a change in the electrons momentum during a smallest-energy transition from the conduction to the valence band. Consequently, part of the energy is generally given up as heat to the lattice, decreasing the device efficiency.

Particularly interesting for III-V semiconductor materials is that the electrical and optical properties, specifically its band gap, can be tuned by altering the material composition. By substituting the atoms in either the III or V sub-lattice with another atom from the same column, the composition is varied to create ternary compounds with modified band gaps. The band gap energy is directly dependent on the concentration of the substituting material (see Fig. 2.1), and enables for example tuning of the wavelength of the light emitted from devices such as LEDs or lasers from the infrared to the visible part of the spectrum.

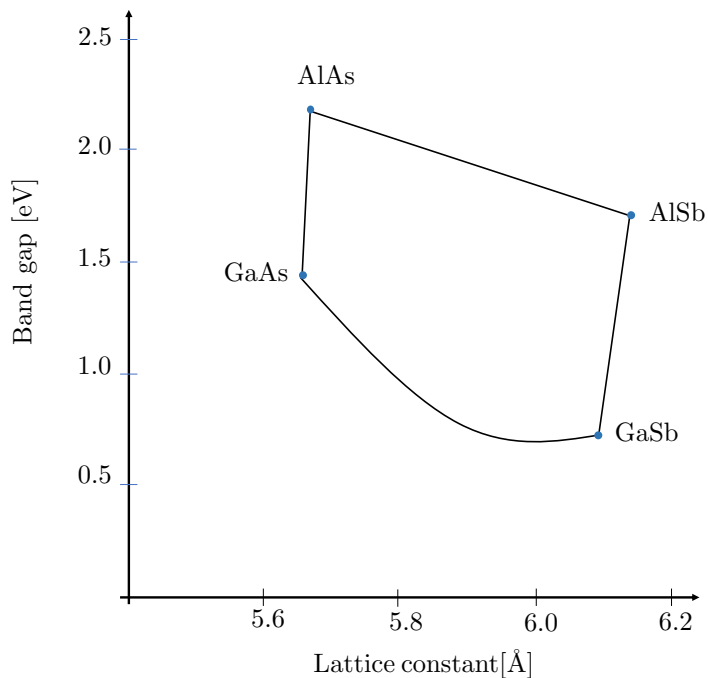


Figure 2.1: The band gap energy, E_g , versus lattice constant for ternary III-V compound semiconductor materials. (Figure adapted from [18])

Two of the most important examples of such binary III-V semiconductor materials are the AlAs-GaAs and the GaSb-GaAs systems. In the first, Al replace the Ga atoms in the III sub-lattice and the column V sub-lattice containing As atoms remains unchanged. In the latter, Sb atoms replace the As atoms in the V sub-lattice, and the III sub-lattice containing Ga atoms remains unchanged. Subscripts are commonly used to denote the fraction of the subsisting atom, x , relative to the fraction of the substituted atoms, $1 - x$, by writing $\text{Al}_x\text{Ga}_{1-x}\text{As}$ or $\text{GaAs}_{1-x}\text{Sb}_x$. GaAs has a direct band gap with energy $E_g = 1.43$ eV at room temperate, and alloying with either Al

or Sb will alter the band gap energy according to Fig. 2.1¹. Furthermore, Figure 2.1 shows the band gap energy as a function of the lattice parameter, which is another advantage to the AlGaAs compounds, namely the negligible change in lattice parameter for varying x . Hence, changing the composition do not introduce strain that could lead to defects, reducing efficiency.

2.1.2 Heterostructured GaAs-based NWs

Heterostructured materials are made by layering III-V semiconductor compounds with alternating material composition. At the interface between two adjacent semiconductors with different band gaps, a heterojunction is established and can be virtually free of defects due to the lattice match. At the heterojunction, the Fermi levels line up in equilibrium, causing spatial variations in the conduction and valence band. An example is provided in Figure 2.2, which is a simple heterostructure consisting of a thin layer of GaAs between regions of AlGaAs with larger band gap. In this particular case, the electrons and holes will be confined in the very thin GaAs layer, making them subject to the particle in a potential well problem described with basic quantum mechanics [19]. The complexity of heterostructure systems may increase if multilayered structures are made.

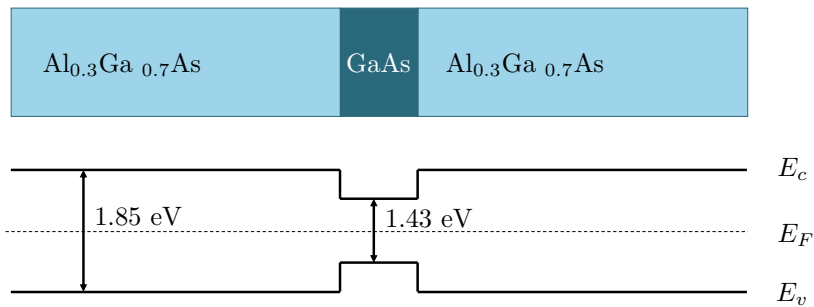


Figure 2.2: Schematic of the spatial variations of the conduction and valence band in a GaAs-AlGaAs heterostructure, with a thin film of GaAs is sandwiched between two larger band gap AlGaAs regions. Within the GaAs layer, the electrons behave as predicted by the *particle in a potential well* problem with quantized energy levels. (adapted from [18])

Current technology is based on two-dimensional heterostructures, but more design freedom for optimized device behaviour is achieved in three-dimensional heterostructures, made possible by the continuous development within nanomaterial fabrication. Nanowires are one-dimensional materials that are fundamentally different from two- and three-dimensional materials due to their high aspect ratio and surface to volume ratio. In general, nanowires has the potential to optimize and improve the performance in an array of applications, such as optical devices [2] and solar cells [3, 20]. First of all, conventional scaling methods to reach sub 100 nm feature sizes in such devices faces

¹Here assuming Zinc Blende crystal structure.

an increasing number of fundamental technological challenges. Additionally, their efficiency is noticeably impaired by defect formation within bulk materials which is minimized in these one-dimensional structures.

Axial GaAs/GaAsSb NWs

The first sample material studied in this project are GaAs/GaAsSb NWs with axially varying Sb concentration (see Fig. 2.3a) previously fabricated for application in quantum well (QW) lasers [1, 21]. The wires are grown to have a series of layered GaAsSb insets with smaller band gap in between regions of GaAsSb with larger band gaps creating quantum wells as previously described. These layered quantum well regions are called superlattices (SLs) and results in valence and conduction band edges as seen in Fig. 2.3b. The wires have six SL named SL-1, SL-2 etc., separated by GaAs spacers. In total, there are six SLs in the wire, where each SL contains ten GaAsSb layers, named W1, W2 etc., with a GaAs potential barriers B1, B2 etc. in between.

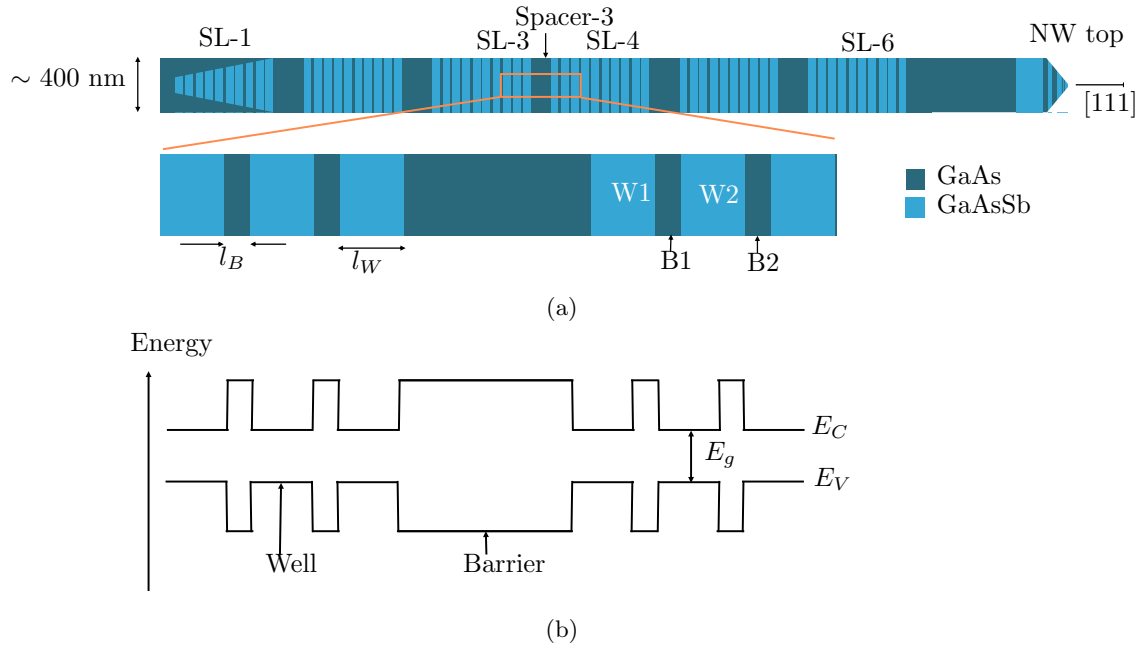


Figure 2.3: (a) Schematic drawing of the GaAs/GaAsSb NWs with axial variations of Sb in the numbered superlattices (SL) separated by spacers. The length of the wells, l_W , and the barriers, l_B , is also indicated in the magnified area, along with the (b) electron energy band diagram showing the quantum wells and barriers.

Lasers, or Light Amplification by Stimulated emission of Radiation, are electrical and optical devices that emits highly directional, monochromatic and coherent light. Stimulated emission occurs when a photon is incident on an excited atomic electron, which triggers the relaxation of the excited electron and consequently the emission of a new photon with energy equal to the band gap [22]. In materials with direct band gap, such as GaAs, the "daughter" photon will be coherent

to the incident photon. In semiconductor lasers, the structure need to have an active region, population inversion and an optical cavity. The active region is where electron-hole recombination takes place. Population inversion means there are more electrons occupying higher energy states than lower such that the stimulated emission exceeds the absorption during interaction with the photons. Optical cavity reflects the photon back into the active region such that the signal is amplified [23]. In NW lasers, it is the end facets that work as reflective mirrors and the wire itself acts as a gain medium forming a Fabry-Pérot (FP) cavity. The wires studied here are so called quantum well nanowires lasers. In these structures, the active region is the quantum wells, and the wavelength of the emitted light is subsequently tuned by altering the size of the QW and by modifying the energy band gap by tuning the composition.

Radial GaAs/AlGaAs NWs

Where in the sample above, the energy band gap is controlled, the second sample studied in this work is fabricated with a potential barrier on the outside if the NW. In this case, the wires have a core-shell structure [24], where the core of the NW consists of GaAs and is surrounded by a shell of AlGaAs as seen in Figure 2.4. As the outer shell has a larger band gap than the core, this creates a flow of carriers to the core band gap and enhance optical properties. Furthermore, GaAs has a high degree of surface states, causing non-radiative combinations at the surface of the material. A high energy barrier created by the shell subsequently passivates the interface states and increases the optoelectric properties of the wires [25]. Heterostructured GaAs/AlGaAs NWs have proven to introduce many advantages due to the materials lattice characteristics. Since AlAs and GaAs have similar lattice parameters, it is possible to grow axial and radial hetero structures without build-up of strain.

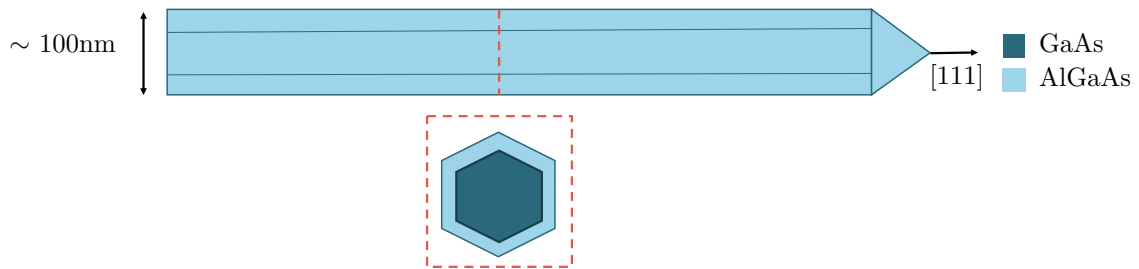
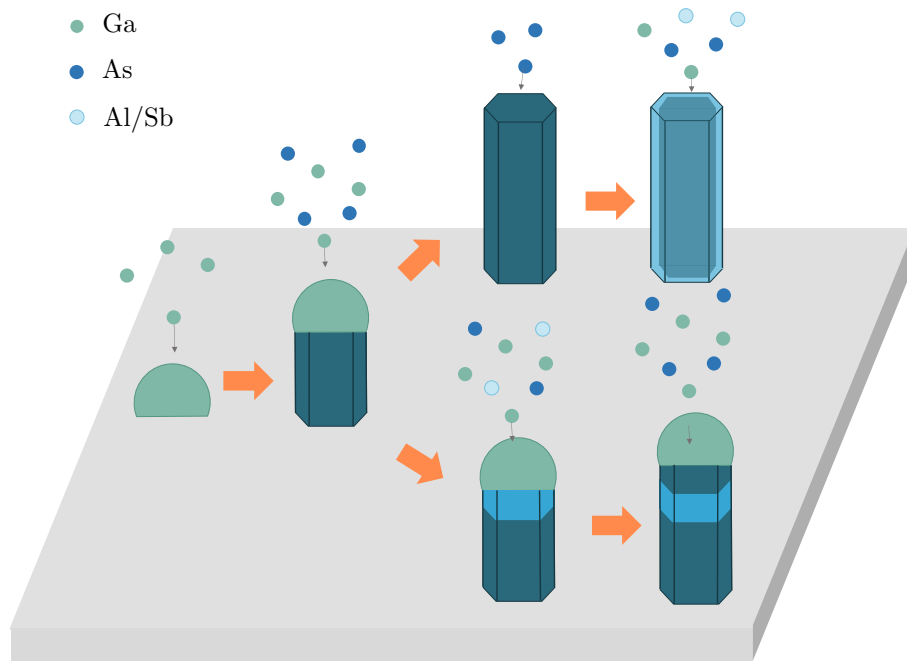


Figure 2.4: Schematic drawing of the hexagonally shaped GaAs/AlGaAs core-shell nanowires from a side view with indicated growth direction [111], and a cross-section axial view.

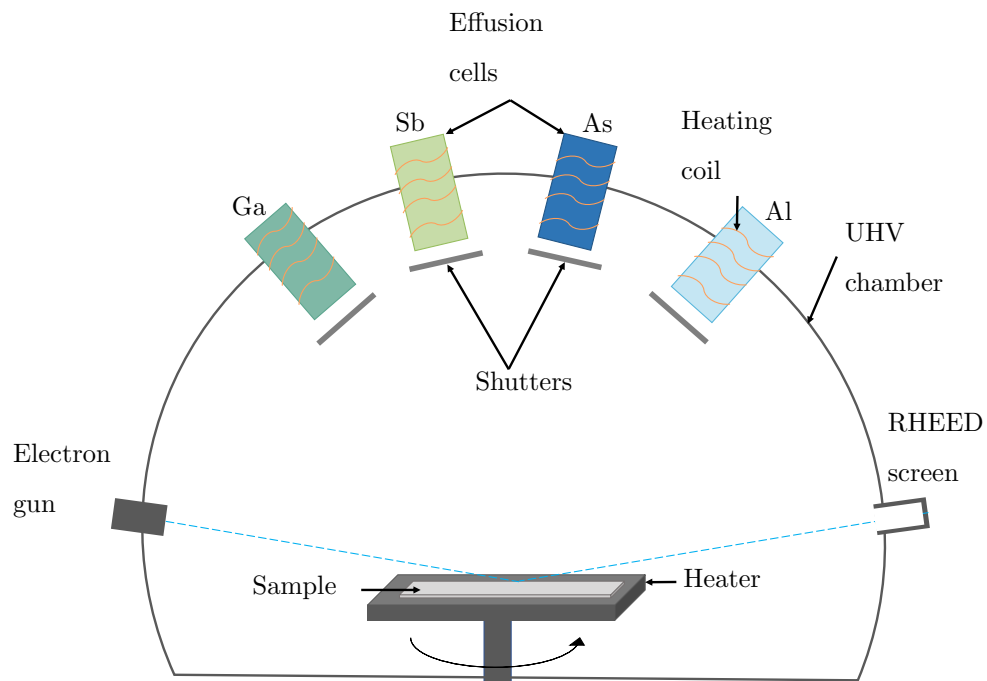
Nanowire growth

An array of techniques have been developed over the last decades to fabricate high quality nanowires. One of the most common methods is the vapour-liquid-solid (VLS) mechanism which is based on a three phase system. VLS includes introducing an impurity or a metal catalyst particle in liquid form at the growth temperature. The purpose of the catalyst particle is to direct the growth direction into a specific orientation and within a confined area. The NW precursor elements are introduced through a gas flow in the growth chamber and react with each other to create the semiconductor compound. Subsequently, the precursor elements are trapped within the catalyst, where they will precipitate at the growth surface resulting in a one-directional growth [26]. Au is a common catalyst material, however, possible unwanted integration of Au into the wire, a self-catalyst approach is used for the wires in this work. This means that one of the growth elements is used as the catalyst element, in this case Ga.

The introduction of the precursors elements are in this case done by molecular beam epitaxy (MBE). In MBE, the solid precursor sources are stored in effusion cells, and the influx is controlled by heating of these cells. MBE is a technique which provides high purity and composition control due to the ultra high vacuum (UHV) preventing the precursor atoms to interact before reaching the catalyst particle. In order to create axial composition variations, the influx of the precursor gas are varied. If the growth conditions are changed or the catalyst particle is consumed, further growth primarily happens via incorporation of the vapor phase directly on the surface, i.e. vapor-solid (VS) mechanisms. This mechanism is used to grow the aforementioned core-shell structures.



(a)



(b)

Figure 2.5: (a) Schematic illustration of the mechanism in VLS where (top) the Ga catalyst particle is consumed to initiate shell growth and (bottom) the influx of precursor concentrations are varied to grow axial insets with varying composition. (b) Schematic drawing of a typical UHV MBE chamber with effusion cells with shutters and heating coils to control the introduction of precursor gass.

2.2 Energy dispersive X-ray spectroscopy

Energy dispersive X-ray spectroscopy (EDS) in SEM and TEM is the most commonly used compositional analysis technique with a degree of spatial resolution. Here, the material is irradiated with energetic (1-200 kV) electrons in order to determine the elemental composition of the specimen. In the following sections, an in depth description of the physical phenomena governing EDS, as well as experimental instrumentation and data processing with focus on quantitative EDS analysis is provided. The majority of the theory is based on Chapter 32-35 in [11], which is a reference text for TEM EDS. In this work, HT SEM range (1-30 kV) is also used, but seeing as the specimen geometry is a thin film, the standard theory for HT TEM is applied.

The basic principle behind any electron microscope is to have a high energy (1-400 keV) electron beam incident on the sample material. The electrons will interact with the sample by a series of scattering events, generating an assortment of signals (see Fig. 2.6) which provides information on the sample topography, crystal structure, composition etc. The signals can be sorted in elastic and inelastic scattering. Elastic scattering refers to scattering events with no loss of energy for the initial electron, while inelastic scattering refers to a scattering event where there is loss of energy. Inelastic scattering signals such as secondary electrons (SE), elastically backscattered electrons (BSE) and transmitted electrons are also important for imaging and diffraction, and will be discussed in Sec. 2.4. In this section, inelastic scattering that creates X-rays are central. In general, there are two types of X-rays emitted, namely characteristic X-rays and Bremsstrahlung X-rays. In the following sections, the origin and nature of these X-ray signals are described in detail.

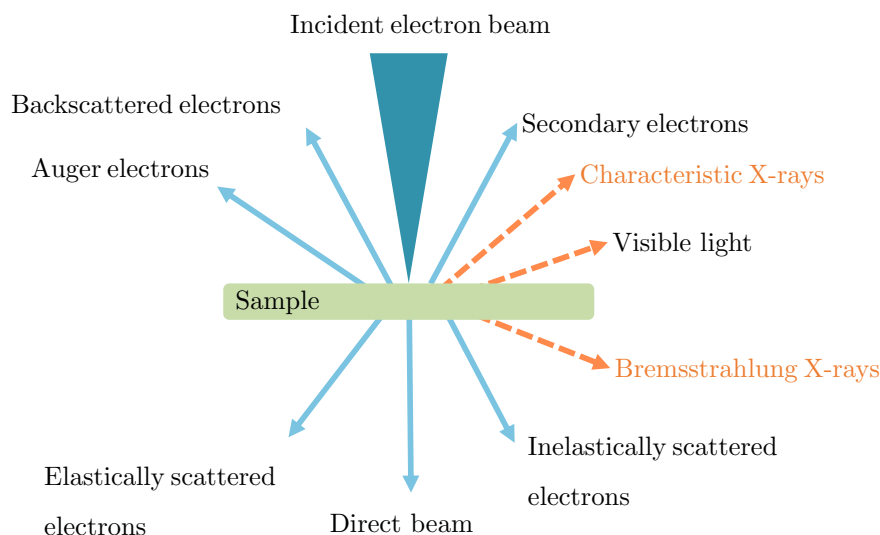


Figure 2.6: Schematic drawing of the most commonly used signals created when electrons from an incident beam interacts with the sample. The X-ray signals most relevant to this section is in orange. Adapted from [11].

2.2.1 X-ray generation

Bremsstrahlung radiation

Bremsstrahlung radiation originates from the incident electrons interacting with the Coulomb field of the nucleus, which results in a change in momentum for the primary electrons. When a charge is (de)accelerated, the change in momentum generates EM-radiation which can be any value up to the beam energy, depending on the strength of the interaction. The probability of Bremsstrahlung creation is usually described by Kramer's cross section

$$N(E) = \frac{KZ(E_0 - E)}{E} \quad (2.1)$$

which gives the number of photons, $N(E)$, with a specific energy, E , created by electrons with energy E_0 , where K is Kramers constant, and Z is the atomic number of the ionized atom. The X-ray intensity increases rapidly with decreasing X-ray energy. However, X-rays with energies $< \sim 2$ keV are absorbed in the sample and are not detected (see Fig. 2.8). In quantification, the continuous function $N(E)$ forms a background signal, which needs to be removed in post-processing (see Sec. 3.4).

Characteristic X-rays

Characteristic X-rays are generated through inelastic scattering events between the incident electrons and inner shell electrons in the sample. Given that the incident electrons have sufficiently high energy, i.e. higher than the critical ionization energy, the energy transfer will provide the inner shell electrons with enough energy to escape the attractive forces of the core. Consequently, the atom is left in an excited state with energy above its ground state, which promotes relaxation of an outer shell electron to lower the atoms total energy. Energy conservation dictates that the inner shell transition energy difference is conserved through either the release of another electron, called Auger electrons, or the creation of a photon (see Fig. 2.7). Since all energy shell values are specific for each element, such photons are referred to as characteristic X-rays and can be viewed as a "chemical fingerprint". Detecting the energy of the emitted X-rays is accordingly used to determine the elemental composition of the sample. When recording a spectrum of all the generated X-rays within a sample, the characteristic X-rays will be merged with the continuum X-rays as seen in Fig. 2.8.

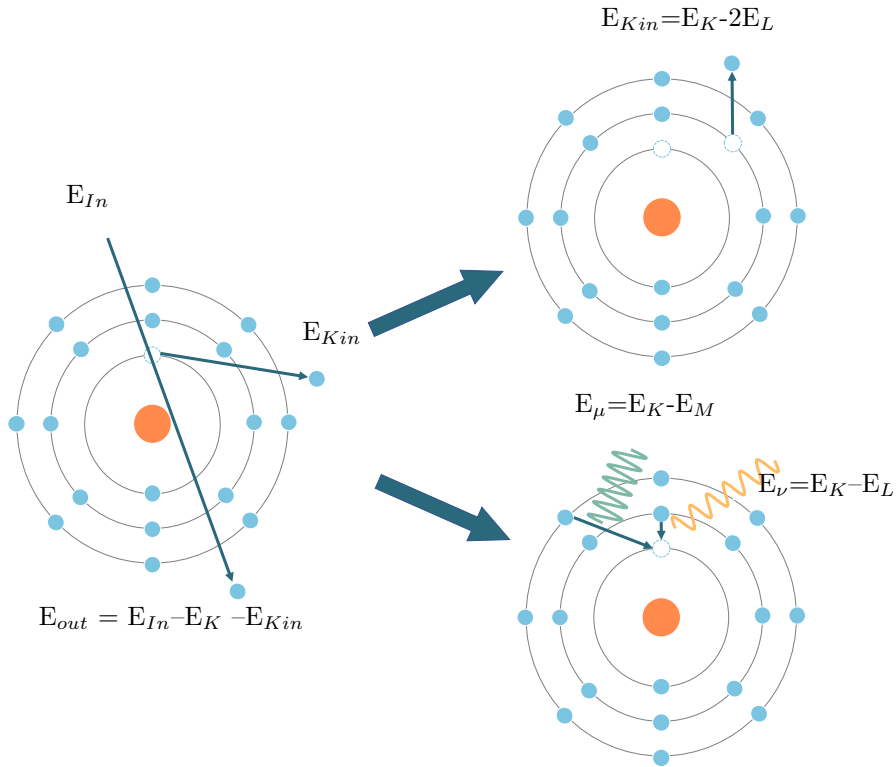


Figure 2.7: Schematic illustration of the process to create a characteristic X-ray (bottom) and an Auger electron (top). The incoming electron with energy E_{In} scatters inelastically with a K-shell electron escaping with a kinetic energy E_{Kin} . Depending on which shell the relaxed electron originates from, the generated X-ray will have energy E_μ or E_{nu} .

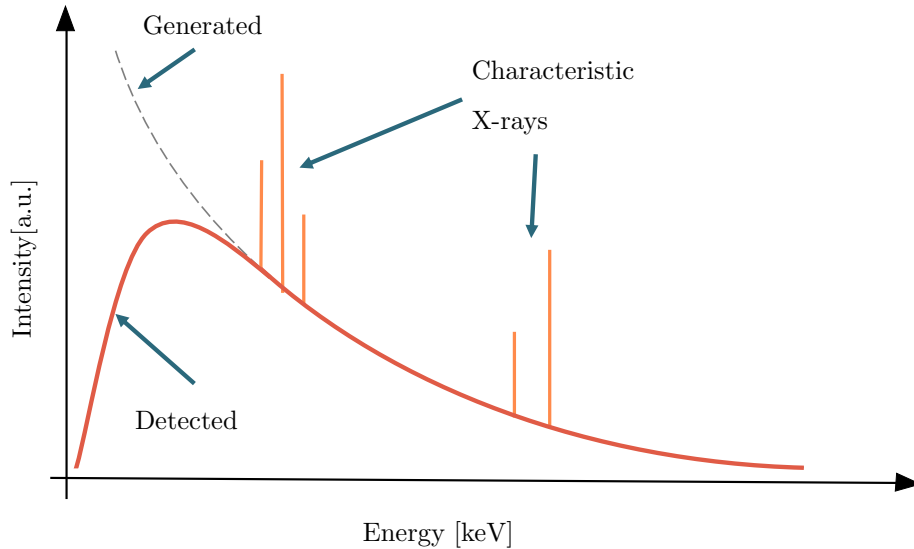


Figure 2.8: Illustration of a generated X-ray spectrum within a sample. The grey dotted lines indicates the generated Bremsstrahlung radiation, and the red indicates the X-rays that are actually detected. Merged with the background radiation is the characteristic X-ray peaks seen in orange.

To identify the different characteristic X-rays, specific terminology based on the simple Bohr model is used. In this model, the electron shells in atoms are labeled K, L, M, etc., where K refers to the inner most shell, while L and M are the subsequent shells. If a K shell electron is excited, and an L shell electron is relaxed, the emitted X-ray is labeled $K\alpha$. Here, the K refers to the shell where the first excited electron originates from, and α refers to the shell where the relaxed electron originates from. If instead the relaxed electron originates from the M shell, there will be a $K\beta$ X-ray emitted. All energy shells except the K-shells also have sub-shells, which is denoted with an additional number subscript (see Fig. 2.9). Each specific characteristic X-ray is referred to as *lines*. Groups of lines, e.g. X-rays created by relaxation to the same energy shell, are referred to as *families*. With increasing atomic number, there is an increase in possible electron transitions with varying probability of occurring. Therefore, each X-ray line is given a weight, which is the intensity of the line relative to the most intense in the family. Table 2.1 contains the energy and weight of some X-ray lines for the elements relevant for this work.

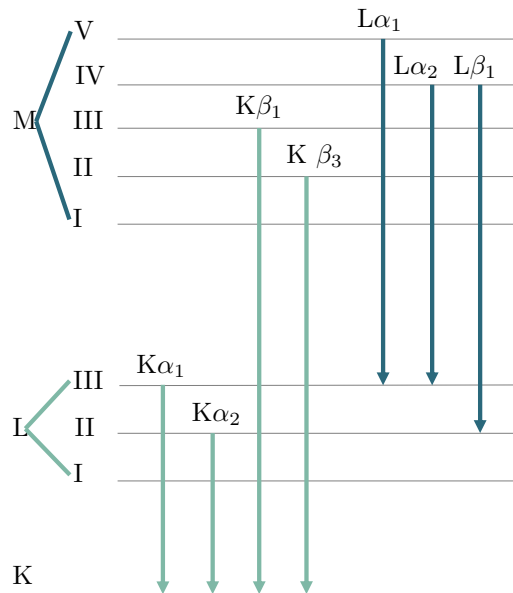


Figure 2.9: Energy shells and subshells with some of the possible X-ray lines and their associated name.

Table 2.1: Values for X-ray line energy and weight for K, L and M lines for the elements relevant to this work. The lines are arranged with increasing line energy, and the values are gathered from the elemental database in the HyperSpy library [27]

Energy	Element	Line	Weight
0.2774	C	K α	1.0
0.5249	O	K α	1.0
0.6768	F	K α	1.0
0.7045	Fe	L α	1.0
0.7429	Ni	L l	0.14
0.8511	Ni	L α	1.0
0.9295	Cu	L α	1.0
1.098	Ga	L α	1.0
1.2819	As	L α	1.0
1.4865	Al	K α	1.0
1.7397	Si	K α	1.0
2.1229	Au	M α	1.0
2.2047	Au	M β	0.59
2.2932	Mo	L α	1.0
2.3948	Mo	L β_1	0.33
3.6047	Sb	L α	1.0
6.4039	Fe	K α	1.0
7.058	Fe	K β	0.13
7.4781	Ni	K α	1.0
8.0478	Cu	K α	1.0
8.2647	Ni	K α	0.13
8.9053	Cu	K β	0.13
9.2517	Ga	K α	1.0
9.713	Au	L α	1.0
10.5436	As	K α	1.0
11.4425	Au	L β_1	0.4
17.4793	Mo	K α	1.0
19.6072	Mo	K β	0.15

Critical ionization energy

In order to have an excitation of an inner shell electron, the primary electron has to transfer a critical amount of energy required for ionization, referred to as critical ionization energy, E_c . With increasing atomic number, Z , the attractive forces from the core increases, and E_c will increase. Consequently, higher energy incident beam electrons are required for a satisfactory X-ray generation. Generally, the critical ionization energy will be less than 20 keV.

Ionization cross section and overvoltage

Assuming the incident electrons have sufficient energy, it is not given that an ionization event will occur. Ionization cross section, σ , describes the probability of ionization. The original expression for the total scattering cross section was given by Bethe [28] as

$$\sigma_T = \left(\frac{\pi e^4 b_s n_s}{E_0 E_C} \right) \log \left(\frac{c_s E_0}{E_C} \right) \quad (2.2)$$

Here, e is the electron charge, n_s is the number of electrons in the ionized shell and b_s and c_s are constants for the specific shell. For high energy electron beams $E_0 > 100$ kV, i.e. beams in TEM, the cross section is relatively large, and insensitive to the changes in acceleration voltage. However, when the energy of the electron beam becomes comparable to the critical ionization energy, as is done in low-voltage SEMs, the cross section will depend on the overvoltage, U . The overvoltage is the ratio of the beam energy E_0 to the critical ionization energy, E_C , and is related to the cross section as depicted in Fig. 2.10. As can be seen, the probability of ionization drastically increases from $U = 0$, to a maximum at $U \sim 5$. Above this maximum value, the cross section decreases, but stays relatively fixed for higher voltages typical for TEMs.

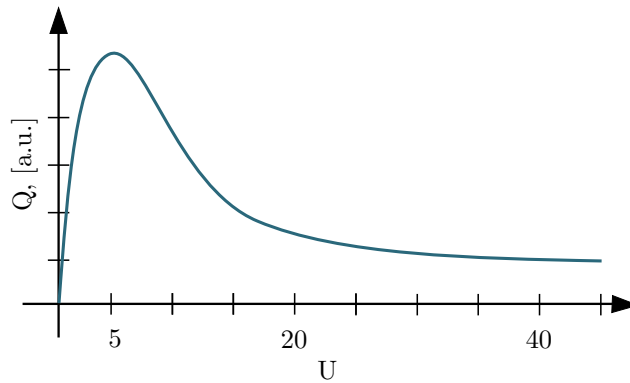


Figure 2.10: Ionization cross section, Q , as a function of the overvoltage, U . Q has maximum value when overvoltage is $U \sim 5$. (adapted from [11])

Fluorescence yield

As mentioned, the ionization of an atom can be followed by either the emission of an X-ray, or an Auger electron. The fluorescence yield, ω , is a measure of the probability of creating an X-ray instead of such Auger electrons. ω is the ratio of X-ray emission to the number of inner shell ionization events. The fluorescence yield is strongly dependent on the atomic number, Z , and can be approximated to the following expression:

$$\omega = \frac{Z^4}{a + Z^4} \quad (2.3)$$

where $a \sim 10^6$ for the K shell. Using this approximation, the fluorescence yield of for example C with atomic number $Z = 6$ is $\omega_{Al} \sim 0.001$, while for As with atomic number $Z = 33$, $\omega_{As} \sim 0.5$. In other words, 1000 C atoms have to be ionized in order to create a $C_{K\alpha}$ X-ray, while only 2 As atoms has to be ionized before an $As_{K\alpha}$ X-ray is generated. Elements below Be with atomic number $Z = 4$ are not detectable.

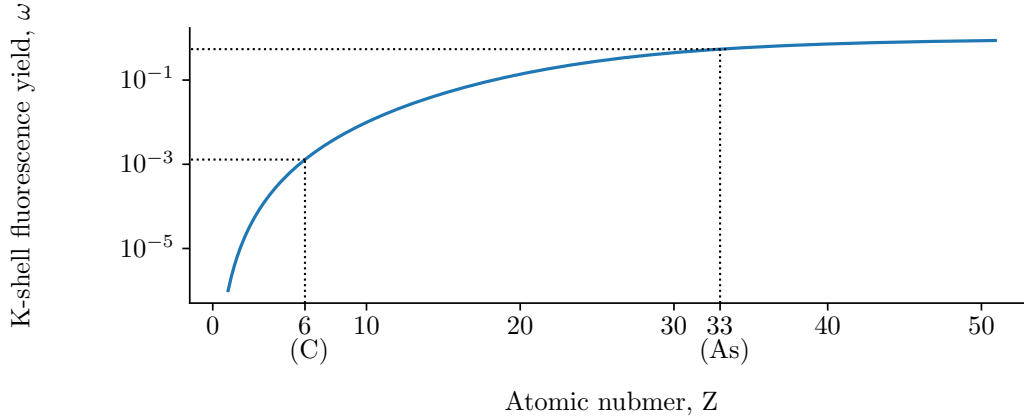


Figure 2.11: Plot showing the heavy Z -dependence of the fluorescence yield for K-shell electrons. Note the logarithmic y-scale, and the rapid decrease at low atomic numbers.

X-ray intensity

The generation of characteristic X-rays is a complicated series of phenomena, especially in a bulk sample. In a thin specimen on the other hand, the X-ray generation can be simplified by making three key assumptions. First, the energy loss of the incident electrons can be neglected. Second, in high HT TEM, most of the scattering events are forward scattering, and electron backscattering loss can also be ignored. Lastly, the depth distribution of X-ray production is unity. Thereby, the X-ray intensity, I_C , can be assumed to be proportional to the mass-thickness, ρt , as follows

$$I_C = \frac{sQ\omega a C N_v D_e}{A} \rho t \quad (2.4)$$

Here, s is a scaling factor to adjust the absolute magnitude for the ionization cross-section, Q . ω is the fluorescence yield, a is the line weight, C is the weight fraction, N_v is Avogadro's constant, A is the atomic weight and D_e is the total electron dose. The last being defined by

$$D_e = N_e I_p \tau \quad (2.5)$$

where N_e is the number of electrons in a unit electric charge, I_p is the probe current and τ is the acquisition time. Most importantly, the intensity of an X-ray is directly dependent on the weight fraction, which is the foundation for quantitative EDS analysis. However, Eqn. 2.4 reveals that the intensity of the characteristic X-ray is also dependent on experimental parameters such as the probe current, measurement time and the amount of material, in addition to material specific physical constants such as ω and σ , who's values are difficult to accurately determine.

After an X-ray has been created, it has to travel through the sample before it reaches the detector. Along its path within the specimen, there is a probability that the X-ray will be absorbed. The attenuation of the intensity, I_C , of an X-ray A is dependent on the specimen composition and thickness. This can be described by Beer-Lamberts law

$$I_C = I_0 \exp(-[\mu/\rho]_{sp}^A \rho t) \quad (2.6)$$

where I_0 is the initial intensity, $[\mu/\rho]_{sp}^A$ is the mass-absorption coefficient and ρt is the mass-thickness. It is clear from Eqn. 2.6 that the amount of absorption increase with heavier elements, and a thicker specimen. In general, the mass-absorption coefficient is higher for low energy X-ray lines, making low energy photons more likely to be absorbed, and hence not detected. A Table containing some of the relevant mass-absorption coefficients for this work is seen in Tab.2.2.

Table 2.2: Mass-absorption coefficients, $[\mu/\rho]_{sp}^A$, of Ga, As, Sb and Pt for relevant X-ray lines $\text{Ga}_{K\alpha}$, $\text{As}_{K\alpha}$ and $\text{Sb}_{L\alpha}$. The values are extracted from HyperSpy library [27] which is based on previous listings by Chantler [29].

X-ray line	$\frac{\mu}{\rho}_{Ga}$	$\frac{\mu}{\rho}_{As}$	$\frac{\mu}{\rho}_{Sb}$	$\frac{\mu}{\rho}_{Pt}$
$\text{Ga}_{K\alpha}$	39	47	174	129
$\text{As}_{K\alpha}$	215	32	121	91
$\text{Sb}_{L\alpha}$	520	617	379	1364

2.2.2 EDS detection and system

A TEM or SEM is often referred to as an analytical electron microscope (AEM) when fitted with an EDS detector to record the emitted X-rays. The traditional EDS detector is a Si(Li) detector. These detectors are a reverse-biased p-i-n diode operated with liquid nitrogen cooling. When an incoming X-ray hits a semiconductor detector, it deposits energy, creating a number of electron-hole pairs directly proportional to the energy of the photon. The electron-hole pairs are separated by applying an internal reverse bias across the very narrow p-i-n junction, creating a charge pulse. The pulse is converted to a voltage, which is amplified through a field effect transistor and identified. A digitized signal is stored in the channel assigned to that energy in the computer display. Today, another design of EDS detectors are more common, namely the Si-drift detectors (SDD). The advantage to these detectors is that they can be operated with Peltier cooling instead of liquid nitrogen, and they have more design freedom to for example increase collection angle. The collection angle Ω , as seen in Fig. 2.12, will be dependent on both the detector design as well as the positioning of the detector relative to the sample in the specimen chamber. The detector is placed at a take off-angle, α , and the specimen can be tilted relative to the detector with a tilt angle θ , which is positive when the specimen is tilted towards the detector.

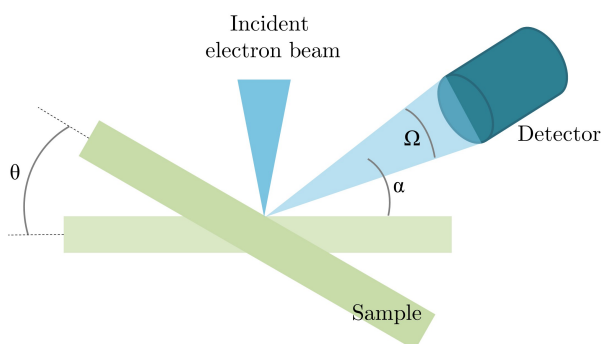


Figure 2.12: Schematic drawing of the EDS system setup where the detector is placed at a take-off angle α and has a collection angle Ω . The specimen is tilted towards the detector with a positive tilt angle θ .

The EDS system consists of mainly three parts, namely the detector, the processing electronics and a computer that controls the system (see Fig. 2.13a). Immediately after detecting a photon, the computer shuts the detector for receiving another photon, so that the detected photon can be analysed. The processing units then assign the X-ray an energy channel in the spectrum. The spectrum is displayed on the computer, along with intensity values, count rates, conditions under acquisition and other relevant parameters and metadata. After the X-ray has been processed, the computer turns the detector on again to detect the next incoming photon (see Fig. 2.13b). The period of time where the detector is effectively switched off is referred to as the dead time, and is generally less than a μs .

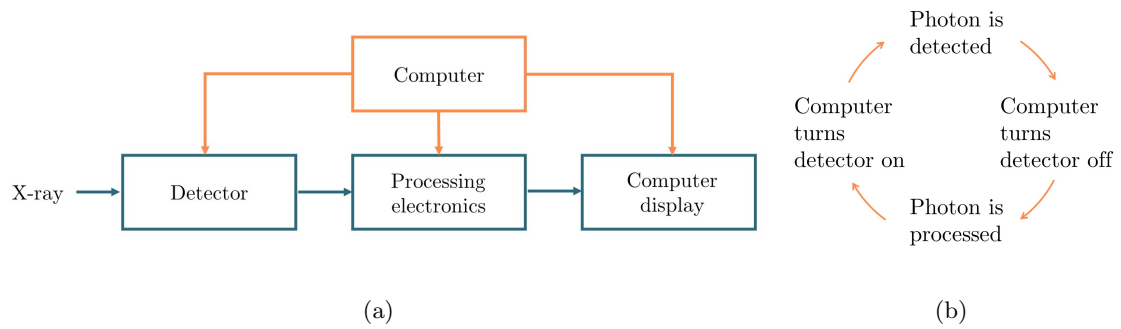


Figure 2.13: (a) Schematic of a typical EDS system where the computer controls the detector and the processing electronics, in addition to the computer display where the spectra and relevant metadata and acquisition details are shown. (adapted from [11]) (b) A flow chart of the process where detector is turned on and off while photons are processed.

In order to protect the detector from possible contamination in the AEM column, they are usually isolated in a pre-pumped tube with a sealed window which allows most X-rays through. The three types of window protection that is used is a beryllium window, a ultra-thin window, or windowless. A challenge with having a window in front of the detector, is that low-energy X-rays are absorbed in the window, preventing detection of for example B, C, N and O. For composition analysis of light elements, UTW have to be used.

Most electron microscopes are able to be operated in scanning mode, where a converged beam scans over a selected area. An EDS spectrum is then recorded for each probe position on the sample, and assigned to a pixel in a computer generated elemental map. For each pixel in the navigation space, the intensity of each X-ray line of interest can be extracted and shown as a color map on top of an image of the sample as seen in Fig. 2.14.

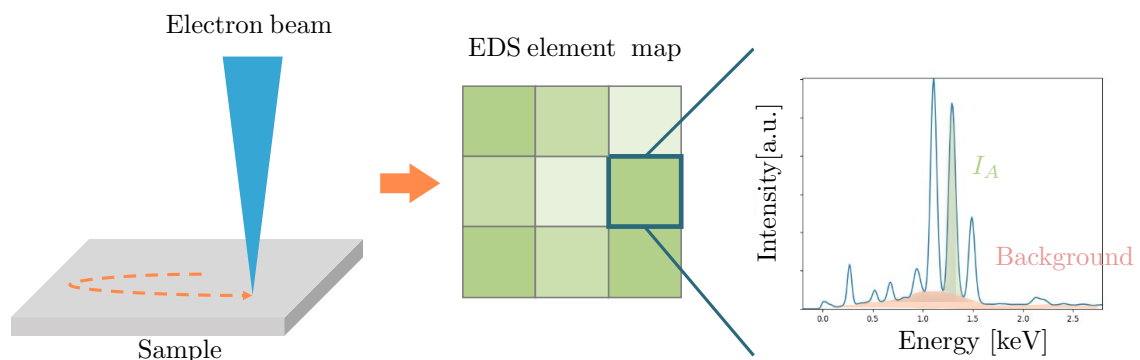


Figure 2.14: Illustration of element mapping of a sample using EDS in scanning mode in an electron microscope. A convergent beam scans the sample and an element map is generated where each pixel is given a color based on the intensity, I_A , of the characteristic peak for element A in the underlying EDS spectrum.

Stray radiation and artifacts

In addition to the characteristic peaks and background radiation generated within the sample, an EDS spectrum will also have artifact peaks from the detector system and unwanted stray X-ray signal from the AEM. This can cause incorrect quantitative and qualitative elemental determination of the sample composition. The artifacts introduced by the EDS system can be categorized into signal-detection artifacts (escape and internal fluorescence peaks) and signal processing artifacts (sum peaks).

Escape peaks are generated when the incoming photon with energy E_0 fluoresces a $\text{Si}_{K\alpha}$ X-ray (energy 1.74 keV) that escapes from the intrinsic region of the detector. Consequently, the detector will record an X-ray 1.74 keV below the true value of the characteristic peak. In general, escape peaks will be $< 2\%$ of the most intense peak in the spectrum in well designed detectors, and will only be visible for major characteristic peaks.

Internal fluorescence peak is a characteristic peak that originates from within the Si detector. An incoming photon can fluoresce $\text{Si}_{K\alpha}$ X-rays within the dead layer of the detector that enters the intrinsic region and is recorded as the detector is not capable of distinguishing its origin. The $\text{Si}_{K\alpha}$ internal fluorescence peak will always be present in a spectrum, especially if the live time is long enough.

Sum peaks are the last artifact, and arise from the electronics' lack of ability to discriminate between individual pulses at high count rates. If two photons enter the detector at the same time, the analyser will register an energy corresponding to the sum of the two photons. This is called pulse pile-up, and is best avoided by having a reasonably low input count rate ($< 10000\text{cps}$) such that the dead time is $< 60\%$.

In addition to the artifacts originating from the EDS system, the real spectrum will include X-rays that does not originate from the electron probe in the chosen analysis region. This can be divided into pre- and post-specimen effects. Pre-specimen effects comes from the TEM illumination system which produces high-energy bremsstrahlung X-rays and electrons that scatter outside the main beam. These will hit the specimen that are in fact from another part of the sample and produce spurious X-rays. Post-specimen scattering is caused by scattering of high-energy electrons and X-rays within the specimen, generating X-rays within the limited confines of the AEM stage. In summary, unwanted X-rays signals may be generated by electrons that are either electrons not contained in the main beam or scattered and backscattered electrons from the sample (see Fig. 2.15). Furthermore, bremsstrahlung radiation and X-rays from within the specimen may generate spurious X-rays.

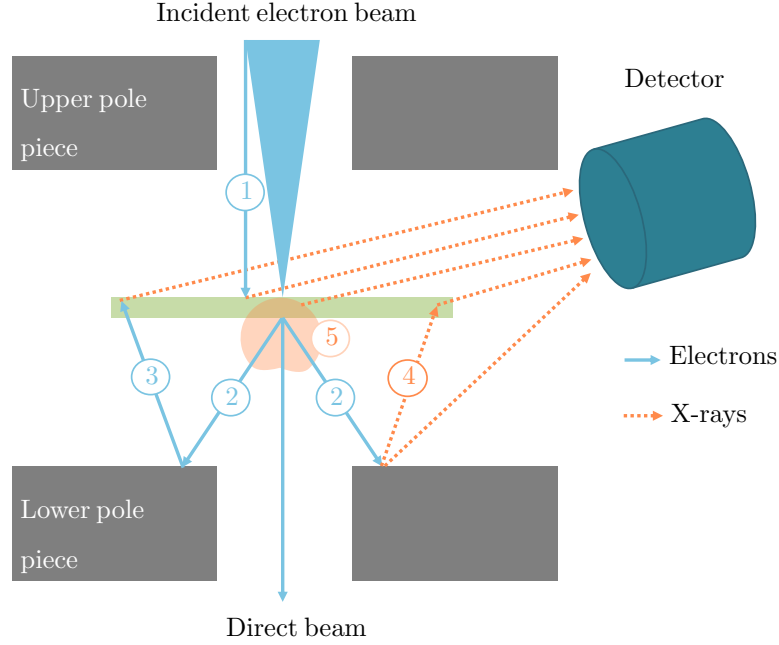


Figure 2.15: Illustration of some of the main contributing factors to unwanted stray radiation within the AEM column. 1) Electrons not confined within the incident beam. 2) Scattered electrons that may generate 3) backscattered electrons and 4) spurious X-rays, that in turn also can generate unwanted X-rays. 5) Bremsstrahlung radiation within the sample. (adapted from [11])

2.2.3 Quantitative EDS

Up until now, only the origin and physical behaviour of characteristic X-rays that enables qualitative determination of the sample composition have been discussed. A recorded EDS signal can also be used to get a quantitative analysis of the radiated area. The general idea is that the intensity of the generated X-rays will be proportionally dependent on the concentration as previously presented in Eqn. 2.4. This equation can be further developed for a more accurate description that applies in an EDS system where the X-ray intensity also will depend on instrument parameters such as the detector efficiency ϵ_A and the detector collection solid-angle $\Omega/4\pi$. Hence, the X-ray intensity can be summarized to be

$$I_A = \frac{N_v Q_A \omega_A a_A C_A}{A_A} \rho t D_e \frac{\Omega}{4\pi} \epsilon_A \quad (2.7)$$

From this expression, it can be seen that the X-ray intensity is dependent sample specific parameters such as the thickness and material specific constants such as cross section and fluorescence yield, in addition to the instrumental setup. Hence, the conversion from intensity to a quantitative composition is not straight forward. Additionally, I_A in Eqn. 2.7 is the intensity of

the characteristic peak above the background, which has to be dealt with. There are in general two main methods to subtract the background signal in an EDS spectrum. The first and most conventional way is to define two windows on each side of the peak where the average intensity is used to determine the background level. The alternative is to make a model of the spectrum by fitting all peaks to Gaussian curves. This method should be considered especially in the low energy range, where peaks are oftentimes close together and overlapping.

Over the last few decades, different methods have been developed in order to convert peak intensity to quantitative concentration values. This section covers the standard models, as well as a newly developed approach specifically made for compositional analysis of III-V heterostructures is presented. All the methods presented here are based on the assumption of a thin film specimen, while EDS for bulk samples in SEM are more demanding and will depend on using corrections for atomic number, absorption and fluorescence using other models and assumptions. However, the material sample studied in this work is a thin sample (~ 100 nm), and is assumed to fulfill the thin film assumption. The theory mainly based on [30] and chapter 35 in [11].

Cliff-Lorimer method

Using the generated X-rays within a specimen for elemental determination was first described by Hiller and Baker in 1944. Several years later, Castaing built and described the equipment to obtain quantitative data from bulk specimens [31]. By assuming that the concentration C_i of an element i generates a certain intensity of the characteristic X-rays, a reasonable approximation is

$$\frac{C_i}{C_{(i)}} = K \frac{I_i}{I_{(i)}} \quad (2.8)$$

where I_i is the measure intensity emerging from the specimen, $I_{(i)}$ is the measured intensity emerging from the standard. K is a sensitivity factor that corrects for the difference between the measured and the generated X-ray intensities, and is dependent on the atomic number, the absorption within the specimen, and the fluorescence of X-rays.

In 1975, Cliff and Lorimer further developed Castaing's model, and showed that it is not necessary to incorporate the intensity of a standard, but instead use the ratio between the intensities of two elements gathered simultaneously [10]. This was done by rewriting Equation 2.8 to a ratio between two elements, A and B

$$\frac{C_A}{C_B} = k_{AB} \frac{I_A}{I_B} \quad (2.9)$$

where k_{AB} is the Cliff-Lorimer factor, often called the k -factor. This model is based on the thin-foil criteria, which assumes the sample is thin enough to ignore absorption and fluorescence. In other words, it is assumed that all generated X-rays within the specimen is emitted and detected. By comparing Eqn. 2.9 with the previously stated relationship between the intensity of a characteristic

X-ray and the composition as seen in Eqn. 2.7, k_{AB} can be expressed as follows:

$$k_{AB} = \frac{A_A Q_B \omega_B a_B \epsilon_B}{A_B Q_A \omega_A a_A \epsilon_A} \quad (2.10)$$

In order to expand this model to a three component system, an extra equation is added:

$$\frac{C_B}{C_C} = k_{BC} \frac{I_B}{I_C} \quad (2.11)$$

and

$$C_A + C_B + C_C = 100\% \quad (2.12)$$

is used to extract the concentration values. Additionally, the k - factors for different pairs of elements are related by

$$k_{AB} = \frac{k_{AC}}{k_{BC}} \quad (2.13)$$

Therefore, k -factors can be specific relative to a pivot element, often Si. Then, the k -factor $k_{A,Si}$ is labeled k_A .

k -factors are not constants, but sensitivity factors that will vary depending on the detector, microscope, analysis conditions in addition to the choice of background subtraction and peak integration methods. Calculated standard k -factors exists, and can usually be extracted from the detector software in the instrument setup. It is also possible to determine k -factors experimentally by using a standard sample with known concentration. Experimentally determining k -factors is regarded as the most accurate practice, however it is also very time consuming and work. It requires a suitable homogeneous and stable thin film standard with known composition, and involves recording many spectra from different point on the specimen with sufficient count statistics, and is therefore seldom done. Either way, it is stated that quantitative EDS calculations with k -factors have an accuracy of $\pm 5\%$ at best [11].

Zeta-factor method

The ζ -factor method was developed by Watanabe and Horita to overcome the main drawbacks of the Cliff-Lorimer method [32]. First of all, the ζ -method does not rely on multi-element standards, but is a pure element method. Secondly, the method allows for simultaneous determination of the mass thickness, enabling a built in absorption correction.

The model is based on the following equation, relating the mass-thickness of the sample and the intensity, I_A , normalized by the composition, C_A :

$$\rho t = \zeta_A \frac{I_A}{C_A D_e} \quad (2.14)$$

Here, it is assumed that the intensity of the measured characteristic X-ray is proportional to the mass-thickness and composition in a thin film where absorption and fluorescence effects can be neglected. Comparing Eqn. 2.14 to the expression for X-ray intensity as described by Eqn. 2.7, the theoretical expression for the ζ -factor becomes

$$\zeta_A = \frac{A_A}{N_V Q_A \omega_A a_A (\Omega / (4\pi) \epsilon_A)} \quad (2.15)$$

As can be seen, the ζ -factors are independent of electron dose, specimen composition, density and thickness, and is dependent only on X-ray energy and accelerating voltage.

Seeing as the expression in Eq. 2.14 applies for a second element B , the compositions C_A and C_B and the mass-thickness ρt in a binary system where $C_A + C_B = 100\%$ can be expressed as

$$C_A = \frac{\zeta_A I_A}{\zeta_A I_A + \zeta_B I_B}, \quad C_B = \frac{\zeta_B I_B}{\zeta_A I_A + \zeta_B I_B}, \quad \rho t = \frac{\zeta_A I_A + \zeta_B I_B}{D_e} \quad (2.16)$$

This can be expanded to hold for a system with N elements in a similar manner as done for the Cliff-Lorimer method. Setting $C_A + C_B + \dots + C_N = 100\%$, the composition of element A becomes

$$C_A = \frac{\zeta_A I_A}{\sum_i^N \zeta_i I_i} \quad (2.17)$$

As mentioned, the beam-current has to be measured simultaneously as the EDS acquisition, which can be done *in-situ* with a Farady cup embedded in the specimen holder. However, this is not available in all AEMs, and this dependence on the beam current is considered the main drawback of the ζ -factor method. Nevertheless, if probe current measurements is possible, a great advantage with the method is being able to determine the mass-thickness of the specimen

Internal composition determination

The Cliff-Lorimer and the ζ -factor methods are the most widely used models for EDS quantification despite the lack of accuracy and practicalities associated with the need of sensitivity factors, sample thickness and/or probe-current. The need for an easy to use quantification model with high accuracy that does not rely on externally determined sensitivity factors as input parameters is therefore obvious. The factorless Internal Composition Determination (ICD) method was outlined by J. Nilsen in 2021 [15] to quantify ternary semiconductor compounds without relying on sensitivity factors. This is achieved through internally determining the composition within the specimen by using a known binary reference within the scan area for the ternary analysis area. Furthermore, the quantification is refined by incorporating that one element has a constant composition, and is called the benchmark element. In a ternary system $AB_{1-x}C_x$, A is used as the benchmark element. In addition to the underlying assumptions in the ζ -factor method, a key assumption in ICD is that the absorption

in the reference area is similar to the absorption in the region of interest. ICD is an iterative process based on the ζ -factor method, and a flow chart of the algorithm can be seen in Fig. 2.16.

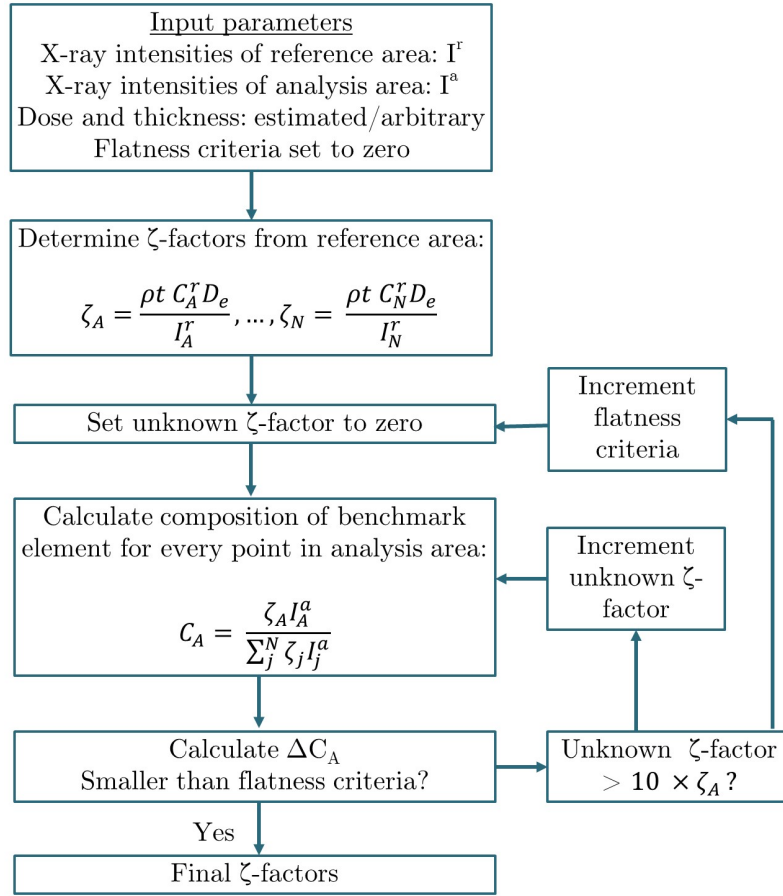


Figure 2.16: Flow chart displaying the incremental process of determining ζ -factors in the Internal Composition Determination method. Initially, the flatness criteria, ΔC_A is set to zero. In the system, element A, has a known constant weight fraction C_A , and the ζ -factors in the reference area can be calculated accordingly. Through the iterative process, a set of reasonable ζ -factors ($0-10\zeta_A$) for the unknown element is checked, while simultaneously increment the flatness criteria. The final ζ -factors gives the smallest possible fluctuations in C_A . (Reproduced from [15])

In order to use the ICD method, the scan area needs to include a reference area where $x = 0$, and the area of interest, referred to as the analysis area where $x \neq 0$. The first step in the ICD method is to extract the X-ray intensity for elements A and B from the reference area. Subsequently, ζ_A and ζ_B are calculated with Eqn. 2.14 using these line intensities, the known composition and arbitrary or estimated dose and thickness. The unknown ζ_C for element C is set to zero in the first iteration, and the composition of the benchmark element is calculated using Eqn. 2.14 in the scanned area. Through the iterative process, the value for ζ_C is determined to minimize the fluctuations in the benchmark element. For each iteration, the value for ζ_C is incremented, the composition of the benchmark element calculated and compared to a flatness criteria, ΔC_A . The

flatness criteria is defined as the difference between the composition maxima and minima of the benchmark composition such that $\Delta C_A = C_A^{max} - C_A^{min}$. If the flatness criteria is not met before the value for ζ_C becomes unreasonably large, e.g. ten times larger than ζ_A , the flatness criteria is also incremented, and the process starts again. Finally, the resulting ζ -factors is used to calculate the composition in both analysis and reference area. As can be seen in Fig. 2.16, a thickness and probe current is set by the user. Using these values, the thickness profile can be reconstructed, but the absolute thickness will only be correct if the input parameters are correct. Nevertheless, it will return a relative thickness profile which can be compared to the expected thickness profile and used for validation of the quantification results.

2.2.4 EDS setup and detector characterization

The aim of this work is to improve quantification of EDS data, which requires to carry out a characterization of the EDS system to know fundamental detector performance parameters that might affect the spectra and consequently the quantification. This is commonly done using a standard test specimen consisting of a NiO thin film on a Mo grid. The tests are described by Watanabe in [30] and in the info-sheet by Ted Pella [33] which is based on the original work by R.F. Egerton and C.S. Cheng from 1994 [16]. The complete test routine has several characteristics. Here only the most essential to this work are discussed, and an overview is found in Tab. 2.3.

Characterization parameters

Energy resolution

To achieve accurate composition analysis, good energy resolution, i.e. the ability to distinguish different energies from each other, is required. The measured X-ray usually have a line width of $\gg 100$ eV, while theoretically the X-rays have a line width of a few eV. Electronic noise is the main cause for the difference between practical and theoretical energy resolution. A detector's energy resolution is defined as the full-width at half maximum (FWHM) value at the $Mn_{K\alpha}$ peak position (5.9keV). This can be derived from the FWHM value of $Ni_{K\alpha}$ peak in the following manner: [34]

$$FWHM(MnK\alpha) = 0.926FWHM(NiK\alpha). \quad (2.18)$$

The factor of 0.926 corrects for the change in peak width with energy, and is based on several detector measurements. The value for FWHM is best found by fitting the peak to a Gaussian.

Energy resolution is highly dependent on the dead time, which in turn is determined by the process time chosen in the EDS system software. Dead time is the time allowed for the processor to evaluate the magnitude of the charge pulse and can be altered in the computer software controlling the detector. The energy resolution is degraded with shorter dead time. The energy resolution is determined by electronics and typical energy resolution for most EDS detectors is 130 eV.

Peak shape

How well the peak shape, S , is fitted to a Gaussian is measured by the ratio of full width at tenth maximum (FWTM) to FWHM.

$$S = \frac{FWTM(NiK\alpha)}{FWHM(NiK\alpha)} \quad (2.19)$$

For an ideal Gaussian peak, the ratio is 1.83. Typically, the $Ni_{K\alpha}$ peak has $S \sim 2$, and larger values may indicate peak tailing. This can be caused by incomplete charge collection (ICC). ICC originates from the p and n regions of the detector, which are often referred to as the dead layer, while the intrinsic region is the active region. In the p and n regions, there is a high rate of electron-hole pair recombination, rendering these regions effectively unresponsive to the incoming X-rays.

Stray radiation

The presence of stray electrons and X-rays in the AEM column can be evaluated by measuring the inverse hole count (IHC). This is defined as the intensity ratio above background of a major X-ray line in the specimen, here the $Ni_{K\alpha}$ line, to an X-ray line from the grid material, here the $Mo_{K\alpha}$ line,

$$R_{NiK\alpha/MoK\alpha} = \frac{I(NiK\alpha)}{I(MoK\alpha)} \quad (2.20)$$

In the ideal setup, the intensity of the $Mo_{K\alpha}$ peak is zero, seeing as it originates from the grid and not from the sample material of interest. Accordingly, higher values for $R_{NiK\alpha/MoK\alpha}$ denotes a column with less stray and spurious X-rays causing unwanted signals in the EDS spectrum. As previously described, strays from the AEM column, the holder and the detector can be a serious problem, especially if the strays overlap with the X-ray lines to be used in compositional determination. The type of stray radiation present in the EDS setup can easily be identified using the NiO sample, as the composition of the sample is well known.

Predominant source of stray radiation

The origin of the stray radiation may be evaluated using the ratio of $Mo_{K\alpha}$ and $Mo_{L\alpha}$ above background:

$$R_{MoK\alpha/MoL\alpha} = \frac{I(MoK\alpha)}{I(MoL\alpha)} \quad (2.21)$$

If the predominant source of stray radiation is X-rays, this would produce a high $R_{MoK\alpha/MoL\alpha}$. High energy Bremsstrahlung X-rays have a higher probability of generating the high energy $Mo_{K\alpha}$ line, while stray electrons have a higher probability of generating the $Mo_{L\alpha}$ line instead.

Peak-to-background ratio

In addition to Bremsstrahlung radiation, the background can also have contributions from electrons outside the probe, from the EDS electronics and from column X-rays. A high peak-to-background, P/B, ratio often indicates a good configured EDS system. The P/B ratio is most commonly defined as the ratio between the full peak intensity including the background, and the background intensity with the same energy window as the peak. Seeing as the energy resolution can differ between spectrometer systems, the P/B ratio should be found by the Fiori definition in order to compare instruments. In the Fiori definition, the average background intensity at a single channel is used instead of the total background within the energy window [35]. The expression for the Fiori P/B_F ratio becomes

$$P/B_F = c_F \frac{I(NiK\alpha)}{B(NiK\alpha)} \quad (2.22)$$

where the factor $c_F = \Delta/\delta$, where Δ is the width of the energy window and δ is the width of one channel.

Calibration of energy scale

Calibrating the energy dispersive range is done using the low energy O_{Kα} peak at 0.525 keV, the Ni_{Kα} peak at 7.47 keV in the middle energy range, and the high energy Mo_{Kα} peak at 17.42 keV. By comparing the maximum value of each peak to its aforementioned theoretical value, the energy scale can be calibrated for incorrect dispersion. Calculating the correct channel dispersion can be approached in different ways. Here, it is found by doing a linear fit of the peaks deviation from the theoretical value versus the theoretical value of the peak. Then, the slope of the linear function is subtracted from the original channel width, which will result in the true energy scale of the spectrum.

Shadowing effects with tilting

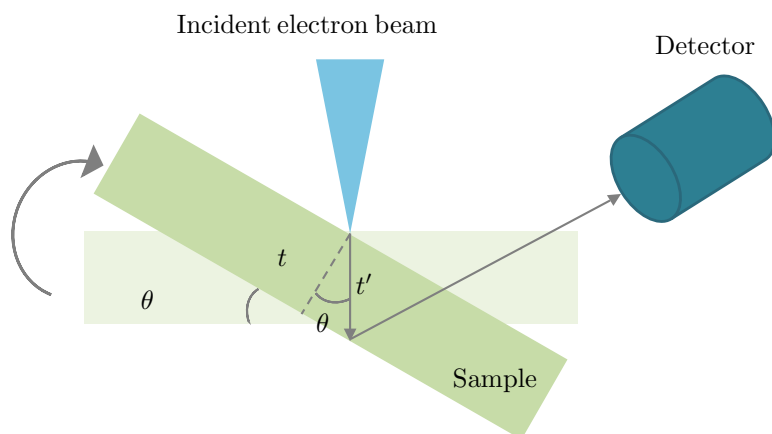
When the specimen is tilted in the AEM stage, the projected thickness, t' , will increase as seen in Fig.2.17a. The increase in t' with increasing tilt angle, θ , is related by

$$t' = \frac{t}{\cos \theta}, \quad (2.23)$$

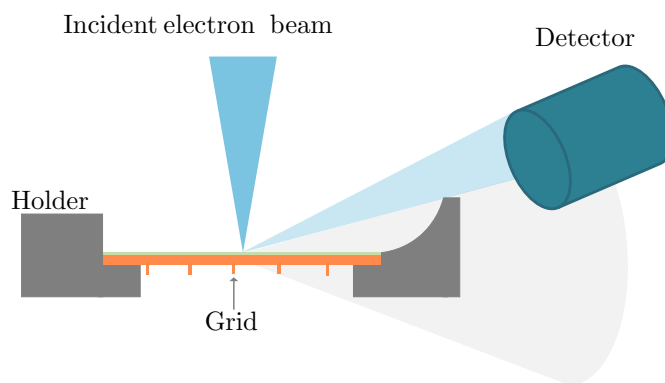
where t is the thickness of the specimen. Taking only the increase in the projected length within the specimen into account, the intensity of the recorded X-ray signal as described by Eqn. 2.4, would have an increase proportional to $1/\cos \theta$.

Shadowing by the grid bars and holder commonly occur, and cause a significant decrease in X-ray signal intensity with decrease of θ (see Fig. 2.17b). The tilt angle, θ , where shadowing occurs can be found by recording a spectra in the middle of a grid square at increasing tilt angle. Plotting

the intensity of a significant peak from the sample versus tilt angle will reveal the angle at which the $1/\cos\theta$ behaviour cease, and shadowing becomes substantial.



(a)



(b)

Figure 2.17: (a) Illustration of how the projected thickness t' in a TEM sample increase according to $t/\cos\theta$, where θ is the tilting angle and t is the thickness of the sample. (b) A substantial decrease in the count rate of a recorded EDS spectrum suggests shadowing from the grid bars or the holder as shown in the figure.

Table 2.3: Overview of all the features and tests performed during characterization of EDS system in this work.

Feature	Parameter/ratio	Description
Energy resolution	$0.926FWHM(NiK\alpha)$	The detectors ability to distinguish different X-ray lines from each other. Typical value is 130 eV.
Peak shape	$S = \frac{FWTM(NiK\alpha)}{FWHM(NiK\alpha)}$	For a perfect Gaussian peak, $S = 1.83$. Values > 2.0 may indicate peak tailing, due to incomplete charge collection.
Stray radiation	$R_{NiK\alpha/MoK\alpha} = \frac{I(NiK\alpha)}{I(MoK\alpha)}$	Measurement of stray electrons and X-rays in the column. Typical values range between 3 to 7 in conventional TEM.
Source of stray radiation	$R_{MoK\alpha/MoL\alpha} = \frac{I(MoK\alpha)}{I(MoL\alpha)}$	High ratio (order of 100) indicates X-rays are main source of column radiation. If high energy electrons are predominant, the value is lower in the order of 1-10.
P/B characteristics	$P/B_F = \frac{I(NiK\alpha)}{B(NiK\alpha)}$	Total EDS background measured by the ratio of total intensity of peak divided by intensity of background. Should be at least 1000.
Energy calibration	Position of $O_{K\alpha}$, $Ni_{K\alpha}$ and $Mo_{K\alpha}$	Deviation of the peak maximum from theoretical value is used to find true energy channel scale (usually 10 eV as default).
Tilting effects	$I(NiK\alpha)$, $I(OK\alpha)$	Measured at different tilts to find at which tilt angle shadowing of the detector is minimized.

2.3 Crystallography

Generally, III-V semiconductor compounds used in photoelectric devices are crystalline materials. While inelastically scattered electrons gives rise to composition and band structure information of a specimen, elastically scattered electron contain information on the materials crystal structure through diffraction patterns (DP). Here, a general introduction to crystal structures and diffraction is given based on [36].

2.3.1 Crystal structures

Crystals are materials that are made up of an infinite repetition of identical atom groups referred to as the basis. The lattice is the set of mathematical points where the basis is attached. In three dimensions, the lattice is defined by the translation vectors \mathbf{a}_1 , \mathbf{a}_2 and \mathbf{a}_3 such that

$$\mathbf{R} = u_1\mathbf{a}_1 + u_2\mathbf{a}_2 + u_3\mathbf{a}_3 \quad (2.24)$$

where, u_1 , u_2 and u_3 are arbitrary integer numbers, and \mathbf{R} is a lattice point.

In addition to defining the crystal axes and basis, it is helpful to identify planes and directions in the crystals. Miller indices are used for this purpose, where a plane is represented as (hkl) . h , k and l are the points at each crystal axis where the plane intersects, multiplied by their common denominator if this leads to fractions. To denote a family of planes, i.e. a set of equivalent planes, curly brackets are used. $[hkl]$ is used to represent the direction perpendicular to the plane.

There are fourteen different Bravais lattices in seven crystallographic systems in three dimensions. One of these systems is the cubic system, which are defined by having $a_1 = a_2 = a_3$ and $\alpha = \beta = \gamma = 90^\circ$, where α , β and γ are the angles between the crystal axes as seen in Fig. 2.18a. The unit cell of a crystal is the smallest repeating unit of the lattice, and can contain one or more lattice points. The unit cell can contain one or more lattice points. In the cubic system, the face-centered cubic (FCC) crystal structure has 4 lattice points in each unit cell, and can be seen in Fig. 2.18b.

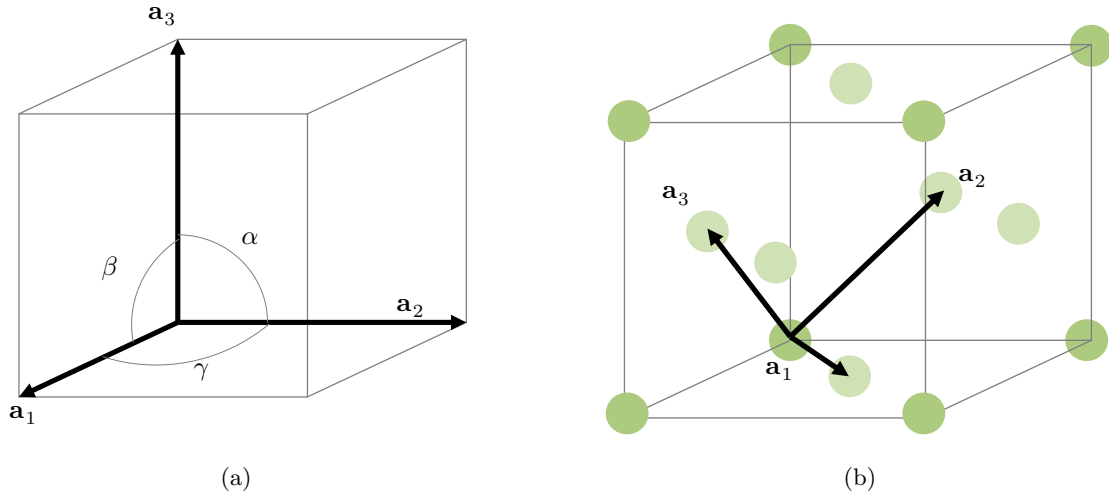


Figure 2.18: (a) Cubic structure with the crystal axes and angles indicated, defined by $a_1 = a_2 = a_3$ and $\alpha = \beta = \gamma = 90^\circ$. (b) FCC crystal structure where lighter orange colored are the face located atoms for better visualization.

The arrangement of atoms in a lattice can be viewed as packing layers of hard spheres. One way of placing the spheres which maximizes the packing fraction is the FCC structure. In each layer, all spheres are in contact with six others in the plane. The second layer B) is placed on top of the first layer (A) by placing each sphere in layer B in contact with three others in A. In the FCC structure, a third layer is added over the holes in layer A that are not occupied by B and creates an ABCABC packing.

Zinc Blende

There could be several atoms on a lattice position. For example, with FCC lattice, but instead of a single atom, there could be two. Examples are silicon with the diamond structure, where there are two Si atoms, displaced $1/4$ of the cubic body diagonal. Another example is kitchensalt, with Na and Cl displaced $1/2$ of the side facets. For III-V semiconductors, Zinc Blende (ZB) is a common crystal structure. It has a stacking as FCC, with ABC stacking in the body diagonal direction ([111]), and two different atoms on a lattice position. The stacking can be noted as AaBbCc, to note that the close-packed layers are different, but the lattice stacking is like seen in FCC. An example relevant to this work is cubic GaAs. The atomic coordinates in a ZB crystal unit cell with these atoms in each lattice point is accordingly

$$\begin{aligned}
 \text{Ga:}(x, y, z) &= (0, 0, 0), \left(\frac{1}{2}, \frac{1}{2}, 0\right), \left(\frac{1}{2}, 0, \frac{1}{2}\right), \left(0, \frac{1}{2}, \frac{1}{2}\right) \\
 \text{As:}(x, y, z) &= \left(\frac{1}{4}, \frac{1}{4}, \frac{1}{4}\right), \left(\frac{3}{4}, \frac{3}{4}, \frac{1}{4}\right), \left(\frac{3}{4}, \frac{1}{4}, \frac{3}{4}\right), \left(\frac{1}{4}, \frac{3}{4}, \frac{3}{4}\right)
 \end{aligned} \tag{2.25}$$

The crystal structures of semiconductor materials often resemble the FCC crystals. They can be viewed by positioning a III group atom at the already established lattice points, and adding a group V atom to the basis. For III-V bulk semiconductors such as GaAs, AlAs and GaSb, the cubic ZB configuration is most common. In Fig. 2.19, some of the crystal planes and their respective atomic arrangements relevant to this work are shown. The ABC stacking can be broken up by planar lattice defects which is called twinning. Here, the stacking order is reversed. It can be described as ABCAB”C”BACBA where ”C” is common plane in both parts and called the twinning plane. A twin can be seen as a reflectoin in a twinning plane or a rotation around the twinning axis (here [111]).

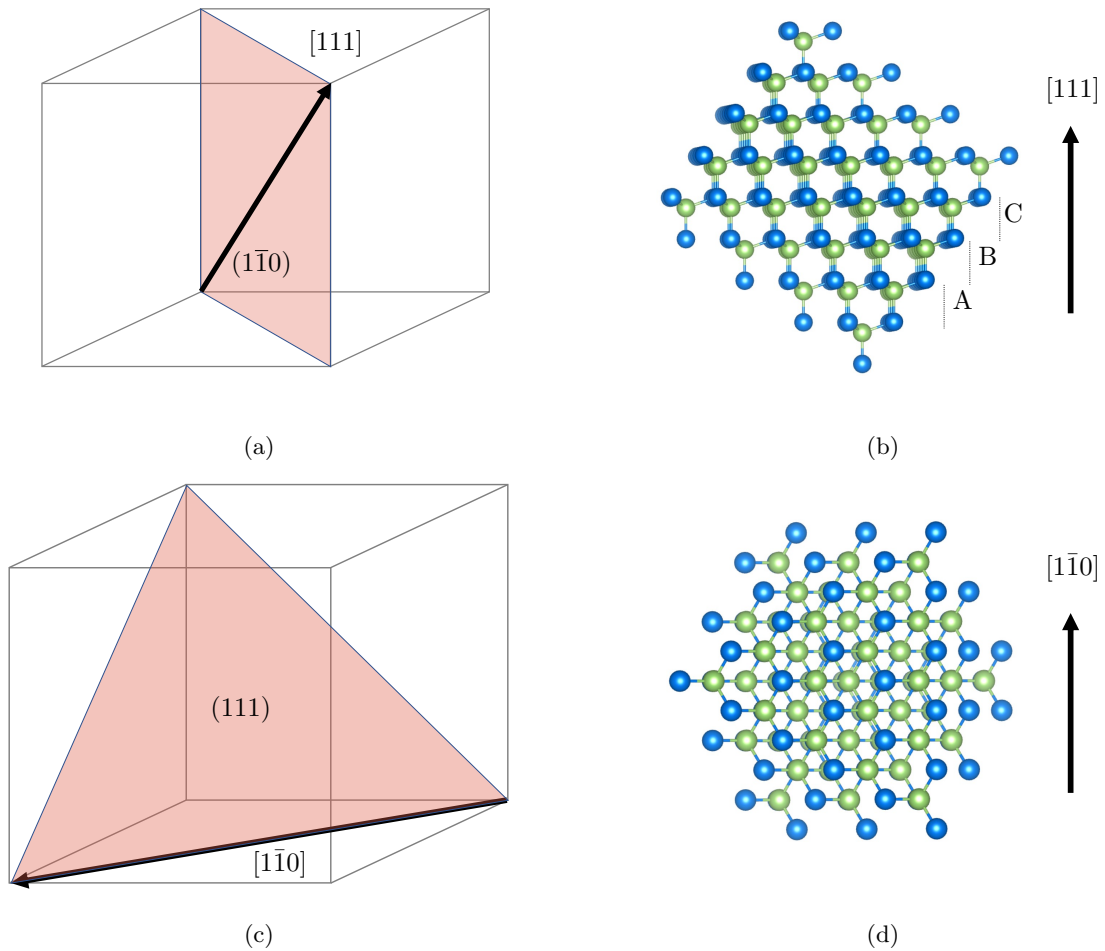


Figure 2.19: Cubic crystal where the (a) (110) and (c) (111) planes are indicated along with the (b) atomic arrangement of (110) planes tilted slightly off-zone to show how the atoms are arranged in Ga and As columns. Also indicated is the ABC stacking of two and two As (blue) and Ga (green) with the [111] (i.e. growth direction in GaAs NWs) indicated. (d) the atomic arrangement of (111) plane with indicated upward crystal vector. Atomic arrangements are modelled in Vesta [37].

2.3.2 Reciprocal lattice

It is also useful to express crystals in reciprocal space, where the reciprocal lattice vectors in three dimensions are defined as

$$\begin{aligned}\mathbf{b}_1 &= 2\pi \frac{\mathbf{a}_2 \times \mathbf{a}_3}{\mathbf{a}_1 \cdot \mathbf{a}_2 \times \mathbf{a}_3}, \\ \mathbf{b}_2 &= 2\pi \frac{\mathbf{a}_3 \times \mathbf{a}_1}{\mathbf{a}_1 \cdot \mathbf{a}_2 \times \mathbf{a}_3}, \\ \mathbf{b}_3 &= 2\pi \frac{\mathbf{a}_1 \times \mathbf{a}_2}{\mathbf{a}_1 \cdot \mathbf{a}_2 \times \mathbf{a}_3}.\end{aligned}\tag{2.26}$$

Here, \mathbf{a}_1 , \mathbf{a}_2 and \mathbf{a}_3 are the primitive lattice vectors in real space as defined by Eqn. 2.24. The reciprocal lattice operator \mathbf{G} , is then defined as

$$\mathbf{G} = h\mathbf{b}_1 + k\mathbf{b}_2 + l\mathbf{b}_3\tag{2.27}$$

On this form, \mathbf{G} maps out the reciprocal space of the lattice. This is essentially the Fourier transform of the real crystal lattice. A point described by Equation (2.27) in reciprocal space represents the set of hkl planes in real space. It also follows that

$$\mathbf{a}_i \cdot \mathbf{b}_j = 2\pi\delta_{ij}\tag{2.28}$$

since one reciprocal lattice vector is orthogonal to the other two in real space.

2.3.3 Diffraction

Electron diffraction constitutes the basis for imaging and characterization of crystal structures and structural properties of a specimen in TEMs. An understanding of wave diffraction is crucial before tackling the inner workings of such instruments. Diffraction has been defined as an interaction between a wave of any kind and an object of any kind. More precisely, it is a deviation in the direction of a wave at the edge of an obstacle in its path. Different laws and conditions to explain diffraction have been derived and are presented here. The theory is in large part based on [36], unless otherwise stated.

Bragg's law and diffraction conditions

Bragg derived a simple explanation of the diffracted beam from a crystal by viewing the crystal planes as mirrors that reflect a portion of the incoming beam, as seen in Fig. 2.20.

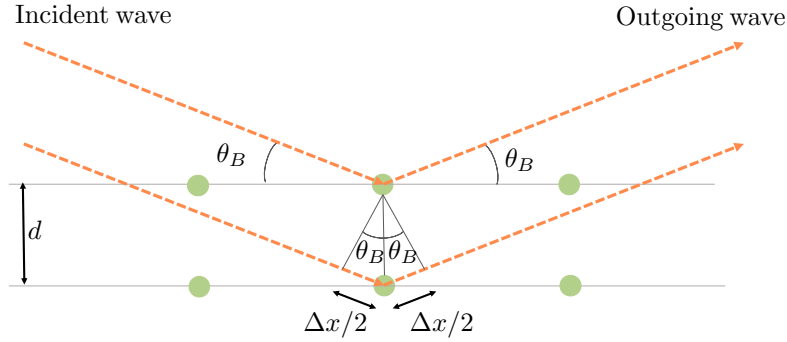


Figure 2.20: Scattering of an incident wave on atomic planes separated by a distance d , as described by Bragg. The wave is incident on the plane with an angle θ_B . The total path difference between the upper and lower reflected wave is Δx as indicated.

The diffracted beam is found when the out coming wave of two parallel planes have a path difference equal to an integer, n , of the wavelength, creating constructive interference. Bragg's law states that

$$2d \sin \theta_B = n\lambda \quad (2.29)$$

where d is the spacing between planes and θ_B is Bragg's angle. Hence, when the wavelength is known, the plane spacings can be deduced.

Even though Bragg's law provides a simple picture of the diffraction phenomena, it does not directly apply to real situations. A representation of kinematic scattering in reciprocal space can be more practical in analyzing electron diffraction. In kinematic diffraction theory, where only one scattering event is assumed to take place, the difference in the incoming, \mathbf{k} , and outgoing wave, \mathbf{k}' , i.e. the scattering vector is

$$\Delta \mathbf{k} = \mathbf{k}' - \mathbf{k} \quad (2.30)$$

By assuming that the amplitude of the scattered wave is proportional to the local electron concentration, $n(\mathbf{r})$, the *scattering amplitude* is defined as

$$F = \sum_{\mathbf{G}} \int dV n_G e^{-i(\mathbf{G} - \Delta \mathbf{k}) \cdot \mathbf{r}} \quad (2.31)$$

where, the Fourier transform is over the reciprocal lattice vectors, \mathbf{G} , and n_G is the Fourier components of the electron density. It can be shown that this expression vanished whenever $\Delta \mathbf{k}$ deviates significantly from \mathbf{G} . Subsequently, it is established a diffraction condition

$$\Delta \mathbf{k} = \mathbf{G} \tag{2.32}$$

which is a central result for elastic scattering of waves on a periodic lattice. This equation states that the pattern of the diffracted beam is in fact a representation of the lattice reciprocal space. The diffraction condition in Eqn. 2.32 is essentially Bragg's law, but in reciprocal space, and gives the first condition that has to be fulfilled in order to see a diffracted beam.

Laue equation and Ewald sphere

The diffraction condition in Eqn. 2.32 can be expressed on another form:

$$\begin{aligned} \mathbf{a}_1 \cdot \Delta \mathbf{k} &= 2\pi v_1, \\ \mathbf{a}_2 \cdot \Delta \mathbf{k} &= 2\pi v_2, \\ \mathbf{a}_3 \cdot \Delta \mathbf{k} &= 2\pi v_3, \end{aligned} \tag{2.33}$$

where, v_1 , v_2 and v_3 are integers. These are called Laue equations and are additional requirements Δk must satisfy in order to see the diffraction pattern. The geometrical interpretation of these equations is that Δk must lie at a common line of intersect of three cones. This can be visualized by the Ewald sphere as seen in Fig. 2.21.

In traditional electron microscopes, the wavelength of the electrons is in the nanometer range, which means that the radius of the Ewald sphere will be large, and several diffraction spots is visible at the same time. Additionally, in real systems, a lattice is not infinite as we have previously assumed, but have a finite size and less repetitions in the incoming beam direction. Material samples analysed with electron diffraction, are typically < 100 nm thick. This leads to an elongation/broadening of the diffracted spots in reciprocal space, or so-called relrods. This can be described by a deviation parameter, \mathbf{s} , such that the diffraction condition becomes

$$\Delta \mathbf{k} = \mathbf{G} + \mathbf{s}. \tag{2.34}$$

This means that more diffraction spots will cross the Ewald sphere and will fulfill the required conditions as seen in Figure 2.21, and are observed simultaneously in a diffraction pattern.

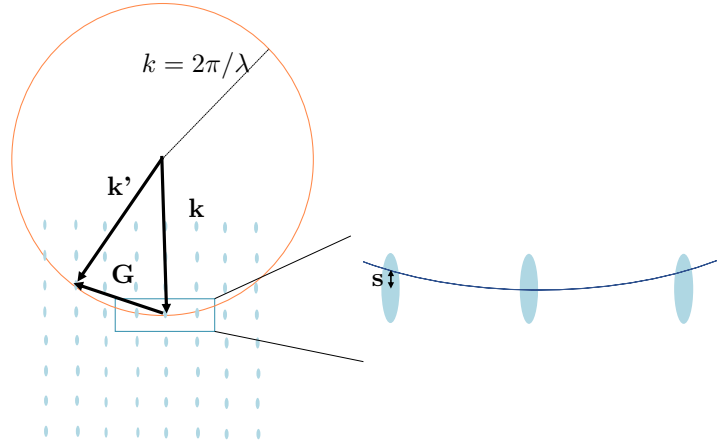


Figure 2.21: Schematic illustration of the construction of Ewald sphere. The blue dots represent reciprocal space of the crystal. The incident beam vector, \mathbf{k} , and the diffracted beam which fulfills the diffraction condition and Laue equations, \mathbf{k}' , are indicated. The radius of the sphere is $k = 2\pi/\lambda$, where λ is the wavelength of the electrons. Adapted from [36]. To the right showing rod shaped diffraction spots caused by the finite shape of a crystal. The deviation parameter, s , here defined as negative, is indicated and allows more diffraction spots to fulfill the diffraction conditions.

Structure factor

In addition to the diffraction condition in Eqn. 2.32 and Laue Eqn. 2.33, the structure factor, $S_{\mathbf{G}}$, is a geometrical quantity that needs to be considered. The structure factor is defined as

$$\begin{aligned}
 S_{\mathbf{G}} &= \sum_j f_j \exp(-i\mathbf{G} \cdot \mathbf{r}_j) \\
 &= \sum_j f_j \exp[-i2\pi(hx_j + ky_j + lz_j)]
 \end{aligned}
 \tag{2.35}$$

Here, the sum is over all atoms, j , in the basis, and the second equality is obtained using Equation (2.28). Additionally, a new quantity, f_j , is introduced. This is the atomic form factor of the basis, and is a measure of the contribution to the total scattering amplitude by atom, j . The interpretation of the structure factor is that its absolute value squared, $|S_{\mathbf{G}}|^2$ represents the intensity of the coherently scattered wave. For a given basis, some combinations in \mathbf{r}_j and \mathbf{G} will leave the structure factor zero, meaning that the diffracted spots has no intensity. Such \mathbf{G} 's are considered forbidden reflections in kinematic diffraction theory and should by this definition not be visible in the diffraction pattern.

For ZB crystals, the atoms in the basis have positions according to Eqn. 2.25. It can be shown that the structure factor for ZB is as follows:

$$S_{\mathbf{G}}^{ZB} = \begin{cases} 0 & \text{if } h, k \text{ and } l \text{ are mixed} \\ 4(f_{Ga} - if_{As}) & \text{if } h, k \text{ and } l \text{ are all odd and } h + k + l = 4n + 1 \\ 4(f_{Ga} + if_{As}) & \text{if } h, k \text{ and } l \text{ are all odd and } h + k + l = 4n + 3 \\ 4(f_{Ga} - f_{As}) & \text{if } h, k \text{ and } l \text{ are all even and } h + k + l = 4n + 2 \\ 4(f_{Ga} + f_{As}) & \text{if } h, k \text{ and } l \text{ are all even and } h + k + l = 4n \end{cases} \quad (2.36)$$

For a detailed derivation, see [38]. As can be seen, the expression is zero for all combinations whenever h , k and l are mixed. This means that for example the 100 reflection is kinematically forbidden, while the 111 and 002 reflection is visible. Further, assuming the kinematic approximation applies, it can be seen that the structure factor, and hence the intensity varies and is related to the atoms, i.e. the factor $f_{Ga} \pm f_{As}$. If composition of III atom position varies, as it does in for example $\text{Al}_x\text{Ga}_{1-x}\text{As}$, elastic diffraction can be used to analyse composition. In this work, this route is not further explored, as the focus lies on analyzing the composition using inelastic scattering and emission spectroscopy.

2.4 Electron microscopy

With the continuous downscaling of features sizes in technology, the need for characterization tools which provide a higher spatial resolution than what is obtainable in optical microscopes, has motivated the development of electron microscopy. Optical microscopes have a maximum obtainable resolution, due to the wavelength of photons. This is given by Rayleighs criterion, which describes the smallest distance that can be resolved, δ , in terms of the wavelength of the photons, λ , the refractive index of the viewing medium, μ , and the semi-angle of collection of the magnifying lens, β , as follows:

$$\delta = \frac{0.61\lambda}{\mu \sin \beta} \quad (2.37)$$

. In terms of this classic criterion, much higher resolution is obtainable by exploiting electrons' particle-wave duality. Electrons have a wavelength, λ , related to their energy, E by

$$\lambda = \frac{h}{\sqrt{2m_e eV}} \quad (2.38)$$

where h is Plancks constant, m_e is the mass of the electron, e is the elemental charge and V is the acceleration voltage in the microscope. When the velocity of the electrons becomes more than half of the speed of light, (as it does in most electron microscopes), relativistic effects have to be taken into account. Eqn. 2.38 is modified, and the wavelength is given by

$$\lambda = \frac{h}{\sqrt{2m_e eV \left(1 + \frac{eV}{2m_e c^2}\right)}} \quad (2.39)$$

Table 2.4: Non-relativistic and relativistic electron wavelength calculated by Equation 2.38 and 2.39 respectively, at relevant acceleration voltages often operated in electron microscopes.

Accelerating voltage [kV]	Non-relativistic wavelength [nm]	Relativistic Wavelength [nm]
1	0.03881	0.03879
10	0.01227	0.01221
30	0.00709	0.00698
100	0.00388	0.00370
200	0.00274	0.00251

As can be seen in Table 2.4, the relativistic and non-relativistic wavelengths deviate more for higher voltages, but the main giveaway is that the electron wavelength becomes comparable to typical lattice parameters for the listed energies. Hence, exploiting the electrons wave-like behaviour constitutes the basis for observing micro- and nanoscale features in a sample. As described in Sec. 2.2, an assortment of signals is generated within a sample material whenever a high energy electron beam is incident on the sample. In the following sections, the origin of these, and the information they hold is described. The theory is mainly based on [11] and [39].

2.4.1 Scanning electron microscope

A traditional Scanning Electron Microscope (SEM) is operated by focusing the accelerated electron beam (typically 130 kV) to a probe on the sample surface. The beam is then scanned over the surface, creating secondary electrons (SE) and backscattered electrons (BSE), the main two signals used to image the scanned area. These signals exit above the sample, and is recorded for each probe position, resulting in an image of the sample with different contrasts.

Secondary electrons

Secondary electrons are created through inelastic scattering between incident beam electrons and valence electrons in the sample. As valence electrons are weakly bound to the atom and have a low ionization energy (1-15 eV), compared to the energy of the incident electrons (1-200 kV depending on the instrument), the energy transfer from the primary electron to the SE is small. After escaping the atom, the SE move through the material, and undergo further inelastic scattering, which continues to decrease their kinetic energy. The depth from which a SE can escape the sample, d_{esc} will depend on the initial energy of the incident beam, the depth of the generation and the type of host material. Nevertheless, only SE near the surface have a significant chance to escape, and the signal is utilized for topological information. As seen in Fig. 2.22 (b), the number of SE that are able to escape the sample increase with surface inclination, as it is easier for electrons to escape when the sample is tilted relative to the beam, producing topological contrast.

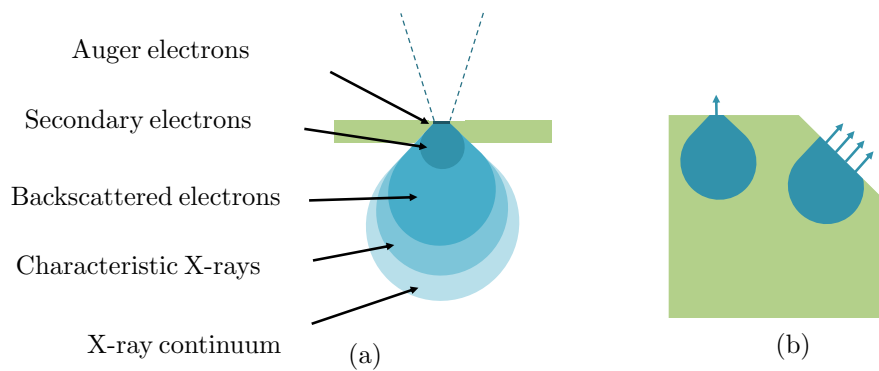


Figure 2.22: Schematic illustration of (a) the interaction volume and origin of the different signals generated by the incoming electron beam in a SEM relevant to this work and (b) how secondary electrons give rise to a topography contrast.

Backscattered electrons

If a primary electron undergoes a sufficient amount of elastic scattering events to reverse its trajectory, the electron can resurface near the point of entrance and escape the material. Such electrons are referred to as backscattered electrons, and provide an atomic number contrast. The scattering events are caused by repulsive forces from the atoms' orbital electrons, which means that the probability of an elastic scattering event increases with increasing atomic number, Z , of the sample. Areas in the sample with a higher atomic number will generate a higher intensity of BSE electrons and will be depicted as brighter in the computer-generated image. BSE originate from the beam, which is accelerated with voltages in the keV range. They have a much higher energy than SE, which only have a few eV kinetic energy, and can therefore travel for longer distances before escaping the material. The penetration depth of BSE can range up to thousands of nanometers, and will consequently lead to a lower obtainable spatial resolution.

The instrument

The conventional operating voltage in typical SEMs are 1-30 kV. The electron beam is generated from an electron source placed at the top of the column in which the electron travels. In general, there are two types of electron sources. Thermionic sources generate electrons through heat, and the field emission source generates electrons by producing a large electric potential between the source and an anode. Subsequently, an electron gun accelerates and focuses the electrons towards the sample chamber.

After the electrons exit the gun, they pass through an assembly of electromagnetic lenses and apertures. The lenses consist of an assembly of copper coils, with a current running through them, creating a magnetic field along the optical axis. The electrons interact with the field due

to the Lorentz force, creating a circular motion, and are bent depending on the strength of the field. Apertures are usually circular holes in metal disks, and is added to the lenses to limit the collection angle and reduce aberrations. Lastly, the electron beam passes through a set of scanning coils, which purpose is to deflect the beam in order to scan the sample. A schematic illustration of the basic setup in a SEM is shown in Fig. 2.23. The signal from the electron specimen is collected by a set of detectors, which are most commonly SE and BSE detectors placed above the sample.

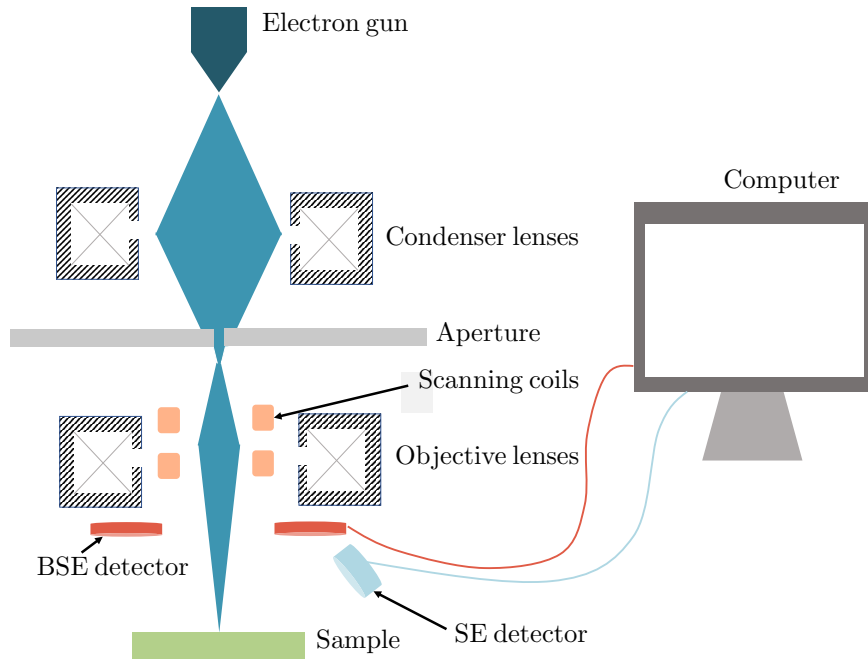


Figure 2.23: Schematic illustration of the components in a typical SEM. The electron gun generates an electron beam which travels through a system of electromagnetic lenses and apertures and is deflected by scanning coils towards the sample. The signal is detected by a set of detectors, and a final image is shown on the computer.

2.4.2 Transmission electron microscope

Transmission electron microscopes have similar set-ups as SEMs, but there are some core differences between the two. First of all, the electrons in a TEM is accelerated at much higher voltage ranges, 100-400 kV. Since the incoming electrons have such high energies, they transmit through the sample at a much higher degree than in SEMs, assuming the specimen is thin enough ($< \sim 200$ nm). In SEMs, the electron beam is focused to a point on the sample, while in traditional TEM mode, the incoming beam is broad and parallel at the sample surface. At $\times 20k$ - $\times 100k$ magnification, the beam illuminates typically several micrometers of the sample. The image is created by simultaneous collection from the illuminated specimen area, and not acquired pixel by pixel.

The instrument

The main components of TEM hardware consists of an electron source, a condenser system, an objective system, intermediate and projector lenses and a recording device (see Fig. 2.24). The condenser lenses are placed above the specimen and creates the electron beam which hits the sample. The objective lenses are placed under and very close to the specimen and creates the image. Then the next set of intermediate and projection lenses transfer the image to the recording screen.

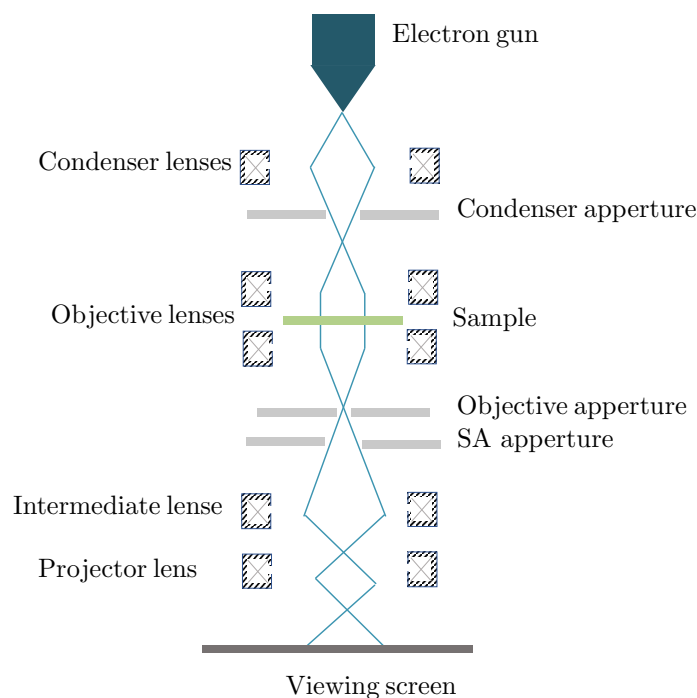


Figure 2.24: Schematic illustration of the main components in a TEM column. Here, deflectors, stigmators for beam tilt and shift and beam symmetry respectively is omitted.

The most important limitations to spatial resolution in TEM are lens imperfections. A perfect lens focuses the incoming rays to the exact same point, but in reality this is only true for the electrons close to the optical axis (OA) since the lens power varies from the center to the edges of the lens. This causes spherical aberrations and is minimized by inserting apertures, which limit the angular distribution of the electron beam. There are typically three apertures in a TEM column. The condenser aperture limits the angular spread of the beam hitting the sample and keeps electrons close to OA. This improves resolution, but also lowers the intensity. The objective aperture limits the angular spread of the beam from the sample in the back focal plane (BFP) and selects which scattering angles that contribute to the image. The selected area aperture is placed in the image

plane and selects which area of the specimen that contributes to the diffraction pattern. Another limitation is astigmatism. Astigmatism is the effect which causes round objects to appear elliptical and is compensated by using deflectors and stigmators.

Bright-field

Bright-field imaging of the sample maps the specimen using the direct beam only. This is done by focusing the intermediate lens on the image plane of the objective lens. However this leads to little contrast in the image, because all diffracted and transmitted rays are carried through the lens system and gathered at the viewing screen. The objective lens focuses all beams that are scattered with the same angle in the same spot in the lenses BFP. This means that the image in the BFP is essentially the DP of the illuminated sample, and each spot in the BFP includes signal from every point in the sample. By inserting an objective aperture selecting only a certain beam in the BFP, a full image of the specimen is still formed on the viewing screen, and an increased contrast is obtained (Fig. 2.25). Looking at the diffraction pattern of the specimen, the direct beam is identified. Inserting an objective aperture selecting the direct beam, results in an image only containing electrons that has not been diffracted. This type of imaging is called bright-field (BF) imaging. BF images of crystalline materials gives diffraction contrast where regions of the specimen that diffract a large part of the beam appear darker than regions where diffraction is not as probable. Alternatively, a diffracted beam can be selected by the objective aperture, and is called dark-field (DF). It has a stronger contrast than BF, but as most electrons do not scatter in thin specimen and there are several diffracted beams, the DF signal is weaker than the BF signal. DF is not further used in the present work.

In BF-TEM mode, an additional diffraction contrast can arise due to variation in the specimen thickness and to bending of the lattice. Assuming a perfect crystalline and evenly thick sample, but the lattice is bent, not all regions of the specimen fulfill the same diffraction condition. Such bending contrast appears as broad and fuzzy dark lines in the BF image. Areas on the sample which are perfectly on-zone will diffract more electrons, while in the bent regions, more electrons will go through to the direct beam. If the lattice is constant and thickness varies, the diffraction contrast is depicted as sharper light and dark lines, which is a thickness contrast. Further, a local change in the lattice parameter, for example due to strain around defect, gives image contrast.

Selected area diffraction pattern

As mentioned, there exists an intermediate DP in the BFP of the objective lens. By focusing the intermediate lens on the BFP instead of the image plane of the objective lens, the DP is projected onto the viewing screen. In order to select the area in the sample which contributes to the DP, a selected area aperture is inserted in the image plane of the objective lens. In this mode there is no

objective aperture, and is called selected area diffraction pattern (SADP) (Fig. 2.25).

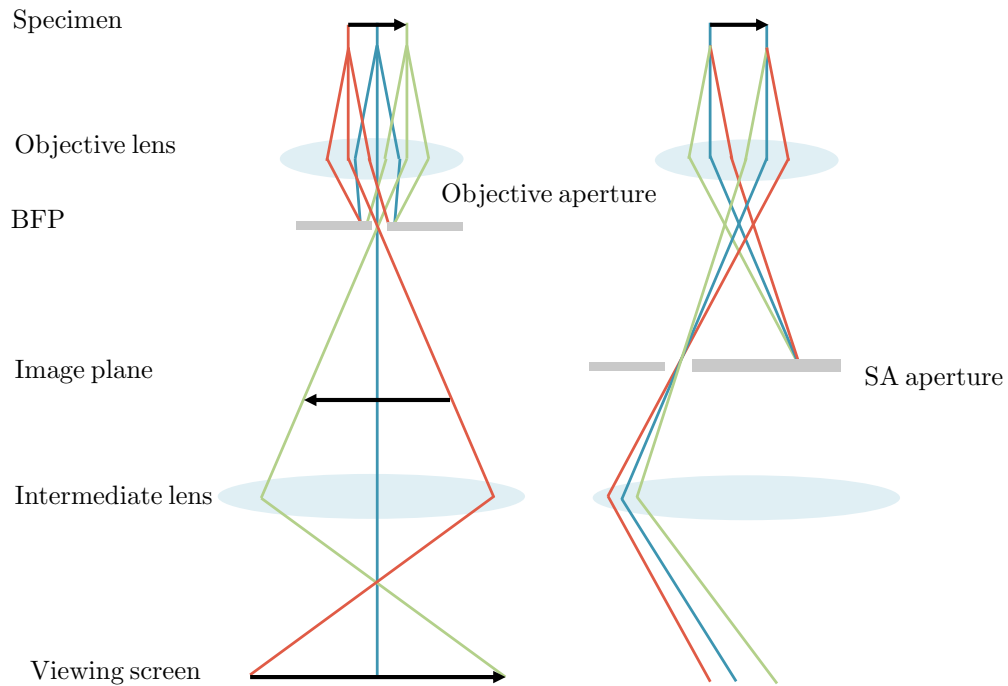


Figure 2.25: Schematic illustration of the relevant modes in a simple TEM setup indicating the most common components below the specimen. (left) BF mode with objective aperture inserted and beams are color coded after their exiting location on the specimen. (right) SADP mode with selected area aperture inserted and beams are color coded after their diffracted angle after exiting the specimen. Adapted from [40].

2.4.3 Scanning transmission Electron Microscope

In STEM, the sample is imaged using the transmitted electrons, but the beam is focused to a point scanning over the sample as in a SEM (see sec. 2.4.1), instead of being parallel to the surface for simultaneous illumination of the selected area. Instead of using apertures to select which beam will contribute to the image (incident or diffracted), this selection is done by the detector placement. The incident beam will go straight through the sample and is collected with a circular BF detector placed on the OA. This approach can be incorporated in a SEM set-up, although as the HT is lower, much thinner specimens are required (<100 nm) to have transmitted electron signal. The intensity of the incident beam is recorded for each pixel which will vary with the crystal structure at that specific point on the sample. The diffracted beam on the other hand is collected with an annular DF (ADF) detector which surrounds the BF detector (see Fig. 2.26) depending on the camera length (distance from detector to specimen), different diffracted beams are selected. A high angle ADF (HAADF) detector collects incoherently scattered electrons at high angles. For

elements with a higher atomic number, Z , the higher electrostatic interactions between the nucleus and the electron beam cause more electrons to be scattered and collected by a HAADF detector. Therefore HAADF STEM can be used for Z -contrast images. Additionally, a thick specimen will also scatter more electrons to be detected by the HAADF detector, which means that a thickness profile can be constructed for a fixed average Z .

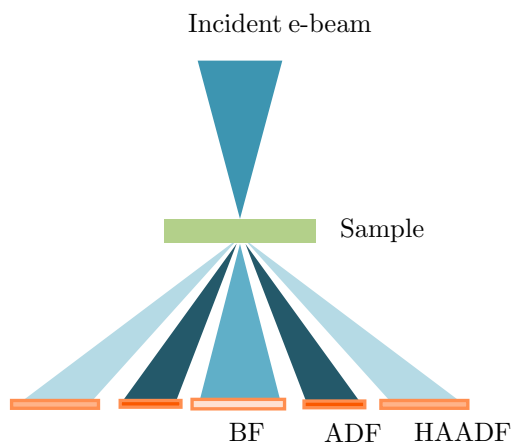


Figure 2.26: Schematic of STEM setup with HAADF detector for Z -contrast, in addition to conventional ADF and BF detectors.

3 | Experimental

Here, the experimental procedures used in this work is presented. First, the material samples used is presented, followed by an overview of the instruments and EDS detectors. Lastly, the different measurement series for EDS data collection an the following data processing is presented.

3.1 Material and specimen

In this study, three specimens were used for the purpose of improving quantitative EDS analysis. A standard NiO test specimen was used for detector and EDS setup characterization and GaAs based heterostructured NWs were used to investigate the performance of quantitative EDS analysis using Cliff Lorimer and Internal Composition Determination. Below is a detailed description of all samples.

3.1.1 NiO thin film on Mo grid

The standard test specimen used for detector characterization is supplied by Ted Pella Inc. [33]. This is a NiO thin film with a reported nominal thickness $t = 65$ nm deposited onto an amorphous carbon film of thickness $t \approx 25$ nm, supported by a 200-mesh molybdenum TEM grid of thickness ≈ 25 μm .

3.1.2 Axial heterostructure GaAs/GaAsSb NWs

In this project, previously grown GaAs/GaAsSb nanowires are studied. The structure of the NWs is described in Sec. 2.1.2 and more detailed information can be found in previous studies [1, 21], where this specific sample batch is named SCN45/sample D.

The NW was grown at a substrate temperature of 625 °C in a solid source MBE (Veeco GEN930). The flux of Ga, As and Sb precursor gasses were 0.7 ML/s, 2.5×10^{-6} Torr and 1×10^{-6} Torr respectively. The catalyst particle was formed in the holes of an Electron Beam Lithography (EBL)-patterned oxide mask on a Si(111) substrate by supplying a Ga flux for 45 s. Then, the NW growth was initialised by growing a GaAsSb stem (~ 100 nm) for 1 min with a Sb_2 flux of 1×10^{-7} Torr. Thereafter, a GaAs NWs segment was grown for 2 min before initializing growth of the

GaAsSb superlattices. Each SL was grown in periods where first the Ga shutter is kept closed and the As and Sb shutters open for 20 s, to then close the Sb shutter for 96 seconds. This procedure is repeated ten times for each SL. The GaAs spacers between each superlattice were grown for 3 min with the Ga and As shutters open. After growing six such SLs, the Ga catalyst droplets were solidified under As_2 flux of 1×10^{-5} Torr for 15 min. In order to passivate the surface states and prevent oxidizing, the NWs were capped with a 14 nm thick $\text{Al}_{0.3}\text{Ga}_{0.7}\text{As}$ and then a 6 nm GaAs shell.

Sample preparation for TEM inspection was done by J. Nilsen. The wires were transferred to a 50 nm thick SiN thin window TEM grid using isopropanol and a diamond scraper. One representative NW was chosen for subsequent characterization by inspection of the sample using the Jeol JEM2100F TEM. Thereafter, a TEM lamella was made from the center of the wire as indicated in Fig. 3.1 with Focused Ion Beam (FIB) using a FEI Helios Nanoab DualBeam. This resulted in TEM lamellas that are $\sim 12 \mu\text{m}$ long and $\sim 100 \text{ nm}$ thick, including the entire wire.

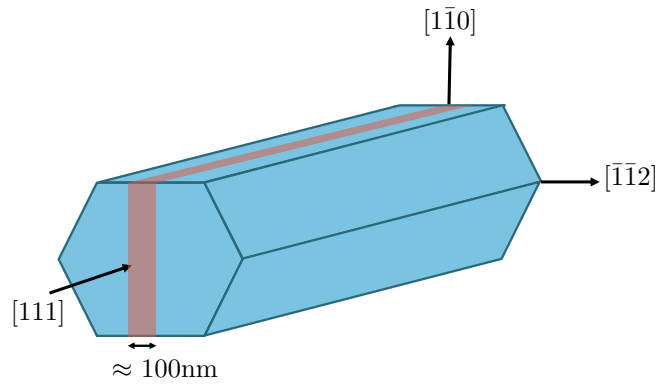


Figure 3.1: Schematic of the of the GaAsSb NW with the FIB lamella in red and relevant crystal directions indicated.

3.1.3 Radial heterostructure GaAs/AlGaAs NWs

The third sample provided for this are cross-section samples of previously grown and prepared GaAs/AlGaAs core-shell NWs. The wires were grown on a Si(111) substrate using Ga-assisted VLS growth in MBE. The core was grown for 35 min at 620°C . Subsequently the Ga flux was terminated to initiate catalyst consumption and consequently AlGaAs shell growth. Shell growth was carried out for 30 min at 460°C . TEM sample preparation was done by ultramicrotomy, where the NWs are embedded into epoxy resin and microtoming slices of the wires perpendicular to their growth direction (see Fig. 3.2). A more detailed overview of the wire growth parameters and TEM preparation is found in [41, 42].

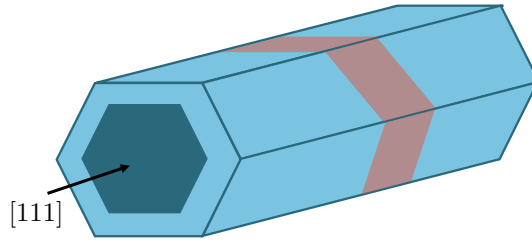


Figure 3.2: Schematic of the of the core-shell GaAs/AlGaAs NW with the cross-section sample indicated in red.

3.2 Microscopes and detectors

In this work, three different TEM and SEM set-ups were used. The first instrument, which is the main instrument used for quantitative EDS analysis, is the low voltage range Hitachi SU9000 S(T)EM, which will be referred to as SU9000 for the remainder of the report. The SU9000 has a Cold Field Emitter electron gun with a maximum emission current of 20 μm and in-lens objective lens setup. The instrument is equipped with both DF and BF detectors, as well as BSE and SE detectors. During this work, the SU9000 has been used at varying working voltages ranging between 2-30 kV using the S(T)EM holder.

The other two instruments used is the HT TEMs Jeol JEM2100 and Jeol JEM2100F, which will be referred to as the 2100 and the 2100F for the remainder of the report. The 2100 has a LaB₆ filament and a Gatan 2k Orius CCD camera. The instrument is also equipped with BF and HAADP detectors for scanning mode. All test specimens were analysed using the Jeol EM-31640 a double tilt beryllium holder and an acceleration voltage of 200 kV in this microscope. Data acquisition in this instrument was done in collaboration with Professor A. T. J. van Helvoort. The 2100F has a Schottky field emission gun (FEG) and a bottom mounted Gatan 2k UltraScan CCD camera. In this instrument, the the Jeol EM-3460 double tilt beryllium holder was used at 200 kV for all measurements. The 2100F is only used for detector characterization to see the effects of moving the EDS detector to a new instrument, and is not used for the quantitative EDS analysis of GaAs NWs. All data from the 2100F presented in this report was acquired by Professor A. T. J. van Helvoort.

These microscopes are equipped with two different Oxford EDS detectors. The detector in the SU9000 is the Oxford Ultim Extreme 120 mm² SDD detector, and the detector in the 2100 is the Oxford X-max 80 SDD detector. During the course of this work, the X-max 80 detector was moved from the 2100 to the 2100F. Both detectors are operated using Aztec software provided by

Oxford Instruments NanoAnalysis. Details of the detectors stated by the manufacturer is seen in Tab. 3.1.

Table 3.1: Details provided by the detector manufacturer for each detector used in this work.

	Ultim Extreme 100 mm2	X-max 80 SDD
Instrument	SU9000	2100, 2100F
Protection window	Windowless	Ultra thin
Solid angle [sr]	0.35	0.23
Energy resolution [eV]	130	130
Energy scale [eV]	10	10

3.3 Measurement series

3.3.1 EDS detector characterization

The test specimen was first investigated using 2100 and SU9000. Then EDS spectra were recorded in the middle of a grid square for subsequent calculation of the detector parameters. Several measurements series were carried out in order to find optimal EDS setup for subsequent quantitative EDS analysis by calculating all detector features in Tab. 2.3. A table over all relevant experimental details can be seen in Tab. 3.2. Each series was carried out with a purpose to determine the effect of varying one system parameter. If not stated otherwise, the process time setting is 4, V_{acc} is 30 in SU9000 and 200 kV in 2100 and 2100F, the data type is PointID with 120 s live time and the x-tilt is 0°.

Table 3.2: Table over the measurement series done for detector characterization. For each series, the parameter under investigation and the purpose for the specific measurement series is listed.

Varying parameter	Purpose
Instrument: SU9000, 2100, 2100F	Compare spectra and identify stray radiation
Detector: Ultim Extreme, X-max 80	Calculate general detector characteristics
Data type: PointID, map	Compare PointID and map datatype
V_{acc}: 30, 15, 10,5	Inspect effect of varying voltage
Tilt: -10° - +20°	Identify shadowing angle

3.3.2 Quantitative EDS of III-V heterostructures

The two GaAs based heterostructure samples was first investigated using both 2100 and SU9000. The first sample used for quantitative analysis was the axial GaAs/GaAsSb heterostructured NWs. This sample was studied in both the SU9000 and the 2100. In 2100, the map was taken of the top of SL3 and bottom of SL4 with Spacer 3 in between. During transfer between the 2100 and SU9000, a large dust particle had deposited onto this particular area of the wire. Therefore, the EDS maps in SU9000 were acquired at the top of the wire containing the top of SL6 and Spacer 6. In total, nine maps were taken with different combination of acceleration voltage and x-tilt as seen in Tab. 3.3. The second sample studied was the radially varying core-shell GaAs/AlGaAs NWs. These were studied at two different acceleration voltages in the SU9000 as seen in Tab. 3.3, and the entire cross section was mapped.

Table 3.3: Overview of the data series for quantitative EDS of heterostructured GaAs based NWs. The mapped area is listed for both samples studied (axial GaAsSb and radial AlGaAs NWs), in addition to the instrument used for analysis and the relevant instrument settings, namely the x-tilt and the acceleration voltage, V_{acc}

x-tilt [deg]	V_{acc} [kV]	Instrument	Area
GaAsSb			
0	30	SU9000	SL6
8	200	2100	SL4/3
	30	SU9000	SL6
	15	SU9000	SL6
	10	SU9000	SL6
20	30	SU9000	SL6
	15	SU9000	SL6
	10	SU9000	SL6
	5	SU9000	SL6
AlGaAs			
20	30	SU9000	Core and shell
	5	SU9000	Core and shell

STEM holder SU9000

In the SU9000, the STEM holder is used. A schematic illustration of the holder can be seen in Fig. 3.3. Two comments are made concerning the use of this holder for future references. First, the TEM grid for the GaAsSb (SCN45) sample falls out of the holder without further measures. The grid was secured using a Cu TEM grid spacer placed below the grid as seen in Fig (see Fig. 3.3 (b)). The spacer is made out of Cu, which is the same material as the FIB sample grid, such that no potential additional stray peaks near the relevant X-ray line are introduced to the spectra. Furthermore, the spacer was cut to not cause any additional shadowing, and should therefore have no effect on the quality of the EDS data. Secondly, the SU9000 does not have the option to tilt in the y-direction. In the remainder of this report, the y-tilt concerning the GaAsSb NWs is tilting the wires around their short axis (only possible with double tilt holder in 2100), and x-tilt is around its short axis as indicated in Fig. 3.3 (c).

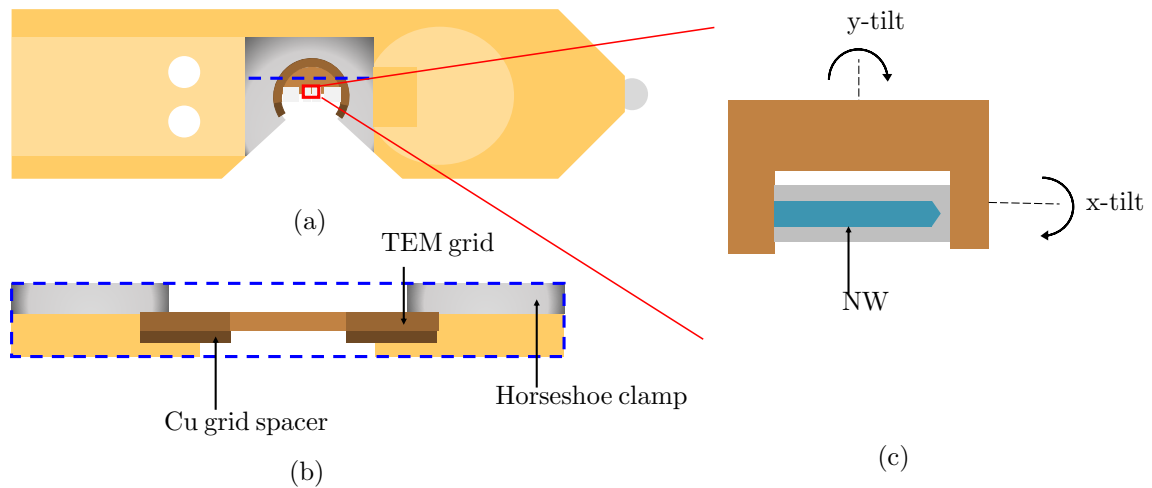


Figure 3.3: (a) Schematic illustration of a top view of the STEM holder in the SU9000 where the horseshoe clamp and the TEM grid can be seen. (b) Cross section view from the indicated blue dashed line where the Cu grid spacer is seen below the TEM grid. (c) NW position in TEM grid, with tilt axes indicated. Note that the SU9000 does not have y-tilt, but the y-tilt direction is indicated as it is the same in the 2100 relative to the NW.

3.4 Data processing

The TEM images were acquired with Digital Micrograph. This was also used to find the distance in diffraction patterns for indexing of the diffraction spots. Cropping, rotating and adding scale bars to the all SEM and TEM images were then done using ImageJ. The visual presentation of the images for the report have been done in Microsoft PowerPoint.

In this work, all EDS datasets were exported from the lab computer for further processing and analysis in the open source Python library HyperSpy [27]. A single EDS spectrum can be exported as an .emsa file and opened in HyperSpy directly. For map datasets, additional .raw, .txt and .rpl files have to be exported into the same folder containing all data files with the same name. Subsequently, the files can be converted to .hdf5 files using the script from D. Lundebjerg's master thesis [43], which also includes a tutorial on how to export the files correctly. The visual representation of EDS data such as intensity maps and spectra were extracted from .hdf5 files using HyperSpy, and then plotted using the matplotlib.pyplot library in Python.

All parameters for detector characterization presented in Tab. 2.3 was calculated using the open source Python library HyperSpy in Jupyter notebook. In this work, a notebook was developed to analyse an EDS spectrum from the standard NiO sample and can be found in Appendix A.1. The code is a generalization of the code previously written by Nylund [44]. How the code is implemented on the EDS data is also presented in Appendix A.1.

Initial inspection of the acquired EDS maps for quantification were done before analysing the spectra and maps. In some cases, the EDS maps also had to be edited before continuing with further analysis. This involved for example rotating the map 90 °, cropping the map by creating a new region of interest (ROI), changing the axes to have the same unit and binning the spectra. Furthermore, the EDS datasets were updated to have energy resolution and energy scale values found during detector characterization. A general Jupyter Notebook containing all these operations was written and can be seen in Appendix A.2.

In order to implement quantitative analysis on EDS spectra, the background has to be subtracted. Two methods for background subtraction has been applied during the data processing in this work. The first method is the integrated fitting method in HyperSpy where each characteristic peak is fitted to a Gaussian. Note that in Oxford detectors, the spectra include a zero-peak, which has to be removed prior to model fitting in order to have a decent fit for the background. Since this method forces the peaks to be ideally shaped Gaussians, the raw data can instead be used by defining two windows on each side of the peak where an average value is calculated. The background is estimated to a linear function between these average values and subtracted from the total peak intensity. The window width and position of the background windows are changed depending on the X-ray line to optimize the linear fit to the background. Quantification using Cliff-Lorimer in HyperSpy is done using the built in function. This function requires the k-factor values as input parameters, which has been extracted from the Aztec software and can be found in Appendix B.2.

The implementation of the ICD method previously outlined by J. Nilsen [15] was done using the code developed by the same author. A tutorial of the code including example data from core-shell GaAs/AlGaAs cross section can be found in [45]. For this work, the code was slightly modified to this specific material. Specifically, the reference areas, the benchmark element, X-ray lines to

be used and background windows were altered. The final script can be seen in Appendix A.3. In order to calculate the composition, the maps are summed along the axis perpendicular to the composition variations. Subsequently, the composition was calculated using both Cliff-Lorimer and ICD methods and plotted as concentration profiles.

4 | Results

In this chapter, the results are presented, and will be discussed further in the next chapter. First, the results from characterization of all EDS detection systems described in Sec. 3.2 are presented, followed by the quantitative EDS analysis of heterostructured GaAs/GaAsSb NWs. In both sections, the sample in question is first introduced based on SEM and TEM characterization before the EDS results are presented.

4.1 EDS detection system and setup

4.1.1 Preliminary sample inspection

An overview image of a grid square in the NiO thin film on Mo grid sample for detector characterization is seen in Fig. 4.1a. The results from inspection of the NiO thin film on C-support in the middle of such grid square in three different instruments are shown in Fig. 4.1 (b-f). Note that the images are not from the exact same position on the film. SADP confirms the cubic NaCl polycrystalline structure. SE imaging in SU9000 at low acceleration voltage (2 kV) provide no topography contrast as seen in Fig. 4.1c. However, as seen in Fig. 4.1d, what appears to be a topography contrast is observed as 30 kV. BF image of the film acquired in the 2100 (Fig. 4.1e) shows diffraction contrast due to the polycrystalline grain structure with average grain size ≈ 10 nm. Since the sample has constant stoichiometry, the observed contrast in the HAADF S(T)EM image acquired in the 2100F seen in Fig. 4.1f is not a Z-contrast, and will be commented on in Sec. 5.1.1. In summary, preliminary imaging of the sample indicate an average randomly oriented sample.

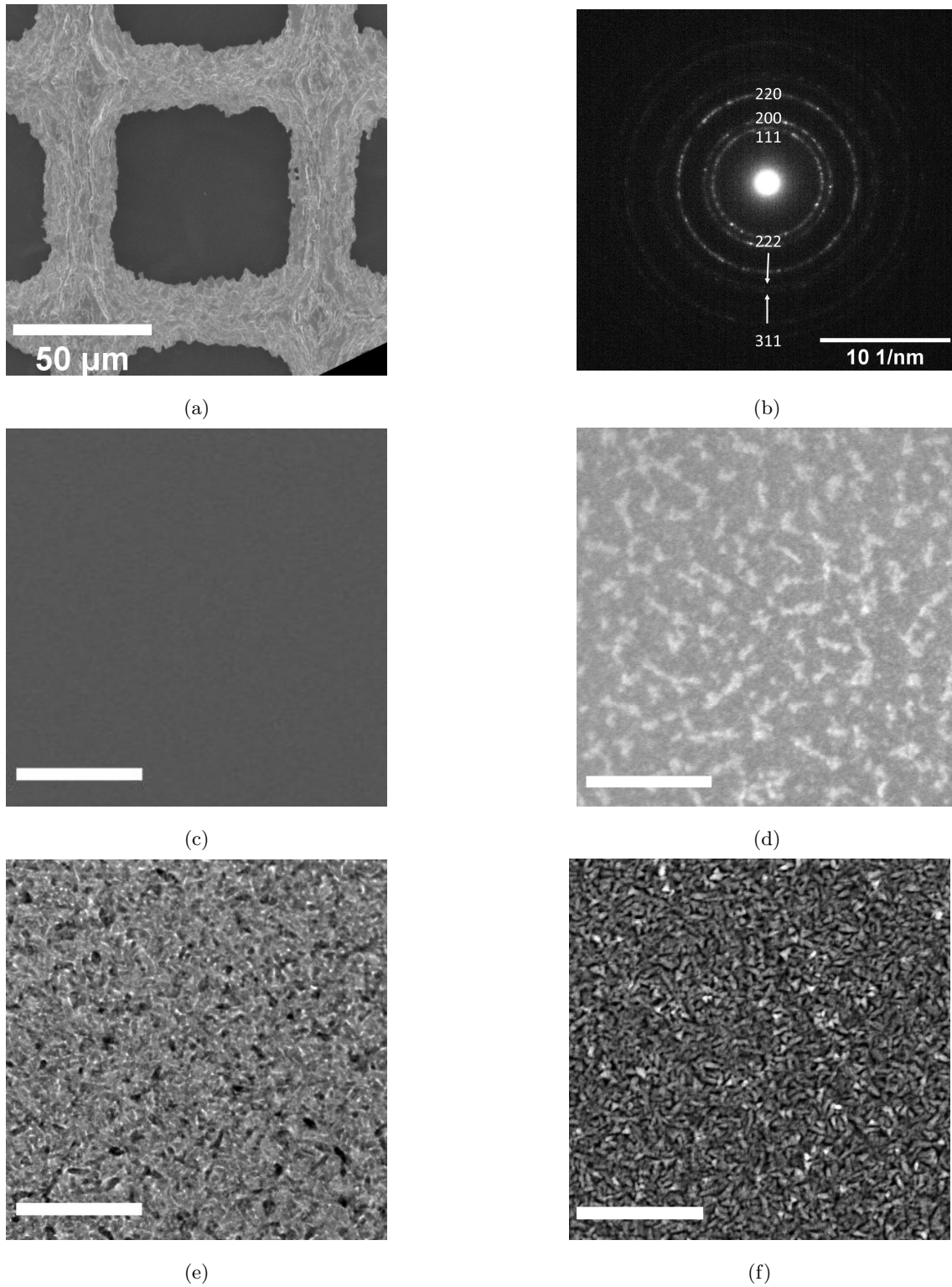


Figure 4.1: (a) SE overview image of one grid square on the test sample taken in the SU9000. (b) SADP showing the film is polycrystalline. (c) SE image of the NiO film at 2 kV and (d) 30 kV from the SU9000. (e) BF TEM image taken in 2100 and (f) HAADF STEM image taken in 2100F. Scale bars (c-f) are 100 nm.

4.1.2 EDS characterization

Here, all EDS measurements acquired from the NiO sample is presented. First, the recorded EDS spectra from all characterized instruments, namely the SU9000, 2100 and 2100F is presented. Then, the calculated EDS detection system and setup features are presented. Note that the detector in the 2100 and 2100F is the exact same detector, and the measurements are before and after the detector was moved from the 2100 to the 2100F.

EDS spectra

EDS spectra acquired in all three instruments is compared in Fig. 4.2, and is used to identify the types of stray radiation and artifacts in the different EDS systems. Ni, O, Mo and C is detected in all instruments, which is expected from the sample. The Mo X-rays are caused by stray radiation since it is from the grid, i.e. not within the illuminated area. Additionally, the $\text{Mo}_{K\alpha}$ peak is observed lower in the SU9000 at 30 kV compared to the TEMs at 200 kV.

All three instruments share common strays and artifacts, which are Fe and Si. Fe is expected stray from the column and Si signals are usually caused by internal fluorescence in the SDD detectors. Note that the peak at 0 keV in all spectra is the zero-peak, which is present in all spectra from Oxford detectors, and should be ignored.

The mentioned peaks are observed in all instruments, but there is a distinct difference in stray peaks between the 2100s and the SU9000, especially, in the low voltage range (see inset in Fig. 4.2). As can be seen, additional Al and Au X-rays are detected in the SU9000. There is also indication of F and Cu presence within the column. In Fig. 4.3 these strays are investigated further with 0° spectra at decreasing acceleration voltage. As can clearly be seen, the strays in the low voltage range, i.e. the $\text{Al}_{K\alpha}$ and $\text{AuM}\alpha$, become less prominent in the spectra with decreasing voltage.

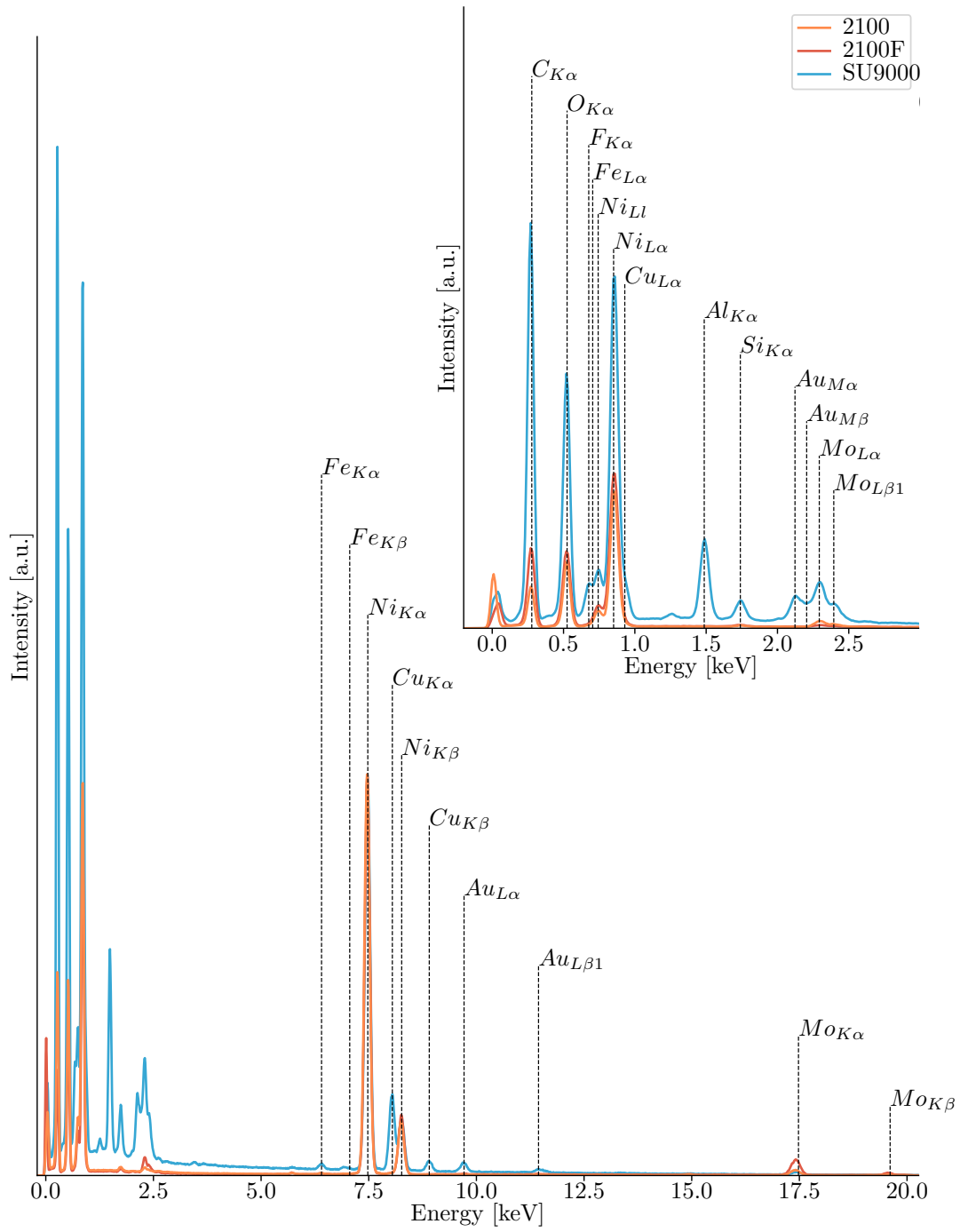


Figure 4.2: EDS spectra from all three characterized instrument setups with relevant X-ray lines indicated and normalized to the $Ni_{K\alpha}$ peak. All spectra were acquired at 0° , at voltages 200 kV in 2100 and 2100F, and 30 kV in SU9000. The inset is a magnification of the low photon energy range for better visualization.

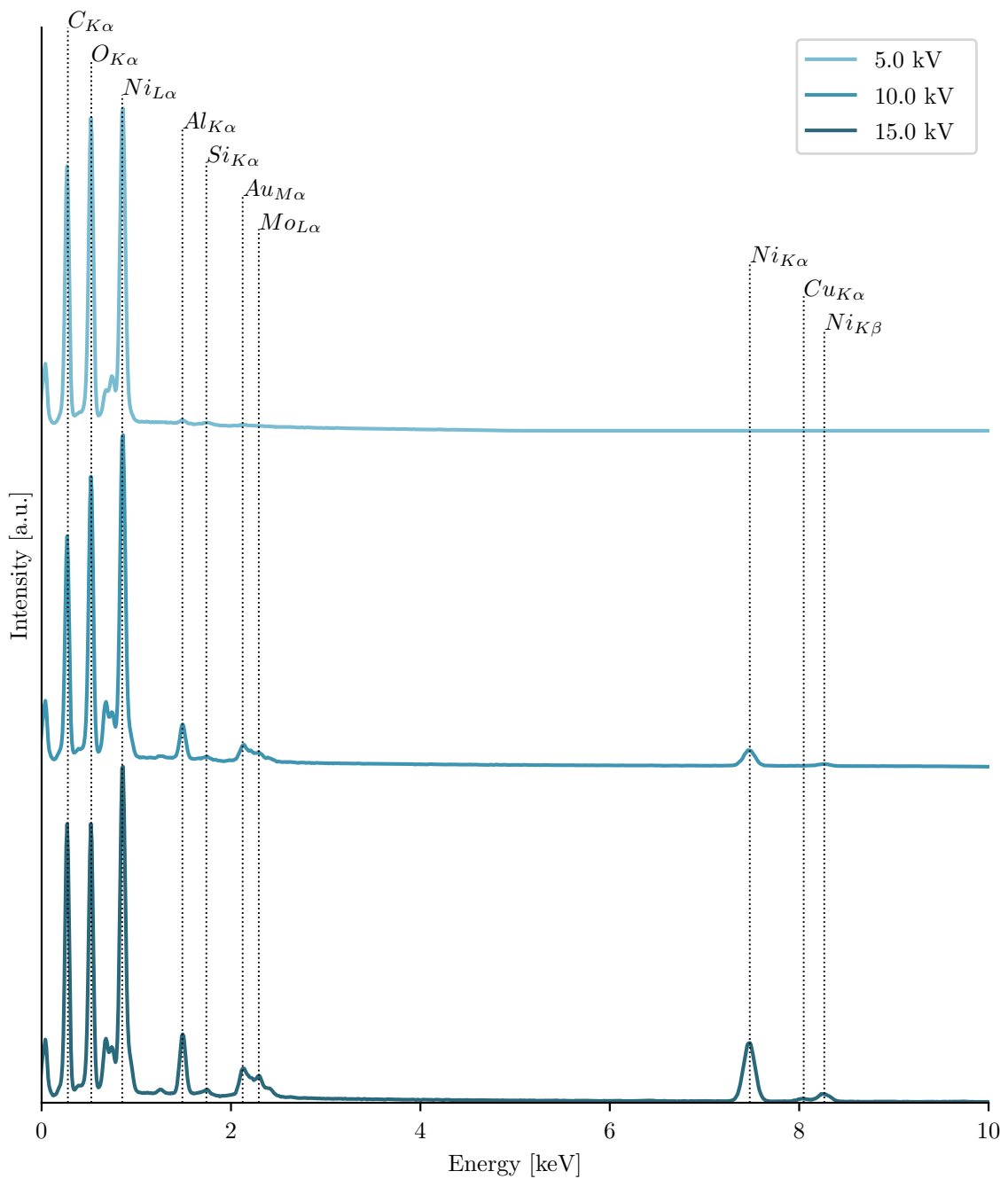


Figure 4.3: EDS spectra from SU9000 at decreasing voltage 15 kV, 10 kV and 5 kV, all taken at 0° . Relevant peaks are indicated. Al, Au, Si, Mo and Cu detection is caused by stray radiation and artifacts, as only C, Ni, and O is within the illuminated area during EDS acquisition.

EDS detection characteristics and ratios

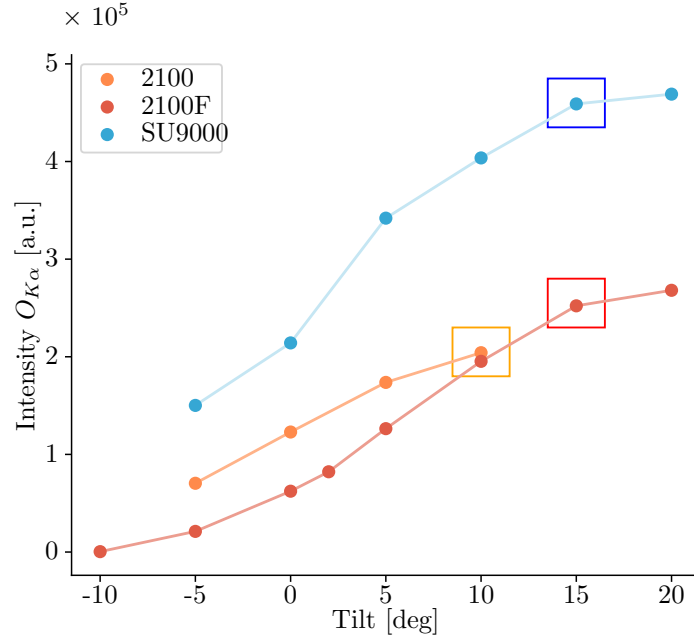
Calculated characteristics for all EDS detection systems based on 0° spectra are shown in Tab. 4.1. As can be seen, the features are calculated in SU9000 at different acceleration voltages, and also for map data. The values for map and PointID at 30 kV are very similar. In the remainder of this section, PointID is used in characterising the set-up. As can be seen, the $\text{Ni}_{K\alpha}$ to $\text{Mo}_{K\alpha}$ ratio is not calculated for 15 and 10 kV since these voltages are too low to generate $\text{Mo}_{K\alpha}$ X-rays with energy 17.5 keV. The same is true for the $\text{Mo}_{K\alpha}$ to $\text{Mo}_{L\alpha}$ ratio. Note that the channel size values at 15 kV and 10 kV are marked with "*" to indicate that these values were calculated using only the position of the $\text{O}_{K\alpha}$ peak and $\text{Ni}_{K\alpha}$ peak for the same reason.

As can be seen in Tab. 4.1, detector specific features such as energy resolution, peak shape and channel size are in principle similar before and after moving the detector from 2100 to 2100F. The $\text{Ni}_{K\alpha}$ to $\text{Mo}_{K\alpha}$ ratio on the other hand has decreased significantly after moving. Detector specific parameters in the SU9000 also remain relatively constant at decreasing voltage. The peak to background ratio, $\frac{I(\text{NiKa})}{B(\text{NiKa})}$, on the other hand decrease drastically. Additionally, this ratio is significantly lower in the SU9000 than in the TEMs.

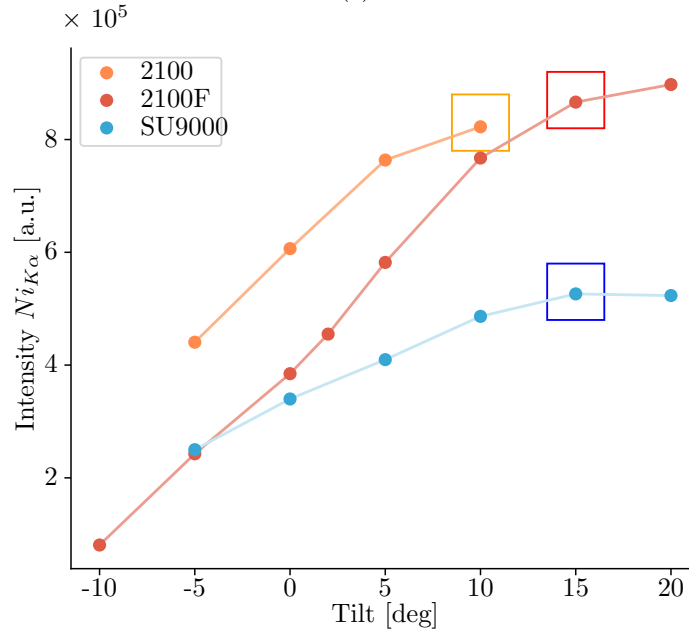
Table 4.1: Calculated values for the features of interest for all instruments at different acceleration voltages, V_{acc} . Channel sizes marked with "*" are calculated using only $\text{Ni}_{K\alpha}$ and $\text{O}_{K\alpha}$.

	SU9000				2100	2100F
Acceleration voltage [kV]	30	30	15	10	200	200
Data type	Map	PointID	PointID	PointID	PointID	PointID
Energy resolution [keV]	0.1319	0.1313	0.1330	0.1334	0.1335	0.1311
Peak shape	1.86	1.87	1.91	2.04	1.84	1.84
Channel size [eV]	10.01	10.03	10.00*	10.02*	10.03	10.04
$\frac{I(\text{NiKa})}{I(\text{MoKa})}$	93	95	-	-	53	18
$\frac{I(\text{MoKa})}{I(\text{MoLa})}$	0.07	0.07	-	-	2.20	2.1
$\frac{I(\text{NiKa})}{B(\text{NiKa})}$	891	889	714	204	4341	4009

The angle at which shadowing occurs is assessed in all three instruments by plotting the intensity of the $O_{K\alpha}$ peak (see Fig. 4.4a) and the $Ni_{K\alpha}$ peak (see Fig. 4.4b). In SU9000 and 2100F a substantial decrease in intensity for both peaks occur around 15° . From the data-points available from the 2100, it is plausible to assume shadowing occurred at 10° . It is obvious that the intensity, i.e. the output count rate has decreased after the detector was moved, and that the shadowing angle has increased.



(a)



(b)

Figure 4.4: Intensity of the (a) $O_{K\alpha}$ peak and (b) $Ni_{K\alpha}$ peak in all three instruments. Tilt angle where substantial decrease in peak intensity occurs is indicated with square boxes. The bold dots are the data points for each tilt angle.

Based on these results, positive tilt angles is used in subsequent quantitative analysis of GaAs based NWs to improve count statistics. The maps are also re-calibrated with the correct energy channel dispersion and energy resolution for each detector based on the 30 kV measurements from the SU9000.

Cliff-Lorimer quantification

EDS quantification of the sample was done with Cliff-Lorimer at 200 kV in the 2100 and 30kV, 15 kV, 10 kV and 5 kV in the SU9000. The results can be seen in Tab. 4.2. From the known stoichiometry of the sample, the expected concentrations are 50 at.% Ni and 50 at.% O. At 200 kV and 30 kV, the calculated values are within ± 7 at.% of the expected values, and within ± 20 at.% at 5 kV.

Table 4.2: Quantification results of NiO thin film using Cliff Lorimer at five different acceleration voltages from 2100 (200 kV) and SU900 (30-5 kV). The $\text{Ni}_{K\alpha}$ line was used at 200 keV, 30 keV and 15 keV in , and the $\text{Ni}_{L\alpha}$ line was used at 10 keV and 5 keV.

V_{acc}	200 kV	30 kV	15 kV	10 kV	5 kV
Ni [at.%]	43.3	48.4	37.5	29.6	29.4
O [at%]	56.7	51.6	62.5	70.4	70.6

4.2 Heterostructure GaAs/GaAsSb NWs

Here, the results from both preliminary SEM and TEM characterization and quantitative EDS using ICD and Cliff-Lorimer of the GaAsSb heterostructured NW is presented.

4.2.1 Preliminary sample inspection

Prior to EDS mapping, general TEM and SEM characterization of the sample was performed. An overview SE image of the entire FIB sample containing all protection layers from the preparation and the NW in the middle is seen in Fig. 4.5a. The top of the NW is identified by the triangular shape on one end. Additionally, FIB markers made during the sample preparation is also indicated, which proved useful to image the same regions in different instruments. The different protection layers were identified using EDS as seen in Fig. 4.5b as it might influence the subsequent EDS mapping of the wire. As can be seen, the wire is lying on a SiN thin film support. The top protection layer is made from Pt. Additionally, a large amount of Ga is detected within the entire mapping area since Ga ions was used during the FIB preparation.

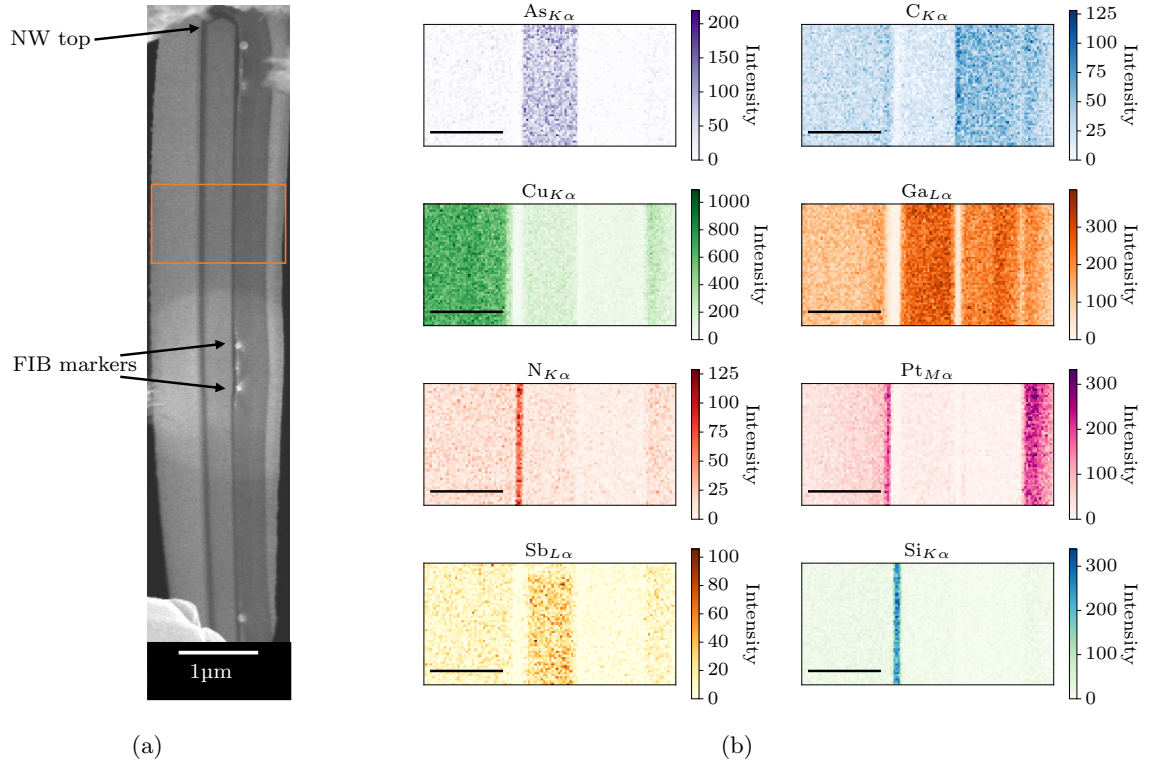
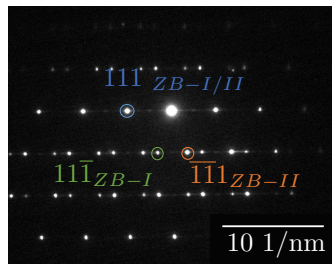
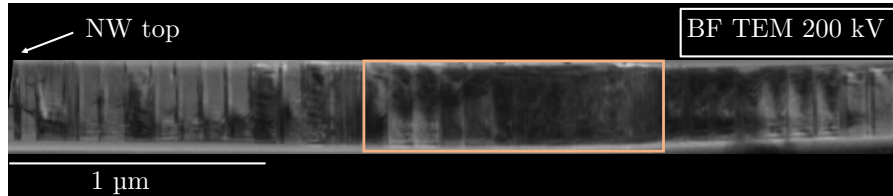


Figure 4.5: (a) SE overview image of the GaAsSb NW cross section sample with NW top indicated as well as FIB markers helpful for locating areas on the wire. (b) EDS map of the different protection layers deposited during FIB sample preparation from the indicated orange area in the SE image. All scale bars are 500 nm.

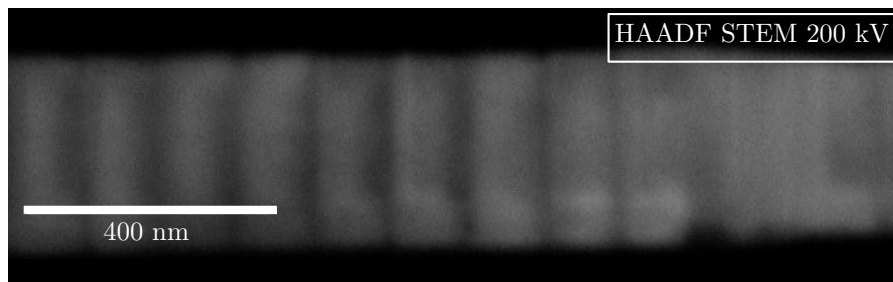
Images of the NW sample done in both HT TEM and LV SEM is shown in Fig. 4.6, where SL4 is magnified and observed with different imaging contrasts. The NW is $\approx 8.5 \mu\text{m}$ long with increasing width from 310 nm at the bottom to 380 nm at the top. From BF TEM image in Fig. 4.6b, bending contrast is observed throughout the wire. Identification of the GaAsSb insets is desirable for the purpose of this project, which is obtainable through atomic number contrast using both HAADF STEM in HT 2100 (see Fig. 4.6c) and BSE SEM in LV SU9000 (see Fig. 4.6d). As can be seen, the contrast is significantly more apparent using HAADF STEM, and based in this, the size of the GaAsSb insets is measured to be $l_w \approx 120 \text{ nm}$. The SADP in fig. 4.6a is on $[\bar{1}10]$ zone and taken at 7° x-tilt and 14° y-tilt. The SADP from the middle of Spacer 3 shows twinning of two ZB phases and $[111]$ growth direction.



(a)



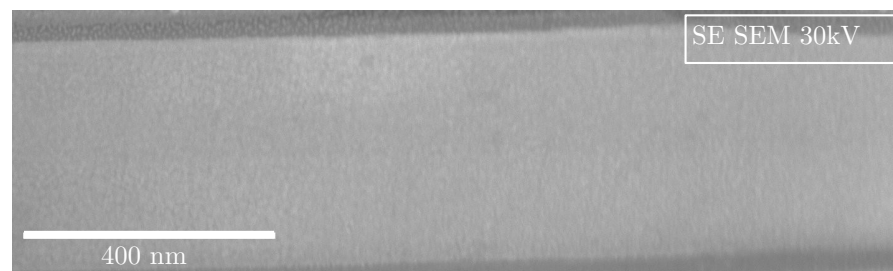
(b)



(c)



(d)



(e)

Figure 4.6: (a) SADP showing ZB crystal structure with $[111]$ growth direction and twinning of two ZB phases. (b) BF TEM overview of the wire at 200 kV from 2100. Spacer 3 and SL4 in indicated area is magnified and imaged using different contrasts. Z contrast in (c) HAADF STEM image at 200 kV from the 2100 and (d) BSE image at 30 kV from SU9000 and topography contrast in (e) SE image at 10 kV in SU9000.

4.2.2 Quantitative EDS analysis

An overview image of the entire GaAsSb NW is seen in Fig. 4.7a. The tilt axis is indicated, as well as the placement of the detector relative to the wire. X-ray intensity map of the top of the wire used for ICD and C-L quantification taken in SU9000 can be seen in Fig. 4.7b. This is the top of SL6, and the reference area during ICD analysis was set to be the first 200 nm of each map. Fig.4.6e is taken in 2100 and is of the top of SL3 and bottom of SL4. In this map, Spacer 3 is used as the reference area for ICD analysis.

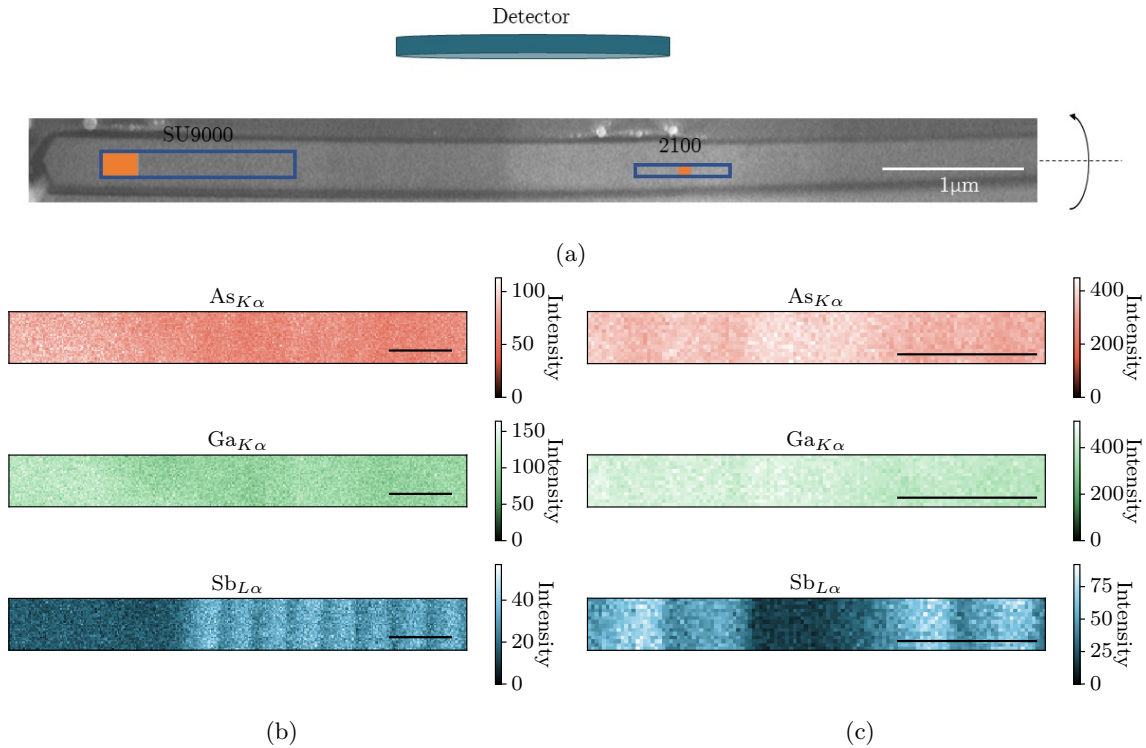


Figure 4.7: (a) SE reference image from SU9000 of the entire NW where map areas are indicated with reference area for ICD analysis is indicated in orange, as well as tilt axis. Intensity map of the indicated areas including $As_{K\alpha}$, $Ga_{K\alpha}$ and $Sb_{L\alpha}$ peak from (b) SL6 at 30 kV and 8° x-tilt from SU9000 and (c) SL4 and 3 with spacer between at 200 kV and 8° x-tilt from 2100. Scale bars are 200 nm in EDS maps

EDS spectra of the inspected areas are plotted in Fig. 4.8, where relevant X-ray lines are indicated. As can be seen in the inset, the intensity of the $Sb_{L\alpha}$ peak decreases with decreasing voltage and at 5 kV, the peak is barely visible. The same is true for the $Ga_{K\alpha}$ and $As_{K\alpha}$ peaks. Therefore, L lines for Ga and As are used for quantification at voltages 10 and 5 kV. Note that here, the spectra at 200 kV from 2100 is of SL3-4, while the spectra at 30-5 kV from SU9000 are of SL6 due to contamination on the lamella between measurement in the instruments. It is assumed that the areas are similar for inspection of the EDS spectra.

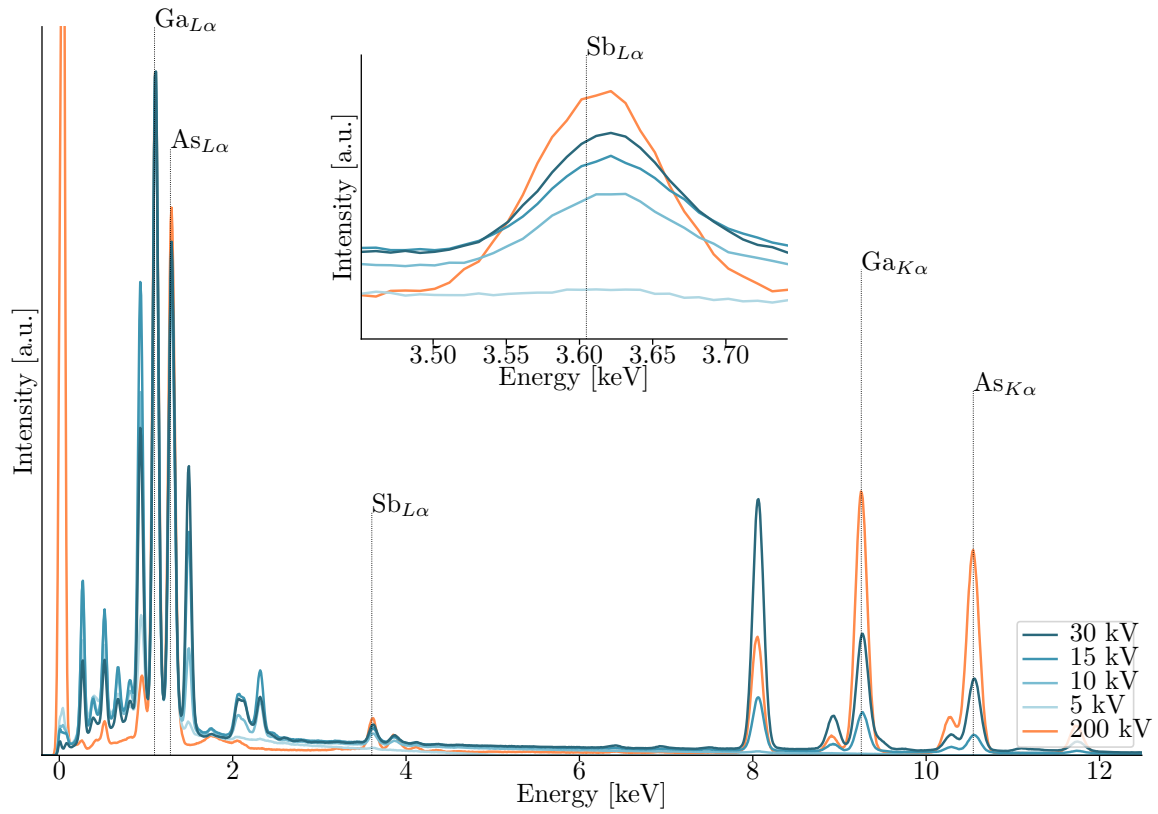


Figure 4.8: EDS spectra of the mapped regions of GaAsSb heterostructured NW. The spectra are taken at decreasing acceleration voltage, where 5-30 kV is from the SU9000 and 200 kV is from the 2100. The inset is showing the $Sb_{L\alpha}$ peak magnified to better see the effect of overvoltage on peak intensity. The spectra are normalized to the $Ga_{L\alpha}$ peak.

Concentration profiles

The results of quantitative analysis of the GaAsSb NWs from the measurement series seen in Tab. 3.3 is presented. All concentration profiles calculated using both the standard Cliff-Lorimer method and ICD at 8° x-tilt with varying acceleration voltage between 200-10 kV is seen in Fig. 4.9. Note that the concentration profile at 200 kV from 2100 is of SL3 and 4 as seen in Fig. 4.7c, while all other are of SLs seen in Fig. 4.7b. Fig. 4.10 shows concentration profiles at 20° x-tilt with acceleration voltage between 30-5 kV of SL6 from SU9000. Both Cliff-Lorimer and ICD profiles are included in light and dark colors respectively. The relative thickness profile calculated in the ICD method is also included for each measurement.

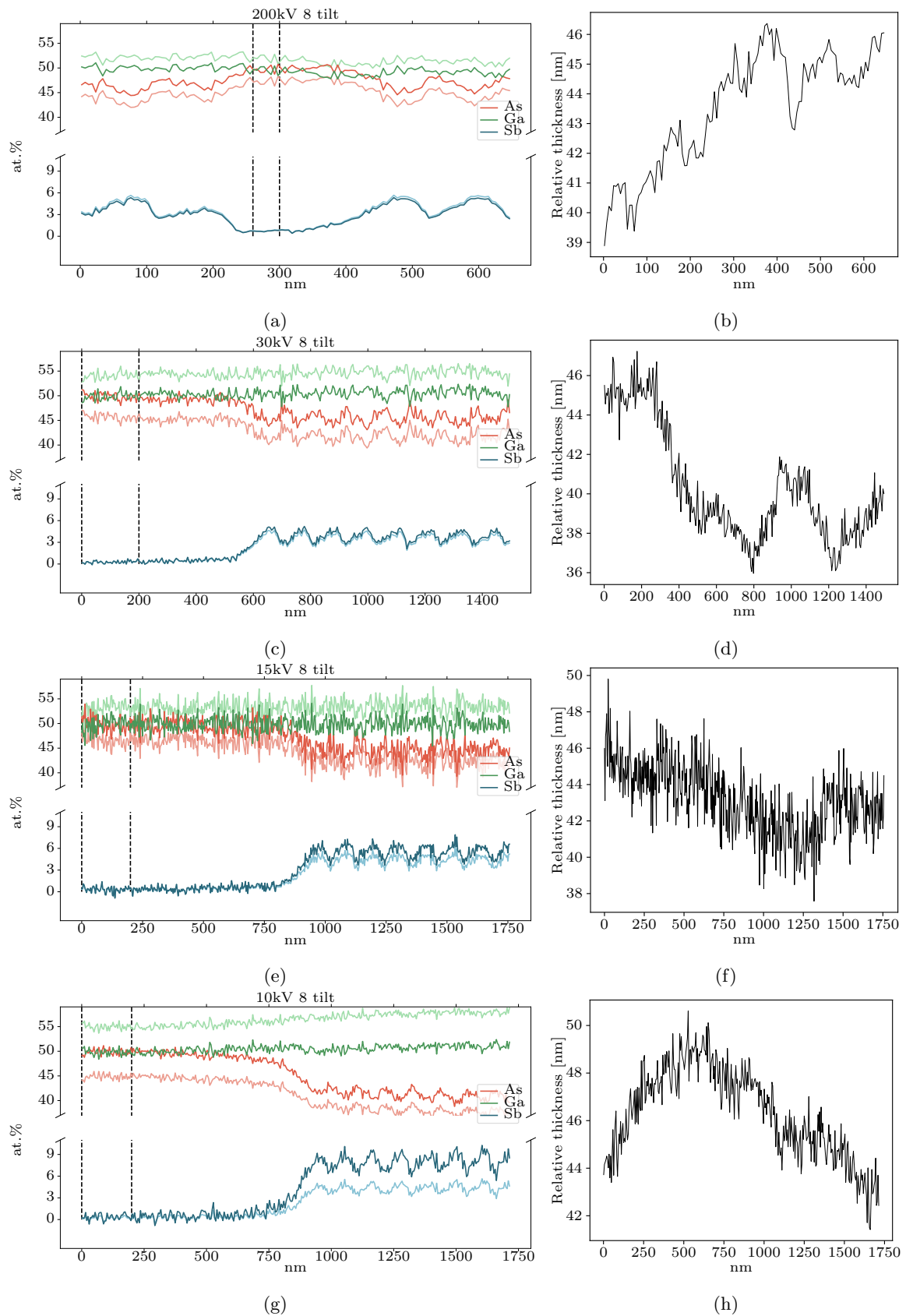


Figure 4.9: Concentration profiles of GaAsSb heterostructured NW from EDS map taken at 8° x-tilt with decreasing voltage. (a,c,e,g) Concentration profiles of As (red) Ga (green) and Sb(blue) for both ICD (dark) and Cliff-Lorimer (light). Reference area indicated by vertical dotted lines. (b,d,f,h) Relative thickness profiles calculated using ICD.

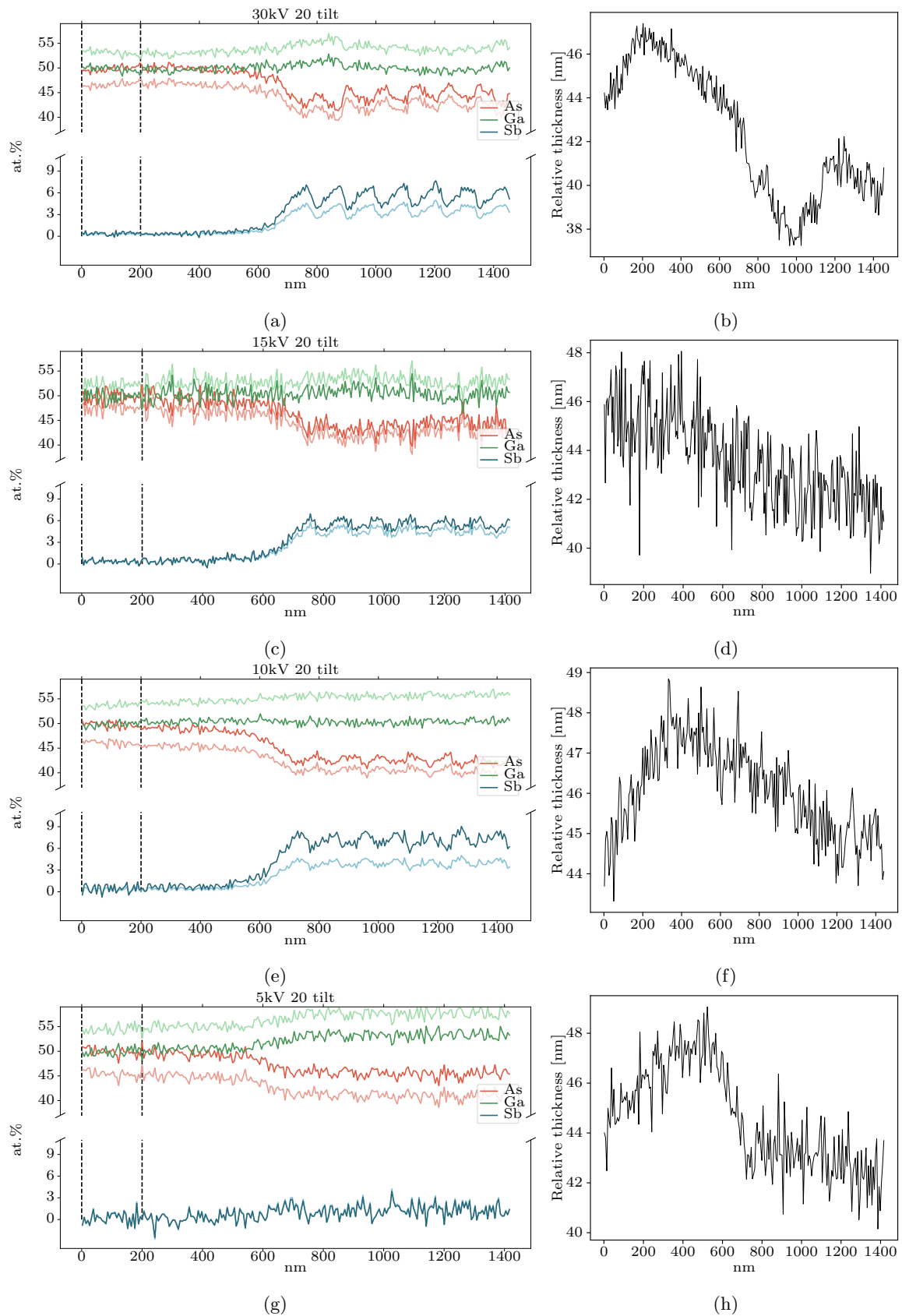


Figure 4.10: Concentration profiles of GaAsSb heterostructured NW from EDS map taken at 20° x-tilt with decreasing voltage. (a,c,e,g) Concentration profiles of As (red) Ga (green) and Sb(blue) for both ICD (dark) and Cliff-Lorimer (light). Reference area indicated by vertical dotted lines. (b,d,f,h) Relative thickness profiles calculated using ICD.

As can be seen from all profiles, the Ga concentrations are stable around 50 at.% using ICD. The As concentration is also stable around 50 at.% in the spacers using ICD. Both As and Ga concentrations using Cliff-Lorimer method follow same behaviour as ICD compositions. However, Cliff-Lorimer Ga and As concentrations are 1-5 at.% above and below the ICD concentration respectively. The Sb concentration follows a periodic increase to a maximum value within each well. It is also observed that all Sb concentration profiles deviated from each other, both using Cliff-Lorimer and ICD. Additionally, the ICD profiles are without exception higher than using Cliff-Lorimer.

In addition to the relative thickness profile, the ζ -factors for all elements and the flatness, ΔC_{Ga} , of the benchmark element Ga can be extracted during the ICD procedure, and given in Tab. 4.3. Here, the initial flatness, ΔC_{Ga}^0 , which is the flatness during the first iteration if the ICD process is included. Furthermore, for better comparison of the results, the maximum Sb concentration, C_{Sb}^{max} , in each profile is extracted for both Cliff-Lorimer and ICD. Results from a map at 30 kV and 0° tilt is also included.

Table 4.3: All relevant parameters from ICD analysis of EDS maps of GaAsSb heterostructured nanowire, including ζ -factors for all elements, maximum Sb concentration values, C_{Sb}^{max} , for both Cliff-Lorimer and ICD, as well initial and final flatness of benchmark element, ΔC_{Ga}^0 and ΔC_{Ga} respectively.

	0 tilt		8 tilt			20 tilt			
	30 kV	200 kV	30 kV	15 kV	10 kV	30 kV	15 kV	10 kV	5 kV
ζ_{As}	1641	153	782	6785	289	495	2753	162	395
ζ_{Ga}	1028	124	499	3273	217	328	1381	128	291
ζ_{Sb}	1149	176	395	1620	1258	365	637	718	2543
$C_{Sb}^{max,ICD}$ [at.%]	7.13	5.35	5.20	7.89	10.26	7.68	6.94	9.04	3.88
$C_{Sb}^{max,C-L}$ [at.%]	4.70	5.68	4.72	6.25	5.64	4.99	5.77	5.01	4.24
ΔC_{Ga} [at.%]	6.1	3.3	4.6	8.7	4.0	4.5	8.0	3.3	6.9
ΔC_{Ga}^0 [at.%]	7.2	4.6	6.0	11.9	8.3	7.1	10.3	6.5	7.9

Based on the C_{Sb}^{max} values presented in Tab. 4.3, an average value and a standard deviation can be calculated. For the ICD, the average maximum Sb concentration is (7 ± 1.6) at.%, and (5 ± 0.6) at.% with Cliff-Lorimer approach. These values are calculated excluding the results from 5 kV, seeing as the signal to noise ratio is too low (see Fig. 4.10g) due to low overvoltage (See inset in Fig. 4.8). Hence, the results show a higher variation in the ICD compositions than using Cliff-Lorimer.

4.3 Heterostructure GaAs/AlGaAs NWs

The last sample studied in this work are radially heterostructured GaAs/AlGaAs NWs. GaAs-AlAs is an important system for heterostructures where group III atoms are exchanged rather than group V. BSE image of the cross section of one representative wire can be seen in Fig. 4.11a. As can be seen in with the observed Z-contrast, the wires have a core of GaAs and a shell of the lighter AlGaAs. An EDS map can be seen in Fig. (b-d), where the relevant X-ray intensities are plotted. The maps are taken in the SU9000 at 30 kV, and as can be seen, there is a high $\text{Al}_{K\alpha}$ signal in the core where no Al is present.

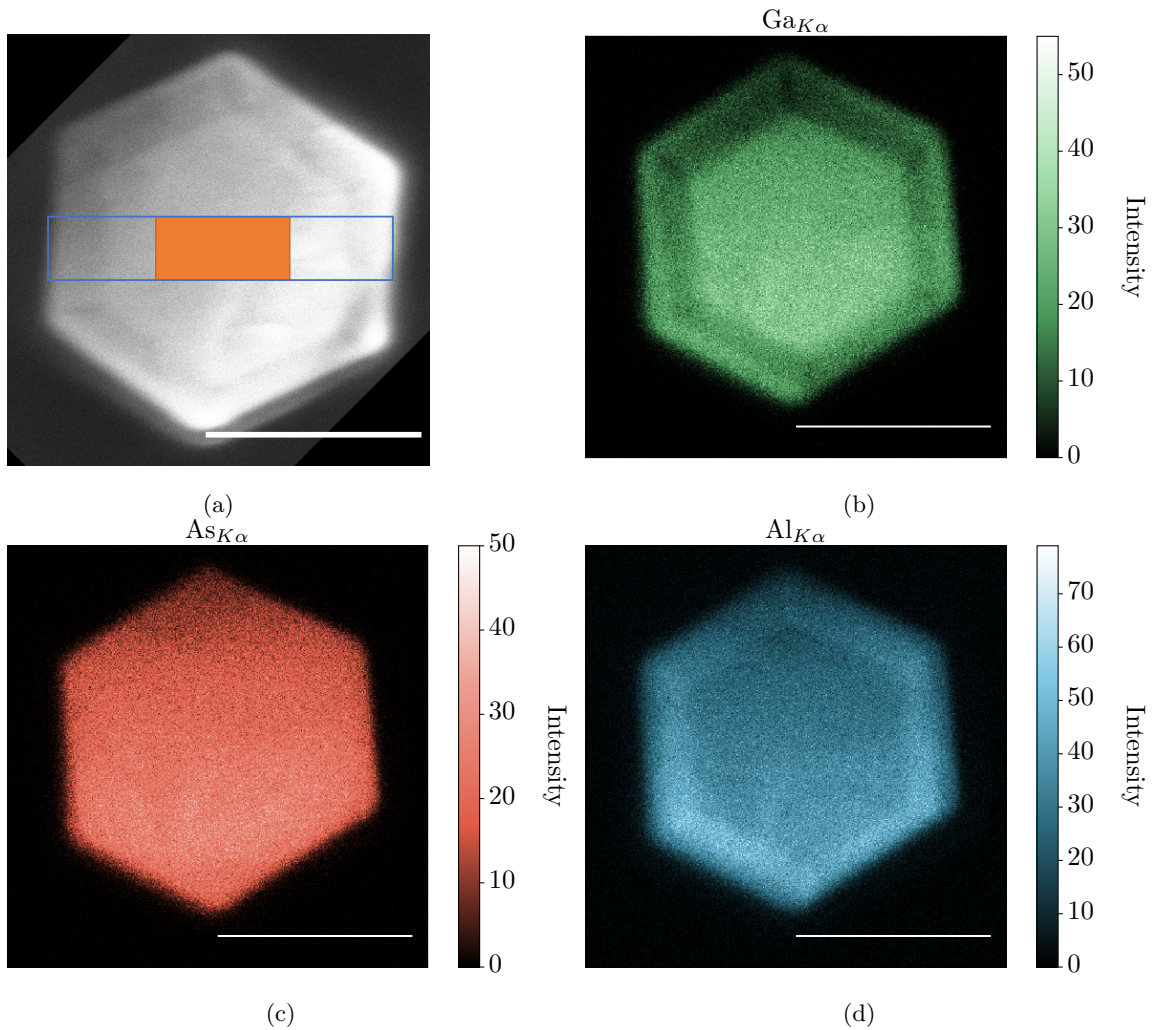


Figure 4.11: (a) BSE image of a core-shell GaAs/AlGaAs NW cross section where EDS mapping area used for subsequent quantitative analysis with indicated reference area for ICD quantification in orange. Intensity maps of the characteristic (b) $\text{Ga}_{K\alpha}$, (c) $\text{As}_{K\alpha}$ and (d) $\text{Al}_{K\alpha}$ X-ray lines. All scale bars are 100 nm.

A large amount of Al stray is present in the EDS sum spectra from the GaAs core as seen in Fig. 4.12. This is similar as observed in the GaAsSb sample (see Fig. 4.2), but there the Al is

not interfering with the peaks of interest. Further, note that the other strays as Au and Cu are present. As can be seen in the inset, the $Al_{K\alpha}$ peak is significantly reduced in the core at 5 kV compared to 30 kV.

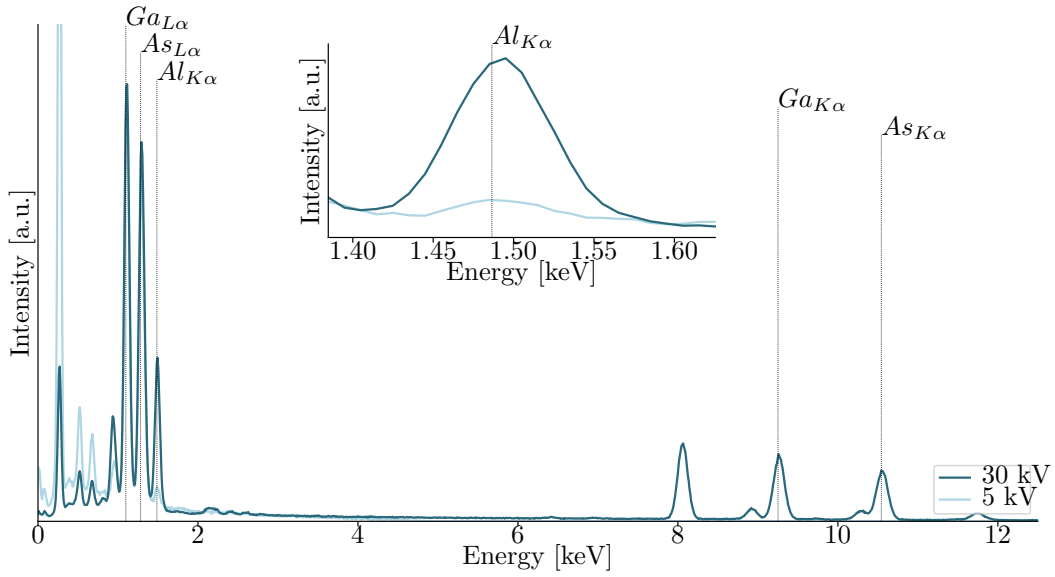


Figure 4.12: EDS spectra from the GaAs core where aluminium content is 0 at.% from the SU9000 at 30 and 5 kV.

Quantification of AlGaAs NWs using ICD and Cliff-Lorimer is shown for two different acceleration voltages below in Fig. 4.13. At 30 kV, the high $Al_{K\alpha}$ from the core results in a Al composition of 95 at.% and a Ga and As composition of 2.5 at.% in the core in ICD method. Using CL, the Al concentration is around 28 at.% in the core, with Ga and As concentrations around 36 at.%. At 5 kV, the Al concentrations in the core are closer to zero and the Ga and As concentrations are closer to 50 at. % in both models. The final flatness of the benchmark element As in the ICD method is 1.3 at.% and 7.2 at. % at 30 and 5 kV respectively.

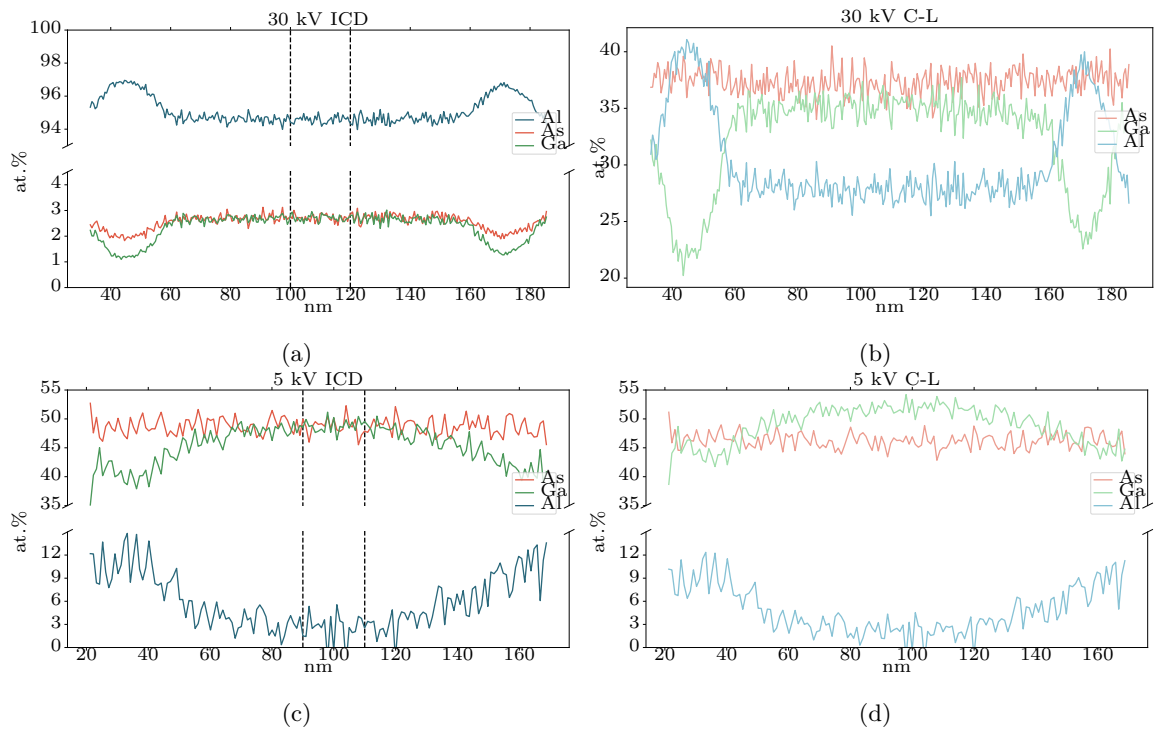


Figure 4.13: Concentration profiles from EDS acquired at in SU9000 at voltage indicated in each figure. The profiles are across a cross section of AlGaAs core-shell using both (a,c) ICD where the GaAs core is used as a reference area and (b,d) Cliff-Lorimer quantification. Area used as reference area during ICD algorithm is indicated with black vertical dashed lines.

5 | Discussion

Here, the results presented in the previous chapter are further elaborated and discussed. First, the observations concerning characterization of the EDS detection system and setup is given. Subsequently, a detailed review of the quantitative analysis of the axial GaAsSb NWs is given, focusing on the performance of the ICD method. Lastly, the results from quantification of radial AlGaAs NWs is commented on.

5.1 EDS detection system and setup

5.1.1 Preliminary sample inspection

Preliminary characterization of the NiO test specimen is required to verify the structure of the provided NiO film and determine a suitable area to record EDS spectra for subsequent calculation of EDS detector system features. During this initial inspection in transmission mode and HT STEM, identifying the orientation of the sample, i.e. which side the NiO thin film is deposited, was not straight forward. In low voltage SEM, the topography of the sample was studied at two different acceleration voltages. At 2 kV, there is no topography contrast, indicating a flat surface. However, at 30 kV, there is an apparent topography contrast. At higher acceleration voltages, the penetration depth of SE increase, which means that the contrast at 30 kV originates from further down in the sample. If the film has been placed upside down in the holder, with the NiO film facing down and the C support facing up in the instrument, it can be assumed that the topography contrast appearing at higher voltages is due to island growth on the surface of the film (see in Fig. 5.1). The orientation of the sample in the instrument may effect the recorded spectra in two ways. First, the generated X-rays have to travel through the C thin film before reaching the detector, adding to the absorption path. However, C is a light element with low mass-absorption coefficients, especially for the high energy photons such as $\text{Ni}_{K\alpha}$ and $\text{Mo}_{K\alpha}$. Therefore it is reasonable to assume absorption through the C support does not effect the calculated intensity ratios. Secondly, the amount of Mo signal detected may increase if the sample is placed upside down with the Mo grid on top. Especially in LV SEM, this could potentially increase the $\text{Mo}_{K\alpha}$ intensity and therefore the calculated feature ratios. Therefore, characterization in SEM should be done with the same sample orientation, which can be identified by using SE signal at low and high

acceleration voltages as described. In HT TEM, the incident electrons have sufficient energy to transmit through the sample, and this will likely not affect the spectra. However, surface roughness can matter, as this can lead to uneven absorption and should be avoided for quantitative EDS [39]. Therefore it is concluded that having the C support facing up gives best reproducibility.

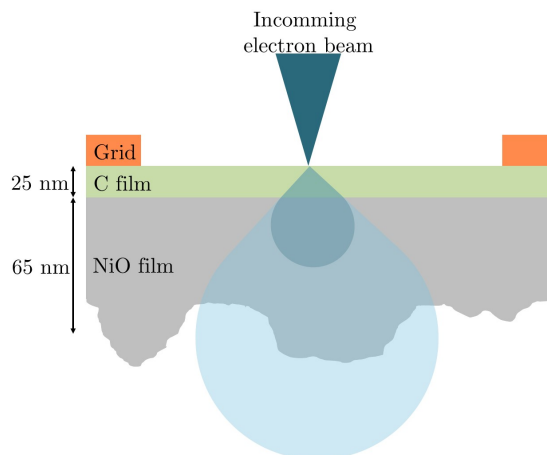


Figure 5.1: Schematic illustration of the size of the interaction volume between the incident beam and the NiO thin film placed upside down (note interaction volume not to scale). As higher acceleration voltages (light blue) the penetration depth for SE electrons increase, and island formation on the film surface is observed, while at lower voltages, the SE signal originates only from the flat bottom.

BF TEM and SADP confirms that the thin film is polycrystalline with randomly oriented grains with diameter ~ 10 nm. The diffraction rings coincide with stoichiometric NiO with cubic NaCl archetype crystal structure, confirming that no unoxidised Ni is present in the specimen. HAADF image of the NiO sample displays some contrast between the grains. Since the composition of the film is fixed, the contrast in HAADF image could be attributed to thickness variations. However, comparing the BF image to the HAADF image, the contrast variations are contained within each grain, i.e. smaller than the topography contrast variations at 30 kV SE. Therefore, it is more likely that the contrast is caused by electron channeling effects. Several studies address electron channeling effects in HAADF imaging [46–48], and the tendency for the incoming electrons to focus along the atomic columns is expected to increase the probability of high scattering angles, causing an additional contrast in the HAADF image. Nevertheless, the average orientation is sufficiently random within the analysed area, and should not effect the EDS measurements if a representative area is mapped. Generally, acquiring an EDS map of for example 100×100 nm would ensure a good average of the NiO film, while PointID could be effected by the local variations if the probe size is small enough, e.g. smaller than the grain size of ~ 10 nm. This will be commented on in Sec 5.1.2. In summary, the preliminary inspection of the NiO thin film establishes the randomly oriented polycrystalline structure as reported by the manufacturers [33], with average homogeneous area in the middle of a grid square which is to be used for the subsequent EDS analysis.

5.1.2 EDS characterization

Results from characterization of the EDS detection system and setup using the NiO sample is discussed below. First, the stray radiation identified in the EDS spectra are commented on, followed by a review of the calculated detector characteristics. Here, the main focus is to compare characterization between the instruments, i.e. HV (2100s) compared to LV (SU9000), and between the detectors, i.e. windowless with large solid angle (Ultim Extreme) and thin film window with smaller solid angle (X-Max 80). These detectors are from the same manufacturer and operated by the same software platform (Aztec). The findings from the TEMs (2100 and 2100F) is compared to previous detector characterization in these instruments by I. E. Nylund [44] from 2017. In this earlier study, the 2100 was equipped with the exact same X-Max 80 SDD detector as in this work. The 2100F was also equipped with an X-Max 80 that is currently in repair, and was therefore replaced by the X-Max originally installed on the 2100 during the course of this work. It is therefore relevant to investigate and compare the measurements before and after the detector was moved, and compare the current installation to previous measurements with the same detector version in the same instrument. Characterization of the detection system in the SU9000 is done for the first time in this work.

EDS spectra

The $\text{Ni}_{K\alpha}$, $\text{Ni}_{K\beta}$, $\text{Ni}_{L\alpha}$, $\text{O}_{K\alpha}$ and $\text{C}_{K\alpha}$ X-rays which originate from the illuminated area are observed in the EDS spectra from all three instruments (see Fig. 4.2). All other peaks in the spectrum are therefore caused by artifacts or stray radiation within the AEM column. This includes the observed Mo signal in all spectra, as this originates from the sample grid, and not from the illuminated area. The spectra from the three different instruments all have common strays and artifacts, which are Fe and Si. The $\text{Si}_{K\alpha}$ peak is commonly observed in all EDS spectra, since this is caused by internal fluorescence of the SDD. $\text{Fe}_{K\alpha}$ is present in all spectra, and $\text{Fe}_{L\alpha}$ overlaps with the Ni_{Ll} peak and is not distinguishable. Nevertheless, Fe is a common system peak originating from the microscope stage, and is generated by stray radiation in most AEMs [11]. In summary, the 2100 and 2100F has additional Fe and Si peaks that does not originate from the sample, which is the same as previously reported [44]. It is therefore established that no new significant contamination has been introduced in these instruments.

In addition to the aforementioned strays and artifacts in the spectra, the SU9000 have Cu, Au, Al and F peaks, which are not observed in the TEMs. Cu is, similar to Fe, a common stray to have present in an AEM, as many parts of the microscope stage and holder are made out of this conductive material. The $\text{F}_{K\alpha}$ peak in the low energy range is close to the Ni_{Ll} peak, but can be observed as a distinguished peak. The $\text{Al}_{K\alpha}$ and $\text{Au}_{M\alpha}$ peaks have a relatively high intensity, introducing significant stray peaks in the low energy photon range. The Au strays originate from

the holder, similar to the Al peak, which originates from the aluminium horseshoe clamp on the holder (see Fig. 3.3). Due to their high signal, these strays are very inconvenient, as they prevent both qualitative and quantitative composition determination by conventional methods of both elements. However, as can be seen in Fig. 4.8, the Al and Au peak diminish at lower voltages, which is an approach to counter the stray emission effects on this particular set-up. This indicates that the majority of the Al and Au strays are created by higher energy photons created within the sample such as $\text{Ni}_{K\alpha}$, hitting the sample holder. When the acceleration voltage is too low to excite these high energy photons, the Al and Au strays are minimized. If compositional analysis of Au and Al is to be done in the SU9000, lower voltages have to be used in order to minimize creation of strays of the same elements. The higher number of stray X-rays in the SU9000, especially in the low energy photon range, is inconvenient for accurate quantitative EDS analysis because of peak overlap at several photon energies. Accurate EDS compositional analysis can be enabled by considering alternative hardware design solutions. For example, a collimator can be added in front of the large detector, which reduces X-ray from other directions than the sample area. Alternatively, the holder can be optimized by replacing the Al clamp with another material. If Al is an element of interest, Cu or Be are alternatives, where the latter is more expensive.

To summarize, the test specimen has proven to be valuable for identifying strays in the system. This is particularly important for analysis of EDS spectra where model fitting is required. A prerequisite for using the built-in method in HyperSpy that fits each individual peak to a Gaussian, is that all elements are predefined. If not, the modelled spectra will deviate significantly from the raw data.

EDS detection features and ratios

Here, the calculated EDS detector and instrumentation characteristics presented in Tab. 2.3 is discussed and compared for all three instruments and their mounted EDS detector (see 4.1). The spectra discussed and compared in this section are the PointIDs taken at 30 kV in SU9000 and 200 kV in 2100 and 2100F. The voltage dependence and map versus Point ID is commented on in the next section.

Energy resolution and peak shape Detector specific features such as the energy resolution and peak shape is evaluated through the FWHM and FWHM/FWTM respectively. The energy resolution for the Ultim Extreme in the SU9000 is calculated to be 131 eV, and 131 and 133 for the X-Max in the 2100 and 2100F respectively, all for process time setting 4. All these results are only a few eV different to the energy resolution of 130 eV stated by the manufacturers. Nevertheless, the EDS spectra acquired for subsequent quantification EDS analysis was adjusted to have the correctly calculated energy resolution to ensure optimized data processing. The energy resolution for the X-Max 80 detector was also calculated to be 133 eV in previous studies [44]. Additionally, deviation in energy resolution between the 2100 and the 2100F is negligible, and it can be stated

that the energy resolution has not been degraded in any practical sense over time or during the installation process. The shape of the $\text{Ni}_{K\alpha}$ peak in all instruments are between 1.84 and 1.87, which is similar to an ideal Gaussian with peak shape 1.80. Therefore, it is likely the ICC is not an issue in either detectors. This is usually the case for SDD detectors, since they have an extremely thin dead layer compared to older Si(Li) detectors.

An energy resolution of 130 eV is not sufficient if lines more than the resolution gap is to be distinguished. One such example is the $\text{Ni}_{L\alpha}$ and $\text{Ni}_{L\beta_1}$ peaks with energy 0.8511 keV and 0.8683 keV, i.e. an energy difference of 172 eV. In theory, these should be distinguishable. However, the $\text{Ni}_{L\beta}$ line is not visible as a separate peak, but instead contribute to a higher $\text{Ni}_{L\alpha}$ count. The $\text{Ni}_{L\gamma}$ peak on the other hand with energy 0.7429 keV is clearly visible in all three spectra as a distinguished peak. Even though the energy resolution is similar to what is stated by the manufacturers, the user should be aware of the limitations of the energy resolution of such detectors. If a better energy resolution is required, EELS can be considered as an alternative method, with typical energy resolution of 1-1.5 eV with a field-emission gun (FEG) setup [11].

Energy scale calibration Based on the position of the $\text{O}_{K\alpha}$, $\text{Ni}_{K\alpha}$ and $\text{Mo}_{K\alpha}$ peaks relative to their theoretical value, the true channel size in each spectrum is calculated. The default channel size is 10 eV, and the true scales deviate with up to 0.04 eV of the initial value. Taking an increase of 0.04 eV in each channel and a spectrum with 2048 channels, the total collected deviation at the last channel is 82 eV. This is lower than the energy resolution, which means that the correction for energy scale is in practice insignificant. Nevertheless, the spectra used for subsequent quantification is calibrated with the correct energy scale to optimize the quantification results. Specifically it is important that the peaks are positioned correctly for extracting the peak intensity and background in HyperSpy.

Stray radiation The stray radiation present in the AEM columns for all instruments were evaluated by calculating $R_{\text{Ni}K\alpha/\text{Mo}K\alpha}$ peak ratio, and are shown in Tab 4.1. Recall that a higher value is associated with less stray radiation present in the column. The ratio values are 95, 53 and 18 for SU9000 at 30 kV, 2100 and 2100F at 200 kV respectively. These are higher than the expected value which range between 3 and 7, reported by [34]. The standard test and the expected values reported are based on Si(Li) detectors. Si(Li) detectors have a high photon detector efficiency of 100%, which is not true for SDD detectors (see Fig. 5.2). Therefore, the thinner SDD detectors with lower detection efficiency measure a lower $\text{Mo}_{K\alpha}$ intensity, which could explain the higher $R_{\text{Ni}K\alpha/\text{Mo}K\alpha}$. In order to compare the results to previous reports from Si(Li) detector, the calculated values can be corrected for low detection efficiency at higher photon energies. By assuming the linear degrading trend of the detector efficiency for SDDs seen in Fig. 5.2a continues for values higher than what is seen in this figure, the efficiency can be estimated to be 50% at the $\text{Mo}_{K\alpha}$ energy. By dividing all $R_{\text{Ni}K\alpha/\text{Mo}K\alpha}$ ratios with a factor 2, the numbers are more

comparable, which is also discussed by Nylund [44]. Even so, the values are still up to 7 times higher than the expected values. Previous studies of the equivalent EDS systems in 2100 reports $R_{NiK\alpha/MoK\alpha} = 69$, $R_{NiK\alpha/MoK\alpha} = 67$ in the 2100F with single tilt holder [44]. First of all, the calculated ratios are generally in the same range, and it is therefore plausible to assume that the increase in $R_{NiK\alpha/MoK\alpha}$ compared to reports from the 90s [34], can in fact be attributed to a low amount of stray radiation, caused by improvement of TEM columns and electron guns over the last few decades. Secondly, the noticeable decrease in the 2100F since the last characterization may indicate that the amount of stray radiation has increased.

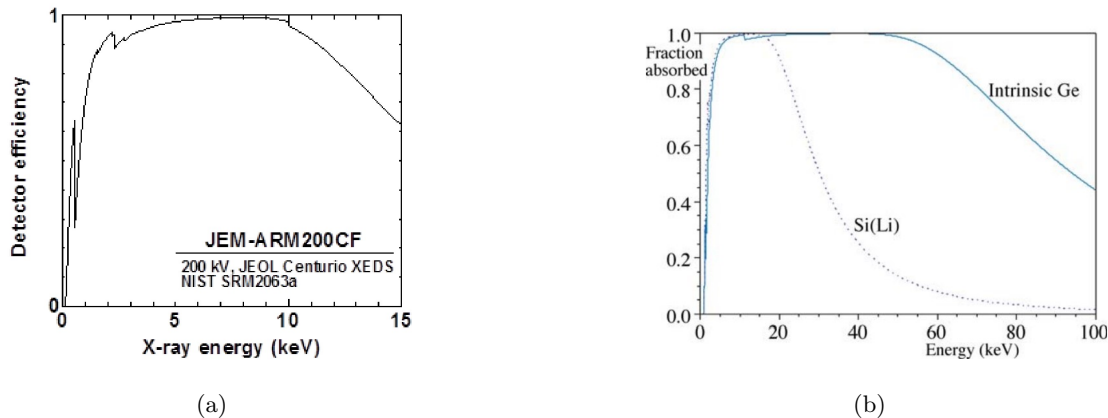


Figure 5.2: Detection efficiency for (a) SDD detector reproduced from [49] and (b) Si(Li) detector, as well as intrinsic Ge detector reproduced from [11].

In addition to being developed to Si(Li) detectors, the standard test is also based on TEM measurements at high voltages (80-400 kV). The $R_{NiK\alpha/MoK\alpha}$ presented here from the SU9000, is calculated at the instruments highest operating voltage, which is 30 kV. The fact that the incoming electrons have an energy ~ 1.5 times higher than the critical ionization energy of the $MoK\alpha$ peak will lead to a lower ionization cross section (see overvoltage Fig. 2.10). Therefore, the $MoK\alpha$ strays generated by stray electrons will not be as large of a contributing factor, causing the higher $R_{NiK\alpha/MoK\alpha}$ compared to values at 200 kV.

Predominant source of stray radiation The predominant source of stray radiation is evaluated with the $R_{MoK\alpha/MoL\alpha}$ peak shown in Tab. 4.1. The manufacturers of the test specimen reports $R_{MoK\alpha/MoL\alpha}$ between 1 and 10 indicate that the main source of strays are electrons, while values in the order of 100 imply X-rays as the main source of strays. In the TEMs, this value is 2.2 and 2.1 in 2100 and 2100F respectively, suggesting electrons are the predominant source of stray radiation, which is similar to previous characterization of similar EDS setups in these instruments [44]. This is still true if the values are multiplied by a factor of 2 to correct for low detection efficiency at high photon energies.

In the SU9000, $R_{MoK\alpha/MoL\alpha} = 0.07$, which also indicate electrons are the predominant source of stray radiation. However, this low value compared to the TEMs is influenced by the low overvoltage as previously discussed. The incident electrons have an energy 1.5 times higher than the $Mo_{K\alpha}$, which will significantly reduce the generation of these X-rays compared to 200 kV. Additionally, it was observed that for example the $Al_{K\alpha}$ peak was significantly reduced at 5 kV, when there is no generation of high energy photons within the sample, which indicates that these high energy photons is a major source of strays in the system. Evaluating the source of stray radiation in LV AEMs can therefore not be done by comparing to existing literature, and needs to be considered as dedicated study.

Intensity to background ratio The amount of background radiation present in the EDS systems are investigated using the Fiori definition in order to better compare different instruments. It is reported that for modern 100-200 kV TEM, the P/B ratio should be close to 3000 [34]. For both HT TEM in this work, the P/B ratio is lying slightly above 4000, which indicates low amounts of background radiation. Additionally, these values have not changed since the last characterization in 2017.

The SU9000 on the other hand has a P/B ratio of 900. Initially, this value is indicative of high amounts of background radiation. However, the low value should be attributed mainly to the low generation of $Ni_{K\alpha}$ X-rays due to the low overvoltage. Nevertheless, a higher background is detected with the detector in the SU9000, especially in the low energy range. This a direct consequence of the windowless large detector detector. Since the detector is windowless, the low energy photons that are usually absorbed by the window reaches the detector, creating a higher background. This can be inconvenient especially when the background is to be subtracted from peak intensities in the low energy range. Even so, the windowless Ultim Extreme detector has advantages, such as high collection efficiency for low energy photons compared to window protected detectors. This can be useful for EDS characterization of materials such as N (0.39 keV), which has been done for example with AlGaN nanostructures, used in ultraviolet LED applications [50].

Data type and voltage effects in SU9000

Map versus PointID As discussed earlier, it is important to record a spectra from a homogeneous area representative of the entire film. This can be ensured by recording an EDS map of for example $100 \times 100 \text{ nm}^2$. However, the values in Tab. 4.1 show that the calculated detector parameters deviate insignificantly form each other in map and PointID data-types. This indicates that PointIDs is representative for the film and are sufficient for detector characterization. This is an advantage, seeing as PointIDs are less time consuming than map acquisition, especially if the output count rate in the instrument is low. Ideally, the status of the EDS system should be regularly checked and certainly after the detector is altered [11]. A fast

and simple data collection and routine data processing is advised, and made possible by the open source code made here.

Acceleration voltage dependence The effect decreasing the acceleration voltage has on the detector parameters was investigated in the SU9000 at 30, 15, 10 and 5 kV. The energy resolution increase with 2 eV from 30 kV to 10 kV which do not have any significant effect on quality of the following quantitative analysis. The FWHM/FWTM increase, and is 2.04 at 10 kV. Peak shapes higher than 2 is in general said to be caused by ICC [30]. ICC is an effect caused by the dead layer in the detector, which means it should not be effected by the acceleration voltage. Therefore, it is more likely that the increase in peak shape is another effect of the low overvoltage, causing the total $\text{Ni}_{K\alpha}$ intensity to significantly decrease, increasing the relative error in the measurement, and hence the peak shape. Values for the channel size does not change significantly either with decrease voltage, which is also expected as this is a detector specific parameter and not dependent on acceleration voltage. A note must be made that the energy calibration is only possible to do with the $\text{O}_{K\alpha}$ and $\text{Ni}_{K\alpha}$ peak, since the $\text{Mo}_{K\alpha}$ peak is not created with acceleration voltages lower than 17 kV.

The P/B ratio at lower voltages also decrease, especially between 15 and 10 kV. This is also likely caused by the low ionization cross section at voltages near the critical ionization energy. Decreasing P/B characteristics with decreasing voltage is also observed at HT TEMs (100-300 kV) for the $\text{Cr}_{K\alpha}$ peak from a Cr thin film measured with a Si(Li) detector in STEM mode in [51]. Additionally, this P/B dependence on voltage was theoretically predicted by [52], for overvoltages in the range 4-25 (40 - 100 kV). Be aware that in this work, the overvoltage is 1-4 for the $\text{Ni}_{K\alpha}$ peak such that the theoretical derivation is not directly transferable to this situation.

In general, it is seen that the detector specific parameters such as energy resolution and energy scale dispersion is not dependent on the acceleration voltage. The parameters that use intensity ratios on the other hand is highly dependent on the overvoltage. Most accurate detector characterization using the standard test presented here therefore has to be done at 30 kV. This is generally the practice for EDS calibration in SEMs, as a high count rate is needed for accurate calculations. An alternative is to change the calculated ratios. For example, measuring the low energy $\text{O}_{K\alpha}$ P/B ratio instead of for the $\text{Ni}_{K\alpha}$.

Tilting effects

For thin specimen quantitative EDS, high count rates are imperative [11], which is improved with SDDs with a larger solid angle as it can be placed closer to the specimen. However, part of the detector area could be off due to shadowing (see fig. 2.17b). Shadowing of the detector can be estimated by retrieving the intensity of significant peaks in the spectrum at increasing tilt angle. This is done with the $\text{O}_{K\alpha}$ and $\text{Ni}_{K\alpha}$ peak, and plotted for all instruments in Fig. 2.17. The

spectra for shadowing inspection were acquired with an increment of 5° . Therefore the exact angle at which shadowing occurs cannot be extracted directly from these data, but an estimate can be made. First of all, shadowing is present in all three instruments and is assumed to be caused by the holders. In the SU9000, a substantial decrease in the peak intensities are observed between 15° and 10° . Despite a high shadowing angle, low count-rates are rarely a problem in this instrument due to the windowless detector, and high adjustable probe currents up to $20 \mu\text{A}$. This is especially seen in the $\text{O}_{K\alpha}$ intensity, which is consistently higher in the SU9000 than in the TEMs. The $\text{Ni}_{K\alpha}$ is on the other hand lower, but can be attributed to the low voltage, causing less generation of this peak as previously stated. For the EDS detector when mounted in the 2100, the shadowing angle is assumed to be between 10° and 5° . After the detector was moved, the angle at which shadowing occurs is higher, i.e. between 10° and 15° . Additionally, the total intensity of the peaks have decreased. This suggests that the detector has not been positioned for optimal count during installation. Earlier reports [44] of previous EDS setup in the 2100F record a shadowing angle around 5° , which is more optimal than the current setup. Hence, the detector must be repositioned, and afterward characterized by routines used here to achieve minimal shadowing when the specimen is flat at 0° tilt.

Even though the shadowing of the detector is a good indication that the detector placement is not optimal, a more informative calculation would be to find the collection solid angle. This is included in the standard test [16, 33], but is not included here, as it requires measurements of the probe current. It should be considered for future work as it is a more precise measure of the actual performance of the detector.

Quantification

An additional test was carried out using the test specimen with known stoichiometry to test the stability of the Cliff-Lorimer quantification model. As can be seen in Tab. 4.2, the values for C_{N_i} and C_O deviate increasingly from the expected concentration ratio ($C_{N_i}/C_O = 1$) at lower voltages. This confirms that the Cliff-Lorimer method is not reliable, especially at lower voltages, as the calculated k-factors are not accurate. Even at 30 kV and 200 kV, the concentrations are within $\pm 7 \text{ at.}\%$ of the true composition. Note that the ICD approach cannot be used on this specimen as there is no internal reference or benchmark element.

5.2 Heterostructure GaAs/GaAsSb NWs

Here, the results of the axial heterostructured GaAs/GaAsSb NWs is further elaborated and discussed. During this work, this was been the main sample used to study the performance of ICD quantification method in LV STEM. First, the observations made during preliminary sample inspection will be commented on, as it may influence the subsequent EDS quantification. Then, a detailed review of the quantification results and their implications is given.

5.2.1 Preliminary sample inspection

The crystal structure, morphology and composition of the III-V heterostructured GaAsSb NWs used for quantitative EDS analysis in this work has previously been studied and characterized. For a detailed review see [1, 21, 41, 53]. Nevertheless, preliminary imaging of the wire sample provided for this project (see Fig. 4.6) was carried out prior to the EDS mapping in order to find suitable areas for EDS analysis, as well as crystal orientation. ICD requires both a reference area, where the Sb concentration is assumed to be zero, and the an analysis area of interest. In the case of these heterostructured wires, the GaAs spacers between the SLs is the reference area, and the SL with layers containing Sb is the analysis area. In order to identify the SLs and the spacers, Z contrast in HAADF STEM and BSE SEM is applied as seen in Fig. 4.6c and 4.6d respectively. An adequate Z contrast to determine the position and size of the SLs and wells is obtained using HAADF STEM in the 2100 at 200 kV. The SU9000 is also equipped with an ADF detector with adjustable camera length. However, no HAADF contrast was obtainable in this instrument. It is likely that the mean free path of the electrons at 30 kV in the material is too small compared to the thickness of 100 nm to produce a detectable transmission signal [54]. Other literature also state that the decrease in HAADF contrast in LV SEMs with increasing sample thickness is caused by beam broadening [47, 55]. However, reducing the sample thickness will simultaneously reduce the generation of characteristics, which will degrade the count-statistics and consequently the accuracy EDS analysis. BSE imaging in the LV STEM can instead be used, and an atomic number contrast was observed as seen in Fig. 4.6d. However, it is not as evident as in the 2100, and much harder to obtain.

The crystal orientation of the wire needs to be identified prior to EDS mapping, as it can influence both the measured intensities of the characteristic X-rays, as well as the spatial resolution of the mapping. It was found in the 2100 that the wire was on zone axis $[\bar{1}\bar{1}0]$ when the holder was tilted to $+7^\circ$ x-tilt (rotation along the long axis) and $+14^\circ$ y-tilt (rotation along the wire short axis). Generally, ensuring that the mapped area is uniform and homogeneous is done by acquiring EDS maps near a zone axis. Especially, since the concentration variations in these wires vary axially, recording an EDS spectra should be done with the correct y-tilt. The SU9000 does not have the ability to tilt the sample in the y direction, which will effect the spatial resolution of the

EDS mapping as well as reducing the Sb content in the GaAs/GaAsSb interfaces as seen in Fig. 5.3. Note that there is no method to identify the crystal orientation in the SU9000, and since it is near impossible to insert the sample exactly the same relative to the incoming beam in the two instruments with different holders and setups, the exact crystal orientation of the wire in the SU9000 is unknown.

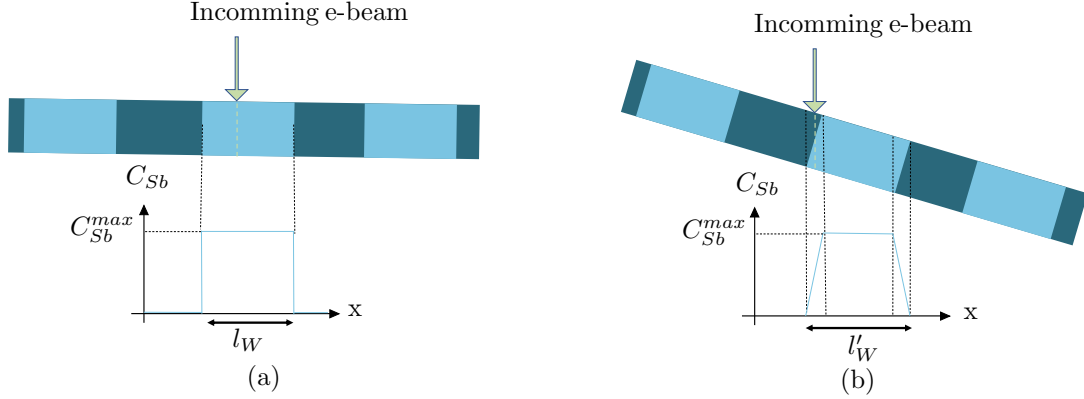


Figure 5.3: Schematic illustration of how spacial resolution is degraded when the wire is not tilted on zone in the y-direction. For visualization purposes, assumed no beam broadening in sample. (top) The wire is on zone and assuming that the Sb concentration is constant within the well with length l_W as seen in the concentration profile below. (bottom) The wire is not tilted on zone in the y direction, leading to a longer well length, l'_W with a gradual increase and decrease in Sb concentration at the GaAs/GaAsSb interfaces.

Another effect that should be commented on is the P/B intensity ratio dependence which is addressed in [49] for a Jeol JEM-ARM where the detector is placed perpendicular to the sample holder axis as is in the 2100s and the SU9000. As is discussed in [49], P/B decreases significantly with x-tilts away from the detector, but as long as the sample is tilted towards the detector the dependence is minimal. Similarly, it is stated that the P/B ratio is not influenced significantly by y-tilt and the effect is assumed to not degrade the quality of the subsequent EDS mapping.

5.2.2 Quantitative EDS analysis

Implementation of ICD method

Quantification of the GaAsSb superlattices has been carried out using the Internal composition determination for the first time in the HT TEM 2100 as a reference, and in the LV S(T)EM SU9000, all with Oxford Instrument SDDs. The only previous reported use of the method is by J. Nilsen who developed the method, who used EDS data on similar samples in the JEOL ARM 200F at 200 kV equipped with a Centurio SDD EDS detector [15]. Therefore, this is the first report of successful use of the ICD method in a low voltage instrument and uncorrected TEM

set-ups. The factorless method is proven to be advantages to the standard quantification methods such as the Cliff-Lorimer or the ζ factor methods for several reasons. First of all, the significant advantage of this method is that the iterative process only requires X-ray line intensities and a known reference area as input parameters, and based on this, the algorithm provides quantitative compositions, in addition to sensitivity factors and a relative thickness profile. The calculated sensitivity factors can then be used for other measurements and compared to standard calculated values. The thickness profile can be a result in of itself, or be used as a validation test to evaluate the calculated compositions. For example, the expected thickness profile is flat for FIB lamellas or the hexagonal shape across a NW (see Fig. 2.4).

Applying the ICD algorithm to EDS data from a LV STEM was achieved by customizing the code developed by J. Nilsen, to this specific problem. The main difference between applying the method to high and low voltage EDS data is that L-lines for Ga and As has to be used at voltages <15 kV. In principal these lines are generated at voltages >11 kV. Nevertheless, the ionization cross section is close to zero when the energy of the incoming electrons become comparable to the critical ionization energy [11]. Consequently, the intensity of the peaks, i.e. the count statistics are significantly reduced, increasing the relative error of each measurement. In addition to the X-ray lines used, the benchmark element (Ga), the unknown element (Sb) and the reference area (GaAs) has to be specified by the user. With these modifications, the method provided quantitative concentration profiles similar to previous reports of the Sb variations within the wires and will be discussed in upcoming paragraphs.

The method is compared to quantitative calculations using the standard Cliff-Lorimer method. Previous studies of Cliff-Lorimer by the author where whole core-shell NWs was studied [17], showed that the quantitative results was highly dependent on both instrumental settings, as well as the type of X-ray line used. This was assumed to be due to the lack of accuracy in the calculated k-factors in the model. Previous studies of similar GaAsSb NW also shown that the EDS analysis to determine the Sb content has a limited accuracy [53, 56]. The error related to the Cliff-Lorimer method is further established by the quantification of the NiO sample studied for characterization of the EDS detection system (see 4.2). Here, the calculated composition deviates increasingly from the known stoichiometry with decreasing operating voltage. Since the internal determination of composition is a factorless method that does not require such sensitivity factors as input parameters, it is thought that this method will provide quantitative composition results independent on the instrument parameters.

General observation in concentration profiles

All Sb concentration profiles exhibit periodic variations within the SL with a gradual increased to a maximum Sb value. This same gradual increase is previously reported [1], and is attributed to a short-time supply of Sb flux in combination with a reservoir effect in the catalyst [57] caused by

high Sb solubility in the Ga catalyst and reduction of supersaturation by the Sb incorporation in the wire. Converting the Sb variations with this "saw-tooth" pattern to the valence band potential [58], the electronic structure can subsequently be modelled as a triangular finite potential well.

In theory, the ICD method should have a built in absorption correction contrary to the standard Cliff-Lorimer method. It is observed in all concentration profiles for the GaAsSb NWs, that the Ga composition is overestimated, and the As composition is underestimated using Cliff-Lorimer. On average, the Cliff-Lorimer Ga/As concentrations are 3.7 at.% higher/lower than using ICD. This can be explained by the difference in mass-absorption coefficients for Sb compared to Ga and As. As seen in Tab. 2.2, $Sb_{L\alpha}$ is absorbed more than both elements, especially within the Pt protection layer in the FIB sample. Additionally, the absorption of $As_{K\alpha}$ in Ga is also significantly higher than for $Ga_{K\alpha}$. Combined, these two absorption effects cause the Cliff-Lorimer Ga concentrations to be overestimated, as they are not corrected for absorption effects. The same argument can also be made to explain why the Sb concentrations is consistently lower using Cliff-Lorimer. These observations are similar to what is previously reported [15], and is an indication that the ICD method indeed handles absorption effects.

In order to investigate the calculated ζ factors for Ga and As in the internal determination method, the reference area the calculations are based on was set to be only a portion of the Sb free GaAs spacers. As can be seen in all concentration profiles in Fig. 4.9 and 4.10, the Ga and As concentrations are stable around 50 at.% within the reference area. This is expected seeing as the ζ factors are calculated based on the assumption that C_{As} and C_{Ga} is in fact 50 at.% in this region. Nevertheless, the concentrations maintain the same values within the regions of the GaAs spacer that has not been forced by the algorithm to have $C_{As} = C_{Ga} = 50$ at.%. This is an indication that the calculated factors are not only valid within the reference area, but also for the rest of the mapped area. The calculated ζ factors with unit kg electron/m²/photon are $\zeta_{Ga} = 124$ and $\zeta_{As} = 153$ in the 2100 and $\zeta_{Ga} = 328$ and $\zeta_{As} = 495$ at 30 kV in the SU9000 at 20° tilt. The calculated ζ factors vary with tilt, and should be compared to experimental determined factors for the used set-ups, but this requires known probe current and having a standard specimen with known composition and thickness [11, 59].

Tilt and voltage dependence

In addition to comparing the ICD method to Cliff-Lorimer quantification, the reliability of the ICD method with respect to instrument parameters such as tilt and accelerating voltage was investigated. Tilting the sample to 20° could degrade the uniformity of the mapped area, but it will ensure no shadowing of the detector. More importantly, as discussed in theory, the projected thickness within a sample increases with increased tilt, and the absorption path length decreases. Therefore, absorption effects should be more significant at 8° tilt. It is possible to include absorption correction in Cliff-Lorimer as described by Goldstein et al. [39]. Absorption correction for k-factors

has been attempted to improve the accuracy of SEM EDS, however absorption coefficients are frequently inaccurate and additional error is introduced as the thickness of the specimen has to be determined with a high accuracy [13, 60, 61]. In this work Cliff-Lorimer quantification was done without absorption correction. Therefore, the Cliff-Lorimer results should deviate more from the ICD results at 8° than at 20°, but this is not what is observed. As can be seen in the results in Tab. 4.3, the discrepancy between Cliff-Lorimer results and ICD results are inconsistent with a higher deviation at 20° tilt. In order to understand this behaviour, a more elaborate explanation is needed, and is discussed in upcoming paragraphs.

While tilting will effect the degree of absorption, altering the acceleration voltage will effect the material and specimen specific parameters that determines the X-ray intensities according to Eqn. 2.7, and consequently the sensitivity factors according to in Eqn. 2.10 and 2.15 for k - and ζ factors respectively. The error in calculating sensitivity factors lies in these expressions, as parameters like ionization cross section, fluorescence yield etc. are difficult to calculate with a high accuracy. It is generally known that the main source of error contributing to high uncertainty with calculating sensitivity factors is the ionization cross section [62]. In HV TEMs, these physical parameters stay relatively unchanged when the voltage is varied. However, in a LV STEM, the energy of the incoming beam (1-30 kV) is similar to the critical ionization energy, and these parameters become increasingly sensitive to changes in the acceleration voltage. Therefore, it is of great advantage that the ICD method calculates the sensitivity factors for all elements of interest without the need for specimen thickness or the aforementioned physical parameters. As can be seen in Tab. 4.3, the calculated ζ -factors are different for each measurement series. Furthermore, the ζ -factors can be used to calculate k -factors by using that $k_{AB} = \zeta_A/\zeta_B$. Calculating the $k_{Ga,Sb}$ at 200 kV, 30 kV and 15 kV (where K lines is used for Ga), the result is $k_{Ga,Sb}^{200} = 0.70$, $k_{Ga,Sb}^{30} = 1.26$, $k_{Ga,Sb}^{15} = 2.02$. As can be seen, the k -factor increases with lower overvoltage, when the ionization cross section for $Ga_{K\alpha}$ decreases, and should remain relatively constant for $Sb_{L\alpha}$ (see Fig. 2.10). This indicates that the ICD method automatically compensates for the variation in physical parameters at low voltages. Consequently, the method provides experimentally determined k -factors without the need for element standards, absorption correction, sample thickness measurements, probe current etc. required in the standard methods [63–65]. Note that the accuracy of these calculated k -factors is yet unknown.

Instability and sources of error in ICD

Based on prior studies of EDS quantification in LV SEM, the Cliff-Lorimer results are expected to have a low precision and depend on the experimental setup (i.e. voltage and tilt) [17], while the ICD method should be less dependent on instrument parameters and provide stable quantitative calculations. However, the results indicate otherwise, as the maximum Sb concentration varies more between each measurement series as seen in Tab. 4.3. The maximum Sb values using Cliff Lorimer

are all within 1.0 at.% of its average of 5.3 at.%. while the ICD results have a higher average of 7.4 where all values are within ± 2.9 at.%. Without further inspection, these results would suggest that the Cliff-Lorimer method is in fact more reliable than the ICD method. However, it is not sufficient to conclude that Cliff-Lorimer is more accurate based solely on the fact that it is more precise for a set of data taken under different conditions. In the next paragraphs, potential sources of errors causing this instability and lack of precision in the ICD method is discussed.

Based on the results, it is not likely that the instrument settings is the main cause for the variations in quantification, since there is no clear pattern relating the calculated concentration values to either tilt or voltage. Instead, it is likely that the cause lies within the assumptions and built in requirements behind the ICD method. It is stated that the algorithm is sensitive to three characteristics of the experiment/specimen. The first is changes in electron channeling, the second is changes in thickness and the third is noise levels. Each of these characteristics is discussed below.

Electron channeling along specific atomic columns, causing preferential generation of certain X-ray lines needs to be taken into account when doing EDS. It is generally known that this is avoided by doing EDS off a zone axis. Electron channeling can be a desired effect as it for example is used to determine the location of impurity atoms in a method called ALCHEMI [66, 67], but has to be avoided for quantitative EDS analysis where high accuracy is desired [11]. The crystal orientation of the GaAs sample was identified in the 2100 to be at the $[1\bar{1}0]$ zone axis at a positive x-tilt of 7.1° . Electron channeling is especially important to avoid in this crystal orientation, as the atoms are arranged in Ga and As columns as seen in Fig.2.19b. At 8° tilt, it is possible that channeling effect in fact are present. Additionally, the wire is bent, such that the wire might be in an orientation where electron channeling alters the Ga to As more in some areas compared to others [68]. In the case of electron channeling along the column V atomic columns, the As concentration is overestimated, and the Sb value is underestimated, and oppositely along the column III atomic column. However, since the wire is not tilted in the y-direction in the SU9000, and the crystal orientation relative to the incoming beam is not determinable, exactly which channeling effects that might occur is not known. Likely the relative lattice-beam orientation is more than a few degrees from a low index channeling sensitive zone and hence the observed III-V ratio should not be affected by channeling effects [68]. Additionally, electron channeling should effect the Cliff-Lorimer results as well, which does not seem to be the case. In general, electron channeling is an effect that might have effected the results, but to what degree is yet unknown, and could be investigated further and potentially utilized.

Thickness of the sample, and its effect on the absorption within the sample is a critical aspect in the ICD method, and can be assessed by the thickness profile provided in the model as verification method. One key assumption in the ICD method is that the absorption of all the X-ray lines is equal within the analysis area. The effect thickness variations has on absorption was studied by J. Nilsen in tapered $I_x\text{Ga}_{1-x}\text{N}$ NW [15]. In the case of the GaAsSb NW studied

here, the FIB sample preparation should ensure that the wire is flat with a constant thickness within the analyzed area, which is also established by the lack of topography contrast in SE imaging. Therefore, the absorption of a specific X-ray should not vary due to thickness variations. However, all measurement series exhibit uneven and inconsistent thickness profiles. The difference in thickness lie between 6-8 nm for most experiments, which constitute 6-8% of the sample thickness of 100 nm. In the case that the thickness indeed do vary across the mapped area, the profile should still not vary between measurements, which is what is observed. Hence, the verification method for ICD indicated that some determinations have to be taken with reservation.

It is not known for which of the HTs calculated relative thickness profile is nearest the true profile, and hence which concentration value is most reliable based on this verification method. Nevertheless, an interesting observation is made that the thickness profiles for each specific acceleration voltage is similar at both tilts. For example, both thickness plots at 15 kV exhibit relatively flat profiles, indicating that the calculated Sb max concentrations of 7.9 at.% and 6.9 at.% at 8° and 20° tilt are more reliable than the other results. Additionally, based on [57] and [15], the expected value can be assumed to be around 8 at.%. This means that the average is closer using ICD, and that tilting the sample to 20° gives the most precise result at 30, 15 and 10 kV. However, these previous calculations are Cliff-Lorimer based EDS analysis, which means that this conclusion cannot be directly drawn. Evaluating the accuracy of the quantification results in this work is in general challenging, due to the lack of a "ground truth" composition, seeing as previous composition characterization is also based on Cliff-Lorimer EDS. Therefore it could be of interest to compare the results to other compositional techniques such as CL and EELS in the future [69, 70].

Noise in EDS signals is in general a challenge, especially if the count statistics are low [11]. In this work, the maps are binned in order to increase the signal to noise ratio for each data-point. However, the final concentration profiles still display a significant level of noise. Seeing as the Ga concentration is known to have a constant value throughout the entire area, the level of noise can be assessed as it is reflected in the final flatness criteria, ΔC_{Ga} . The purpose of the flatness criteria in the algorithm is optimize the unknown ζ -factor to compensate for absorption effects. However, in these datasets, the noise level of the recorded spectra seems to be higher than the changes in the benchmark element due to absorption, and the flatness criteria has instead become a "noise criteria". The noise in the EDS system will be different from one measurement to another. Therefore, the final calculated ζ -factor for Sb will depend on the level of noise, and can be the reason why the composition results are different between each measurement. The uncertainty of the ICD method is also reflected in the flatness criteria. The flatness is between 3.3 at.% and 8.7 at.% for all measurements, which is further indication that the noise levels of the EDS data increases the uncertainty of the method in this case. However, it is worth pointing out that the initial flatness of the Ga composition (during the first iteration of the code), has been improved

in the final calculated values. Therefore, it is possible that flatness in Ga concentration caused by difference in absorption between the X-rays, has been corrected, and that the final flatness is the noise, which the code cannot eliminate.

In order to eliminate, or at least minimize noise effects, denoising can be done using for example decomposition by principal component analysis (PCA). The method reduces the dimensionality of large datasets by reconstructing the data from a number of orthogonal eigenvectors (components). [71, 72]. This is a commonly used method for denoising in HyperSpy. Generally, denoising can be beneficial, especially in EDS data with low count statistics. However, the accuracy of the reconstruction is now known and can possibly exclude data that is not noise [73]. Additionally, due to the high collection angle of the detector and the high probe current, the output count-rates in the SU9000 are well above 10 000 cps, usually above 20 000 cps, such that the signal to noise ratio is high. Therefore, the raw data is thought to be more reliable in this case the main analysis in this work has been performed on raw data. Nevertheless, concentration profiles after denoising the data from the measurement series in Fig. 4.10 and 4.9 can be seen in Appendix B.1. Here it is observed that in some cases, the Ga concentration varies in phase with the Sb concentration using Cliff-Lorimer, which is also observed by J. Nilsen [15]. This is assumed to be another effect caused by the aforementioned high absorption of Sb compared to Ga X-rays, and is seen in the Cliff-Lorimer method as it lacks an absorption correction. These are the kind of Ga variations the flatness criteria is intended to correct. As can be seen in Tab. B.1, the final flatness of the denoised data is between 0.2 and 1.7 at.% for all profiles, which is a significant improvement compared to the raw data. Additionally, the Sb maximum concentration values looks to be more stable (excluding the outliers at 5 kV 20 tilt and 10 kV 8 tilt). It can be interpreted the ICD approach that uses a flatness criteria is not suited as the source for the roughness is not absorption, but noise. Once the noise is stripped, the flatness is hugely improved, and the roughness in the benchmark element is due to absorption rather than noise and the ICD approach works better.

Advantages and challenges to LV STEM EDS

Up until now, several factors contributing to low accuracy in quantitative EDS has been discussed. This has revolved around the use of sensitivity factors, absorption effects, electron channeling, noise and stray radiation in the detection system. Here, some general advantages and challenges to EDS in LV STEM is commented on.

One of the main advantages to LV STEM EDS is that the generation depth of the X-rays decrease with decreasing beam energy, which consequently leads to a higher spatial resolution [39, 74]. Development of stable FEGs has also enabled smaller nanometer resolution for low (<5 kV) voltages [75]. Additionally, a lower X-ray generation depth leads to lower absorption paths and therefore easier detection of lighter elements ($Z < 10$) [76]. Detection of such low energy photons has also been improved by the development of the SSDs, in addition to windowless detectors that allow for

high collection efficiency in the low energy part of the spectrum [77].

Despite these obvious advantages to LV STEM EDS, quantitative analysis is known to have better accuracy when K lines are used compared to L lines [76, 78]. Additional error is also introduced by the many X-ray line overlaps in the low energy range. Furthermore, all EDS quantification methods discussed in this work is based on the thin film criteria. Watanabe et al. [32] states that the critical specimen thickness where 5% X-ray absorption occurs is well above 100 nm for most K-lines. However, for L-lines, this is significantly reduced. Therefore, it is also possible that the underlying fundamental thin film assumption is in fact not valid when $\text{Ga}_{L\alpha}$ and $\text{As}_{L\alpha}$ lines are used (10 and 5 kV).

Advantages to ICD

EDS is a widely used technique for compositional analysis due to its technical simplicity and availability in most modern electron microscopes. Furthermore, most users place confidence in the quantitative EDS analysis calculated in the operating software, such as Aztec, without being aware of the related uncertainty. Usually, quantitative computations in such detector soft-wares are based on Cliff-Lorimer quantification. Neither the source code used for conversion from spectrum to composition, or the calculations to determine k-factors are disclosed in any published writing as far as the author knows, limiting the transparency and accuracy of the quantitative analysis. ICD on the other hand is currently implemented using the open-source library HyperSpy, and made available to apply in other systems in the original work by J. Nilsen [45] and in this work (Appendix A.3).

The need for an easy to use quantification method with high accuracy is clear. Over the last decade, several alternative methods have been suggested. Thickness dependent effective sensitivity factors can be calculated based on Monte Carlo (MC) simulations of X-ray generation [12]. Alternatively, extrapolated k-factors can be found by making suitable standards in combination with MC or multivariate statistical analysis [13, 14]. However, due to their need for complex simulation tools or element standards, the methods are rarely considered by the average every-day EDS user. This is where the ICD methods is clearly advantageous. The only requirement for the analysis is to have an area with known composition and an benchmark element present, which is usually the case in ternary III-V heterostructures.

5.3 Heterostructure GaAs/AlGaAs NWs

In this section, the results from quantitative analysis of the radial AlGaAs heterostructured NWs is discussed. The axial GaAsSb heterostructures in the previous section was used to study the stability and precision in ICD versus Cliff-Lorimer quantification. The AlGaAs NWs discussed

in this section were analysed to investigate the effect of the Al stray present in the SU9000 that was observed during characterization of this detection system. Note that the sources of error and instability in the ICD method is still a concern in these measurements. The noise levels are significant, especially at low voltages. Channeling effects can likely be neglected as the atoms are not arranged in Ga and As columns in this orientation (see Fig. 2.19d). Lastly, the thickness of the specimen should be relatively constant due to the ultramicrotomy preparation and absorption is assumed to be constant within the scanned area.

As previously discussed, the Al strays originate from the horseshoe clamp on the STEM holder. It is assumed that the majority of the $Al_{K\alpha}$ strays are generated by higher energy photons such as $Ga_{K\alpha}$ and $As_{K\alpha}$. As can be seen in the EDS spectra from the core (see Fig. 4.12), where the recorded $Al_{K\alpha}$ signal should be zero, the Al stray is significantly reduced, even though not entirely gone at 5 kV. Nevertheless, both qualitative and quantitative EDS analysis of $Al_{K\alpha}$ should be more reliable and accurate at lower voltages such as 5 kV, where $Ga_{K\alpha}$ and $As_{K\alpha}$ are not generated. As can be seen in the $Al_{K\alpha}$ intensity map of the wire cross section in Fig. 4.11b, the Al stray contributes significantly to the recorded spectra. In the core, it is known that the Al content is zero [15, 42], but a high $Al_{K\alpha}$ signal is recorded within the entire core.

The concentration profiles at 30 kV in Fig. 4.13a and 4.13b show a calculated Al content of 95 at.% and 28 at.% for ICD and Cliff-Lorimer respectively. At 5 kV on the other hand, the Al concentration is close to zero within the core. Additionally, using ICD, the Ga and As concentrations are averaged around 50 at.% within the reference area. Consequently, it is established that in order to quantify Al content in this instrument, low voltages have to be used. However, due to low ionization cross section the count rate is very low leading to a high noise to signal ratio. If this could be improved, qualitative and quantitative analysis of Al seem to be obtainable if lower voltages <7 kV are used.

The results at 5 kV can be compared to previous studies of similar core-shell NWs. ICD determination of the same sample shows an increase in the Al composition towards the core from ~ 20 at.% to 35 at.% [15]. Here, the shell concentration calculated in this work is lower for both methods. Additionally, it is previously found that the Al concentration in the shell in similar core-shell NWs is arranged in Al rich lines parallel to the $\{110\}$ side planes [42]. As can be seen from the concentration profiles in Fig. 4.13a and 4.13d, it is obvious that the signal to noise ratio and the spatial resolution of these maps are too low in order to observe these Al rich lines within the shell.

In summary, it is shown that qualitative and quantitative EDS determination of Al in the SU9000 is improved by reducing the acceleration voltage. However, the Al stray is still present, and quantification is not optimal as compared to previous reports of the Al composition in these cross section samples. Therefore, the apparent problem with the Al strays in these instruments has to be resolved in order to improve EDS analysis of Al alloys in the future. This will be commented on in Sec. 6.3.

6 | Future work

This work consists has consisted of two main tasks, which has been i) to characterize the EDS detection systems used, specifically the new windowless system and ii) to implement the recently developed ICD quantification method on LV EDS data for the first time. The results and discussion revealed room for improvement and aspects to be considered regarding both. Here concrete suggestions will be proposed to improve the quantification by EDS for III-V semiconducting nanostructures.

6.1 Develop alternative detector characterization standard test

The EDS detection system test that was carried out in all detection systems in this work is based on the work by Egerton et al. [16]. These are developed for older Si(Li) EDS detectors. In most modern day AEMs however, the EDS detectors are SDDs. From the results, it became apparent that calculated detector features for SDD, such as the $R_{NiK\alpha/MoK\alpha}$ and $R_{MoK\alpha/MoL\alpha}$ ratios, cannot be directly compared to expected values for Si(Li) detectors from previous reports. Therefore, it is necessary to develop or at least adapt the test and find expected values for detector characteristics more suited for SDD detectors.

Furthermore, the standard test is developed high voltage ranges (100 - 400kV), where variables such as ionization cross section, overvoltage and fluorescence yield does not have to be taken into account. Decreasing the acceleration voltage effects all these parameters, decreasing the detected X-ray intensities. This has two effects on the EDS characterization. First of all the expected values for intensity ratios, for example the peak to background ratio is much smaller in a LV SEM than at conventional HT TEM ranges. Secondly, not all X-ray lines used, such as the $Mo_{K\alpha}$ peak, will not be generated at all. Therefore, it is necessary to define other intensity ratios to measure characteristics such as strays and peak intensity to background ratio. With the flexibility of the open-source packages, this allows to use for example L lines instead of K-lines easily.

Another test sample the NiO on Mo TEM grid could also be designed. By using a Cu or Ti grid, lines or line ratio from these could be used to analyse strays. Note that Cu is not optimal due to overlap with Ni, in addition to Cu being a normal stray from most AEM stages. One also has to

reduce the background in the low energy range (see Sec. 2.2.1 Bremsstrahlung radiation). Using graphene instead of 20 nm thick C support could be of interest. These are already commercially available. Instead of NiO another stable compound is demanding, but as Egerton discusses [16], there are several phase purity and stability issues to consider. With the increasing growth of STEM in SEM [79] and larger collection angle EDS systems, characterizing the acquisition setup will become of interest. Where for low voltage SEM of bulk sample the topic is discussed in textbook [39]. Systematic EDS setup analysis test for low voltage are rarely reported.

6.2 Investigating denoising effects for ICD for LV STEM

As discussed in Sec. 5.2.2, the majority of the EDS analysis has been performed on the raw data in this work. This was done since denoising can potentially lead to loss of data, and rigorous noise and error analysis is required in order to validate the denoising procedures. In developing ICD, J. Nilsen also worked primarily with raw data [15]. An analysis in that work showed small gain from denoising and concluded that the input data had sufficient signal to noise ratio. However, in the present study, the noise level and type might be different and the signal to noise ratio insufficient. It is believed that the amount of noise present in the EDS data has indeed caused the ICD method to not work as intended. Additionally, the denoised datasets seen in Appendix B.1 show some promise concerning the expected behaviour of the Cliff-Lorimer and ICD method.

PCA is a user-friendly denoising technique that may appear fault free to the inexperienced user. However, determining its accuracy for application in quantitative EDS with reliable confidence intervals is not straight forward. Especially for EDS studies, low signal to noise ratio can lead to random noise bias. Therefore, a more systematic investigating the effect of denoising along the statistical approach recently done by [73] than initially approached here should be considered for future work. In [73], the accuracy of denoising by PCA is evaluated by analyzing PCA effect on quantitative EDS analysis of binary AuAg nanoparticles. It is found that a high accuracy is obtainable when the signal to noise ratio exceeds a minimal level, and suggests noise evaluation procedures to design experiments. Other literature also discuss PCA bias/systematic error estimators [80, 81], which can be looked further into.

6.3 Deal with Al strays in SU9000

During the characterization of the EDS detection setups prior to EDS quantification, the presence of a significant Al stray in the SU9000 was identified. If the stray does not interfere with a real characteristic peak from the specimen, like the Cu stray from the FIB half grid in the case of GaAsSb heterostructure, it can safely be ignored after identification. However, Al stray prevents both qualitative and quantitative EDS of Al in the specimen in this instruments. It was observed

that the Al stray was significantly reduced at lower voltages, when high energy photons such as $\text{Ga}_{K\alpha}$ and $\text{As}_{K\alpha}$ is not generated. This limits the generation of the Al stray from the horseshoe clamp on the holder, and the quantification was significantly improved at lower voltages. However, this is still a major problem and drawback in this instrument that needs to be dealt with.

There are two approaches to dealing with this problem. The most obvious and best solution is to remove the source of the strays. The piece can be replaced by a clamp made out of another conductive material. Preferably a material that is already present in the column, for example Cu, such that no additional strays are introduced in the EDS spectra. If eliminating the stray to the detected signal is not possible, a more elaborated approach is analyzing time resolved X-ray creation and detection. A setup has been described by Jannis et al. [82], where simultaneous measurement of the inelastically scattered electrons with a Timepix3 detector and the characteristic X-rays with an SDD is possible. Consequently, if an Al X-ray is measured simultaneously as an electron with energy loss equal to the $\text{Al}_{K\alpha}$ photon energy is detected, then it is established that the Al X-ray indeed originates from the sample. However, this is beyond the scope of this work, but is an exciting development which could be a solution for identifying strays in the future.

An essential part of the current study is the availability of open-source analysis software HyperSpy. This was essential to develop ICD and use denoising strategies as PCA (see appendix B.1) is not available in commercial packages. Hence, the question is whether it is possible to detangle the Al stray signal from the sample by making use of the flexibility available and extend the post processing. Here, some initial suggestions to how this can be done is presented on EDS data from the AlGaAs core shell cross section at 30 kV in the SU9000.

In the first approach, it is assumed that the group III and group V atoms are 50 at.% each. In other words, adding the requirement that $C_{As} = C_{Ga} + C_{Al} = 50$ at.% everywhere. By inserting this assumption in the Cliff-Lorimer method, and simultaneously assume that the calculated k-factors are correct, it is possible to calculate C_{Al} from the C_{Ga}/C_{As} ratio calculated from I_{As} and I_{Ga} . The result from implementing this additional requirement in Cliff-Lorimer is seen in top of Fig. 6.1. The same calculations can also be made, but instead of using calculated k-factors, the experimentally determined ζ -factors from the ICD method can be used ($k_{AB} = \zeta_A/\zeta_B$). This results in concentration profile and maps seen in the middle of Fig. 6.1. As can be seen, the Al concentration using k-factors are closer to zero in the core, and around 20 at.% in the shell. It is known that the concentration in the shell is closer to 35 at.% [15], which is closer to the calculated shell concentration using ζ -factors. Even though the results are an improvement from the results in Fig. 4.13a and 4.13b, the assumption that the As composition is 50 at.% everywhere is an extremely crude first approximation, as it forces a certain result.

The second approach in post processing, is to assume that the Al stray contribution is constant within the entire mapped area. Subsequently, an average intensity of the Al stray can be found from the core. Then, this average stray Al intensity is subtracted everywhere in the map. This

results in the concentration profile and maps seen at the bottom in Fig. 6.1. As can be seen, the Al concentration in the core is indeed close to zero, but the shell concentration is too low, and the Ga and As concentrations are significantly overestimated and underestimated respectively. Subtracting an average Al stray intensity from the entire map is incorrect practice for mainly two reasons. First, the Al stray is predominantly created by $\text{Ga}_{K\alpha}$ and As_α strays generated within the sample, which means that the amount of Al strays is dependent on the number of Ga and As atoms present, which is not constant within the wire, especially in the shell where Al atoms replace Ga atoms. Secondly, as can be seen clearly in the Al and Ga concentration maps, the recorded X-ray intensity varies (in the y direction). This is because the absorption path length is higher at the top due to the position of the EDS detector relative to the cross section. Therefore, subtracting an average strays intensity is not a valid assumption even if the algorithms themselves look correct. Nevertheless, with all post-processing methods presented here, the Al rich bands in each corner of the cross-section as reported by Kauko [42] is observed, which shows some promise to the approaches.

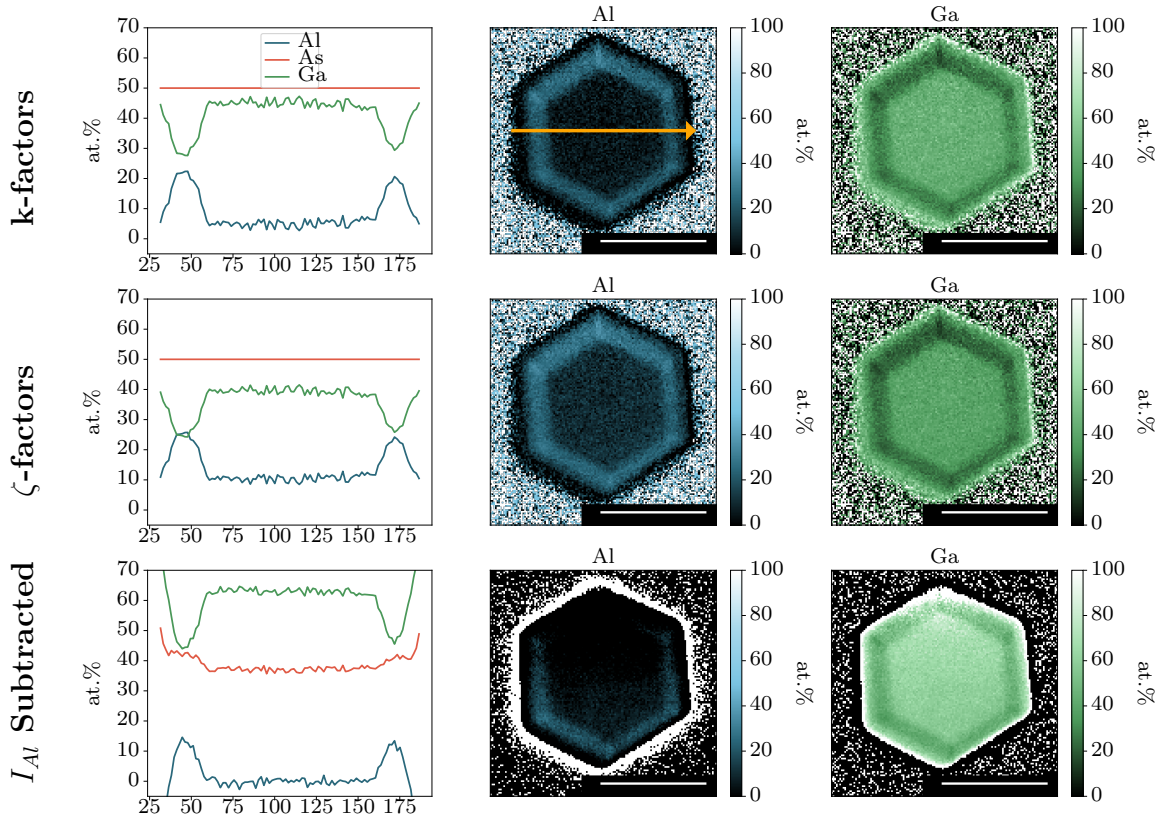


Figure 6.1: Quantitative analysis of radial core-shell GaAs/AlGaAs NWs for suggested post-processing routines to deal with Al stray. Concentration profiles across the orange arrow as well as concentration maps for Al and Ga are shown for three different approaches. Top row: Cliff-Lorimer with calculated k-factors assuming $C_{As} = 50$ at.%. Middle row: Cliff-Lorimer with k-factors calculated using ICD calculated ζ -factors for Ga and As and assuming $C_{As} = 50$ at.%. Bottom row: An average Al intensity, I_{Al} , from the Al free core is subtracted from the entire mapped area. All scale bars are 100 nm.

As discussed, there are some major obvious drawbacks to the post processing approaches to eliminate the Al stray presented here. However, it can be considered whether any of these methods can be combined with the ICD method by adding a second criteria to the algorithm, in combination with the flatness criteria. Alternatively, completely different concepts could be considered. For example, Jany et al. showed that unsupervised machine learning, also within HyperSpy, could distinguish signals of the same X-ray energy but from different volumes [83]. To conclude, the problem from stray radiation is real as it inhibits accurate quantification and needs to be addressed in future work.

7 | Conclusion

This work aims to improve quantitative EDS for technical important III-V semiconductors. This has been achieved through two main objectives: i) preliminary characterization of the used EDS detection systems and ii) implementation of the factorless ICD method for quantitative composition calculations. Three EDS detection systems have been used, namely the windowless Oxford Ultim Extreme 100 mm² in the LV Hitachi SU9000 S(T)EM and the Oxford X-Max 80 with ultra-thin window protection which was moved from the Jeol JEM2100 to the Jeol JEM2100F during the course of this work.

Characterizing the EDS detection systems was done with a standard NiO thin film on a Mo TEM grid test sample and a general Jupyter Notebook was developed to calculate all relevant detection characteristics. It was found that the energy resolution and energy channel sizes are ~ 130 eV and ~ 10 eV as the manufacturers state. Shadowing of the EDS detectors are observed in all instruments at tilt angles up to 10° - 15° and indicates that the detectors are not mounted correctly for optimal collection solid angle and high count rates. All instruments have internal fluorescence Si peak, and Fe strays from the column. Additional strays in the SU9000 are Cu, F, Au and especially Al, where the latter originates from the horseshoe clamp on the holder, which introduces several peaks in the low energy range of the spectra. High background levels and stray peaks in the low voltage range in the SU9000 due to large collection angle and windowless protection introduce challenges for high accuracy EDS quantification. However, this enables high count rates for low energy photons not possible in the X-Max 80 with a thin window.

As ratio-based approaches like Cliff-Lorimer require a sensitivity factor that can compromise the accuracy, the work implemented the recently developed ICD method for internal composition analysis of III-V ternary compounds, for the first time in LV STEM. The performance of the algorithm was mainly studied using a FIB lamella of a heterostructured GaAs_{1-x}Sb_x NW. A systematic study was performed at increasing tilt and voltages to investigate the stability of the method compared to the standard Cliff-Lorimer method. In both methods, the periodic Sb variations with a gradual increase to a maximum Sb within each SL are observed. The ICD algorithm corrects the over- and underestimation of Ga and As respectively observed with the Cliff-Lorimer method. Furthermore, the method provides calculated ζ -factors for all elements of interest which can be used to calculate new k-factors, in addition to relative thickness profiles that can be used to validate the quantification results, with minimal input from the user.

However, the Sb concentration profiles are currently more inconsistent using ICD than Cliff-Lorimer. It is thought that channeling effects, different absorption within the scanned area or high levels of noise are contributing factors. Noise is assumed to be the main cause, as the flatness of the benchmark element with constant composition is higher than expected, and reflects the noise in the data. The ICD algorithm works better based on improved reduction in flatness when PCA denoising is applied to the data. Although a more detailed study is required to determine how noise affects the ICD approach.

The Al stray identified in the SU9000 through NiO detection system characterization obstructs quantification of Al as it can be interpreted as a signal from the sample. In a core-shell $\text{Al}_x\text{Ga}_{1-x}\text{As}$ NW cross-section sample, this becomes obvious. A significant $\text{Al}_{K\alpha}$ signal from the Al-free core is detected, as the higher energy $\text{Ga}_{K\alpha}$ and $\text{As}_{K\alpha}$ photons hit the Al clamp in the holder and generate a detected Al signal. At 30 kV, this results in an Al composition of 95 at.% in the core using ICD, while at 5 kV, the $\text{Ga}_{K\alpha}$ and $\text{As}_{K\alpha}$ lines are not generated, and the quantification results are significantly improved. Nevertheless, both qualitative and quantitative EDS determination of Al in the SU9000 is limited due to the significant Al stray, and post-processing routines are attempted to extract a more accurate composition estimate for Al in the specimen.

Bibliography

- [1] D. Ren, L. Ahtapodov, J. S. Nilsen, J. Yang *et al.*, ‘Single-mode near-infrared lasing in a GaAsSb-based nanowire superlattice at room temperature’, *Nano letters*, vol. 18, pp. 2304–2310, 2018.
- [2] K. Tomioka, J. Motohisa, S. Hara, K. Hiruma *et al.*, ‘GaAs/AlGaAs core multishell nanowire-based light-emitting diodes on Si’, *Nano letters*, vol. 10, pp. 1639–1644, 2010.
- [3] J. A. Czaban, D. A. Thompson and R. R. LaPierre, ‘GaAs core-shell nanowires for photovoltaic applications’, *Nano letters*, vol. 9, pp. 148–154, 2009.
- [4] E. C. Garnett, M. L. Brongersma, Y. Cui and M. D. McGehee, ‘Nanowire solar cells’, *Annual review of materials research*, vol. 41, pp. 269–295, 2011.
- [5] A. M. Munshi, D. L. Dheeraj, V. T. Fauske, D.-C. Kim *et al.*, ‘Vertically aligned GaAs nanowires on graphite and few-layer graphene: Generic model and epitaxial growth’, *Nano letters*, vol. 12, pp. 4570–4576, 2012.
- [6] D. L. Dheeraj, G. Patriarche, H. Zhou, T. B. Hoang *et al.*, ‘Growth and characterization of wurtzite GaAs nanowires with defect-free zinc blende GaAsSb inserts’, *Nano letters*, vol. 8, pp. 4459–4463, 2008.
- [7] S. Plissard, K. Dick, X. Wallart and P. Caroff, ‘Gold-free GaAs/GaAsSb heterostructure nanowires grown on silicon’, *Applied Physics Letters*, vol. 96, p. 121 901, 2010.
- [8] X. Yan, W. Wei, F. Tang, X. Wang *et al.*, ‘Low-threshold room-temperature AlGaAs/GaAs nanowire/single-quantum-well heterostructure laser’, *Applied Physics Letters*, vol. 110, p. 061 104, 2017.
- [9] H. Zhou, T. B. Hoang, D. Dheeraj, A. Van Helvoort *et al.*, ‘Wurtzite GaAs/AlGaAs core-shell nanowires grown by molecular beam epitaxy’, *Nanotechnology*, vol. 20, p. 415 701, 2009.
- [10] G. Cliff and G. W. Lorimer, ‘The quantitative analysis of thin specimens’, *Journal of Microscopy*, vol. 103, pp. 203–207, 1975.
- [11] C. B. Carter and D. B. Williams, *Transmission electron microscopy: Diffraction, imaging, and spectrometry*. Springer, 2009.
- [12] T. Walther and X. Wang, ‘Self-consistent method for quantifying indium content from X-ray spectra of thick compound semiconductor specimens in a transmission electron microscope’, *Journal of Microscopy*, vol. 262, pp. 151–156, 2016.

-
- [13] A. Parisini, S. Frabboni, G. C. Gazzadi, R. Rosa *et al.*, ‘Comparison of Cliff–Lorimer-based methods of scanning transmission electron microscopy (STEM) quantitative X-ray microanalysis for application to silicon oxycarbides thin films’, *Microscopy and Microanalysis*, vol. 24, pp. 193–206, 2018.
- [14] M. Rathi, S. Ahrenkiel, J. Carapella and M. Wanlass, ‘A standards-based method for compositional analysis by energy dispersive X-ray spectrometry using multivariate statistical analysis: Application to multicomponent alloys’, *Microscopy and Microanalysis*, vol. 19, pp. 66–72, 2013.
- [15] J. S. Nilsen and A. T. van Helvoort, ‘Composition analysis by STEM-EDX of ternary semiconductors by internal references’, *Microscopy and Microanalysis*, vol. 28, pp. 61–69, 2021.
- [16] R. Egerton and S. Cheng, ‘Characterization of an analytical electron microscope with a NiO test specimen’, *Ultramicroscopy*, vol. 55, pp. 43–54, 1994.
- [17] M. S. Skomedal, ‘Correlated S(T)EM-TEM-EDX study of core-shell GaAs/AlGaAs nanowires’, Norwegian University of science and technology, report TFY4520, Department of Physics, 2021.
- [18] B. G. Streetman, S. Banerjee *et al.*, *Solid state electronic devices*. Pearson/Prentice Hall Upper Saddle River, NJ, 2006, vol. 10.
- [19] D. J. Griffiths, *Introduction to quantum mechanics*. Pearson International Edition (Pearson Prentice Hall, Upper Saddle River, 2005), 1960.
- [20] A. Casadei, E. F. Pecora, J. Trevino, C. Forestiere *et al.*, ‘Photonic–plasmonic coupling of GaAs single nanowires to optical nanoantennas’, *Nano letters*, vol. 14, pp. 2271–2278, 2014.
- [21] I. Andersen, ‘TEM characterization of GaAs/GaAsSb heterostructured nanowires for laser applications’, M.S. thesis, NTNU, Fakultet for naturvitenskap, 2017.
- [22] D. Kleppner, ‘Rereading Einstein on radiation’, *Revista Brasileira de Ensino de Física*, vol. 27, pp. 87–91, 2005.
- [23] S. W. Eaton, A. Fu, A. B. Wong, C.-Z. Ning *et al.*, ‘Semiconductor nanowire lasers’, *Nature reviews materials*, vol. 1, pp. 1–11, 2016.
- [24] D. Dheeraj, A. Munshi, M. Scheffler, A. Van Helvoort *et al.*, ‘Controlling crystal phases in GaAs nanowires grown by Au-assisted molecular beam epitaxy’, *Nanotechnology*, vol. 24, p. 015 601, 2012.
- [25] C.-C. Chang, C.-Y. Chi, M. Yao, N. Huang *et al.*, ‘Electrical and optical characterization of surface passivation in GaAs nanowires’, *Nano letters*, vol. 12, pp. 4484–4489, 2012.
- [26] G. Cao, *Nanostructures & nanomaterials: synthesis, properties & applications*. Imperial college press, 2004.
-

-
- [27] F. De La Peña, E. Prestat, V. T. Fauske, P. Burdet *et al.*, *Hyperspy/hyperspy: Release v1.6.5*, 2021. DOI: 10.5281/ZENODO.5608741. [Online]. Available: <https://zenodo.org/record/5608741>.
- [28] M. Inokuti, ‘Inelastic collisions of fast charged particles with atoms and molecules—the bethe theory revisited’, *Reviews of modern physics*, vol. 43, p. 297, 1971.
- [29] C. T. Chantler, ‘Detailed tabulation of atomic form factors, photoelectric absorption and scattering cross section, and mass attenuation coefficients in the vicinity of absorption edges in the soft X-ray ($Z= 30-36$, $Z= 60-89$, $E= 0.1 \text{ keV}-10 \text{ keV}$), addressing convergence issues of earlier work’, 2005.
- [30] M. Watanabe, ‘Practical aspects and advanced applications of XEDS’, in *Transmission Electron Microscopy*, Springer, 2016, pp. 467–503.
- [31] R. Castaing, ‘Application des sondes électroniques a une méthode d’analyse ponctuelle chimique et cristallographique’, Ph.D. dissertation, Université de Paris, 1952.
- [32] M. Watanabe and D. Williams, ‘The quantitative analysis of thin specimens: A review of progress from the Cliff-Lorimer to the new ζ -factor methods’, *Journal of microscopy*, vol. 221, pp. 89–109, 2006.
- [33] Ted Pella Inc., *Evaluating an analytical TEM with the NIOXTM test specimen*, https://www.tedpella.com/technote_html/650%20TN.pdf, Accessed:2022-01.
- [34] J. Bennett and R. Egerton, ‘NiO test specimens for analytical electron microscopy: Round-robin results’, *Microsc Microanal*, vol. 1, pp. 143–150, 1995.
- [35] C. Fiori, C. Swyt and J. Ellis, ‘The theoretical characteristic to continuum ratio in energy dispersive analysis in the analytical electron microscope’, *Microbeam Analysis*, vol. 1982, pp. 57–71, 1982.
- [36] C. Kittel, P. McEuen and P. McEuen, *Introduction to solid state physics*. Wiley New York, 1996, vol. 8.
- [37] K. Momma and F. Izumi, ‘VESTA: A three-dimensional visualization system for electronic and structural analysis’, *Journal of Applied crystallography*, vol. 41, pp. 653–658, 2008.
- [38] J. Todorovic, ‘Correlated transmission electron microscopy and micro-photoluminescence studies of GaAs-based heterostructured semiconductor nanowires’, Ph.D. dissertation, NTNU, Fakultet for naturvitenskap, 2012.
- [39] J. I. Goldstein, D. E. Newbury, J. R. Michael, N. W. Ritchie *et al.*, *Scanning electron microscopy and X-ray microanalysis*. Springer, 2017.
- [40] B. Fultz and J. M. Howe, *Transmission electron microscopy and diffractometry of materials*. Springer Science & Business Media, 2012.

-
- [41] A. M. Munshi, D. L. Dheeraj, J. Todorovic, A. T. van Helvoort *et al.*, ‘Crystal phase engineering in self-catalyzed GaAs and GaAs/GaAsSb nanowires grown on Si (111)’, *Journal of Crystal Growth*, vol. 372, pp. 163–169, 2013.
- [42] H. Kauko, C. Zheng, Y. Zhu, S. Glanvill *et al.*, ‘Compositional analysis of GaAs/AlGaAs heterostructures using quantitative scanning transmission electron microscopy’, *Applied Physics Letters*, vol. 103, p. 232111, 2013.
- [43] D. M. Lundeby, ‘Improving the accuracy of TEM-EDX quantification by implementing the zeta-factor method’, M.S. thesis, NTNU, Fakultet for naturvitenskap, 2019.
- [44] I.-E. Nylund, ‘Evaluation of energy-dispersive spectroscopy characteristics for improved compositional analysis’, Norwegian University of science and technology, 2017.
- [45] J. S. Nilsen, *Quantitative-EDX of ternary semiconductors using internal references: Tutorial and example data-set*, 2019. DOI: 10.5281/zenodo.3569466.
- [46] T. Plamann and M. Hytch, ‘Tests on the validity of the atomic column approximation for STEM probe propagation’, *Ultramicroscopy*, vol. 78, pp. 153–161, 1999.
- [47] V. Morandi and P. G. Merli, ‘Contrast and resolution versus specimen thickness in low energy scanning transmission electron microscopy’, *Journal of Applied Physics*, vol. 101, p. 114917, 2007.
- [48] S. Hillyard, R. F. Loane and J. Silcox, ‘Annular dark-field imaging: Resolution and thickness effects’, *Ultramicroscopy*, vol. 49, pp. 14–25, 1993.
- [49] M. Watanabe and C. Wade, ‘Practical measurement of X-ray detection performance of a large solid-angle silicon drift detector in an aberration-corrected STEM’, *Microscopy and Microanalysis*, vol. 19, pp. 1264–1265, 2013.
- [50] I. Bækken, ‘Characterizing the structural and optical properties of AlGaN nanostructures for ultraviolet LED applications using correlated electron microscopy’, M.S. thesis, NTNU, Fakultet for naturvitenskap, 2021.
- [51] S. M. Zemyan and D. Williams, ‘Standard performance criteria for analytical electron microscopy’, *Journal of Microscopy*, vol. 174, pp. 1–14, 1994.
- [52] C. Gray, J. Chapman, W. Nicholson, B. Robertson *et al.*, ‘X-ray production in thin films by electrons with energies between 40 and 100 keV. 2—characteristic cross-sections and the overall X-ray spectrum’, *X-ray Spectrometry*, vol. 12, pp. 163–169, 1983.
- [53] H. Kauko, B. Fimland, T. Grieb, A. Munshi *et al.*, ‘Near-surface depletion of antimony during the growth of GaAsSb and GaAs/GaAsSb nanowires’, *Journal of Applied Physics*, vol. 116, p. 144303, 2014.
- [54] M. Schaffer, B. Schaffer and Q. Ramasse, ‘Sample preparation for atomic-resolution STEM at low voltages by FIB’, *Ultramicroscopy*, vol. 114, pp. 62–71, 2012.
-

-
- [55] D. O. Klenov and S. Stemmer, ‘Contributions to the contrast in experimental high-angle annular dark-field images’, *Ultramicroscopy*, vol. 106, pp. 889–901, 2006.
- [56] J. Todorovic, H. Kauko, L. Ahtapodov, A. Moses *et al.*, ‘The effects of Sb concentration variation on the optical properties of GaAsSb/GaAs heterostructured nanowires’, *Semiconductor science and technology*, vol. 28, p. 115 004, 2013.
- [57] D. Ren, D. L. Dheeraj, C. Jin, J. S. Nilsen *et al.*, ‘New insights into the origins of Sb-induced effects on self-catalyzed GaAsSb nanowire arrays’, *Nano letters*, vol. 16, pp. 1201–1209, 2016.
- [58] S. Johnson, C. Guo, S. Chaparro, Y. G. Sadofyev *et al.*, ‘GaAsSb/GaAs band alignment evaluation for long-wave photonic applications’, *Journal of crystal growth*, vol. 251, pp. 521–525, 2003.
- [59] A. Garmannslund, ‘Refinement of the ζ -factor method for quantitative energy-dispersive X-ray spectroscopy in scanning transmission electron microscopy’, M.S. thesis, NTNU, 2016.
- [60] O. Eibl, ‘New method for absorption correction in high-accuracy, quantitative EDX microanalysis in the TEM including low-energy x-ray lines’, *Ultramicroscopy*, vol. 50, pp. 179–188, 1993.
- [61] G. Bastin and H. Heijligers, ‘Quantitative electron probe microanalysis of ultra-light elements (boron-oxygen)’, in *Electron probe quantitation*, Springer, 1991, pp. 145–161.
- [62] R. Gauvin and G. L’Espérance, ‘Determination of the Cnl parameter in the Bethe formula for the ionization cross-section by the use of Cliff-Lorimer KAB factors obtained at different accelerating voltages in a TEM’, *Journal of Microscopy*, vol. 163, pp. 295–306, 1991.
- [63] J. Wood, D. Williams and J. Goldstein, ‘Experimental and theoretical determination of kAF_e factors for quantitative X-ray microanalysis in the analytical electron microscope’, *Journal of Microscopy*, vol. 133, pp. 255–274, 1984.
- [64] R. Graham and J. Steeds, ‘Determination of Cliff-Lorimer k factors by analysis of crystallized microdroplets’, *Journal of Microscopy*, vol. 133, pp. 275–280, 1984.
- [65] P. J. Sheridan, ‘Determination of experimental and theoretical kASi factors for a 200-kV analytical electron microscope’, *Journal of electron microscopy technique*, vol. 11, pp. 41–61, 1989.
- [66] J. H. Spence and J. Taftø, ‘ALCHEMI: A new technique for locating atoms in small crystals’, *Journal of Microscopy*, vol. 130, pp. 147–154, 1983.
- [67] I. Jones, ‘Determining the locations of chemical species in ordered compounds: ALCHEMI’, in *Advances in imaging and electron physics*, vol. 125, Elsevier, 2003, pp. 63–I.
- [68] M. De Graef, *Introduction to conventional transmission electron microscopy*. Cambridge university press, 2003.

-
- [69] H. Lakner, B. Bollig, S. Ungerechts and E. Kubalek, ‘Characterization of III-V semiconductor interfaces by Z-contrast imaging, EELS and CBED’, *Journal of Physics D: Applied Physics*, vol. 29, p. 1767, 1996.
- [70] B. Yacobi and D. Holt, ‘Cathodoluminescence scanning electron microscopy of semiconductors’, *Journal of applied physics*, vol. 59, R1–R24, 1986.
- [71] I. T. Jolliffe, *Principal component analysis for special types of data*. Springer, 2002.
- [72] I. T. Jolliffe and J. Cadima, ‘Principal component analysis: A review and recent developments’, *Philosophical Transactions of the Royal Society A: Mathematical, Physical and Engineering Sciences*, vol. 374, p. 20150202, 2016.
- [73] M. Moreira, M. Hillenkamp, G. Divitini, L. H. Tizei *et al.*, ‘Improving quantitative EDS chemical analysis of alloy nanoparticles by PCA denoising: Part I, reducing reconstruction bias’, *Microscopy and Microanalysis*, vol. 28, pp. 338–349, 2022.
- [74] D. E. Newbury and N. W. Ritchie, ‘Electron-excited X-ray microanalysis at low beam energy: Almost always an adventure!’, *Microscopy and Microanalysis*, vol. 22, pp. 735–753, 2016.
- [75] J. Liu, ‘High-resolution and low-voltage FE-SEM imaging and microanalysis in materials characterization’, *Materials characterization*, vol. 44, pp. 353–363, 2000.
- [76] R. Wuhrer and K. Moran, ‘Low voltage imaging and X-ray microanalysis in the SEM: Challenges and opportunities’, in *IOP Conference Series: Materials Science and Engineering*, IOP Publishing, vol. 109, 2016, p. 012019.
- [77] S. Burgess, J. Sagar, J. Holland, X. Li *et al.*, ‘Ultra-low kV EDS—a new approach to improved spatial resolution, surface sensitivity, and light element compositional imaging and analysis in the SEM’, *Microscopy Today*, vol. 25, pp. 20–29, 2017.
- [78] R. Gauvin, ‘What remains to be done to allow quantitative X-ray microanalysis performed with EDS to become a true characterization technique?’, *Microscopy and Microanalysis*, vol. 18, pp. 915–940, 2012.
- [79] R. Keller, ‘STEM-in-SEM: A re-emerging material measurement approach’, *Microscopy and Microanalysis*, vol. 27, pp. 1050–1051, 2021.
- [80] N. Faber, M. Meinders, P. Geladi, M. Sjöström *et al.*, ‘Random error bias in principal component analysis. part i. derivation of theoretical predictions’, *Analytica chimica acta*, vol. 304, pp. 257–271, 1995.
- [81] E. R. Malinowski and D. G. Howery, *Factor analysis in chemistry*. Wiley New York, 1980, vol. 3.
- [82] D. Jannis, K. Müller-Caspary, A. Béché and J. Verbeeck, ‘Coincidence detection of EELS and EDX spectral events in the electron microscope’, *Applied Sciences*, vol. 11, p. 9058, 2021.

-
- [83] B. Jany, A. Janas and F. Krok, ‘Retrieving the quantitative chemical information at nanoscale from scanning electron microscope energy dispersive X-ray measurements by machine learning’, *Nano letters*, vol. 17, pp. 6520–6525, 2017.

A | Appendix

A.1 Jupyter Notebooks for detector characterization

This appendix includes the code developed for characterization of the EDS system with the NiO thin film of Mo TEM grid standard sample. First, the notebook containing the function `DetectorCharacterize` is shown. This has been a further development and generalization of the code written by I.-E. Nylund [44] in a previous project. Additionally, the function has been made to handle exceptions if X-ray lines are not within the energy range (e.g. if the acceleration voltage is lower than 17 kV and the $\text{Mo}_{K\alpha}$ peak is not excited). The function takes a spectrum from the NiO test sample on Mo grid [33], and calculates and returns all relevant parameters to this project in a list. The list contains the deviation of the peak position of $\text{O}_{K\alpha}$, $\text{Ni}_{K\alpha}$ and $\text{Mo}_{K\alpha}$ to the theoretical values, which can be used for energy scale calibration (see example code). Then, the total intensity of the $\text{O}_{K\alpha}$ and $\text{Ni}_{K\alpha}$ peak is returned, which can be used to find shadowing of the detector. Lastly the list includes all relevant intensity ratios between X-rays and the peak to back round ratio of $\text{Ni}_{K\alpha}$ peak.

Note that the function uses model fitting in order to extract peak intensities, and the code therefore has to be used with caution. To ensure a good model fitting, all the peaks has to be defined in the spectrum before the `DetectorCharacterize` function is used. Additionally, most Oxford detectors have a zero peak. This is handled by the function automatically. If the spectrum does not have a zero peak, this has to be defined by setting `zero_peak = False`. In order to verify the modelled spectrum, the function returns the model such that the user can evaluate its quality.

Below the characterization notebook, an example is provided on how to use the code. This is done using the data from the NiO on Mo grid sample taken at 30 kV and 0° tilt in the SU9000, presented in this work. The code should be applicable to all HT ranges.

EDS detector characterization notebook

Load necessary libraries

```
[ ]: %matplotlib qt
import numpy as np
import matplotlib.pyplot as plt
import hyperspy.api as hs
import math
```

The function below called DetectorCharacterize, takes in a spectrum and returns a list with the parameters of interest for this work.

Whether or not the spectrum has a zero-peak needs to be defined in the function. (Oxford detectors usually have zero-peak)

The function also has the option to plot the NiKa window used, and also to plot, i.e. print the results

The function handles exceptions if certain X-ray lines are not within the range. This is for example for the MoKa line if the acceleration voltage is below 17 kV. The ratios using MoKa are set to 'nan'.

Be careful to define all X-ray lines present in the spectrum before using the DetectorCharacterize function, as it uses model fitting to extract peak intensities.

```
[ ]: def DetectorCharacterize(s, zero_peak = True, plot_NiKa_window = True,
    →plot_results = True):
    s.add_elements(["Ni", "Mo", "O"])

    Vacc = s.metadata.Acquisition_instrument.TEM.beam_energy

    offset = s.axes_manager[0].offset
    scale = s.axes_manager[0].scale

    start_index = abs(int(offset/scale))
    s_0 = s.isig[start_index:]

    ##### Energy scale calibration #####
    ##### MoKa #####
    #Interval to look for MoKa
    x_MoKa_0 = int(17/scale)
    x_MoKa_1 = int(18/scale)

    MoKa_window = s_0.data[x_MoKa_0:x_MoKa_1]

    #Find local position and value of MoKa X-ray
    MoKa_max_local_index = np.argmax(MoKa_window)
    MoKa_max = MoKa_window[MoKa_max_local_index]
```

```

#Find global position and energy value
MoKa_max_global_index = MoKa_max_local_index + x_MoKa_0
MoKa_max_E = MoKa_max_global_index * scale

#find deviation from theory
MoKa_Theory = hs.material.elements.Mo.Atomic_properties.Xray_lines.Ka.
↪energy_keV #Xray data booklet
devMoKa = (MoKa_max_E - MoKa_Theory)*1000

##### NiKa #####
x_NiKa_0 = int(7/scale)
x_NiKa_1 = int(7.8/scale)

NiKa_window = s_0.data[x_NiKa_0:x_NiKa_1]
NiKa_max_local_index = np.argmax(NiKa_window)
NiKa_max = NiKa_window[NiKa_max_local_index]
NiKa_max_global_index = NiKa_max_local_index + x_NiKa_0
NiKa_max_E = NiKa_max_global_index * scale
NiKa_Theory = hs.material.elements.Ni.Atomic_properties.Xray_lines.Ka.
↪energy_keV
devNiKa = (NiKa_max_E - NiKa_Theory)*1000

##### OKa #####
x_OKa_0 = int(0.4/scale)
x_OKa_1 = int(0.6/scale)

OKa_window = s_0.data[x_OKa_0:x_OKa_1]
OKa_max_local_index = np.argmax(OKa_window)
OKa_max = OKa_window[OKa_max_local_index]
OKa_max_global_index = OKa_max_local_index + x_OKa_0
OKa_max_E = OKa_max_global_index * scale
OKa_Theory = hs.material.elements.O.Atomic_properties.Xray_lines.Ka.
↪energy_keV
devOKa = (OKa_max_E - OKa_Theory)*1000

theoretical_values = [OKa_Theory, NiKa_Theory, MoKa_Theory]
measured_values = [OKa_max_E, NiKa_max_E, MoKa_max_E]
deviation = [devOKa, devNiKa, devMoKa]
max_intensities = [OKa_max, NiKa_max, MoKa_max]

##### peak shape and fwhm

```

```

NiKa_window = s_0.isig[x_NiKa_0:x_NiKa_1]

if plot_NiKa_window:
    NiKa_window.plot()

FWHM_Ni = NiKa_window.estimate_peak_width(factor=0.5)
FWHM_Mn = FWHM_Ni*0.926
FWTM_Ni = NiKa_window.estimate_peak_width(factor=0.1)

FWHM = FWHM_Mn.data[0]
FWTM_FWHM = FWTM_Ni.data[0] / FWHM_Ni.data[0]

##### creating a model
if Vacc < 20:
    s = s.isig[:Vacc]

if zero_peak == True:
    s_cut = s.isig[33:]
    m = s_cut.create_model(auto_background = False)
else:
    m = s.create_model(auto_background = False)

m.add_polynomial_background(order=8)
m.fit_background()
m.fit(bounded=True)

##### intensity ratios:
try:
    MoKa = m.components.Mo_Ka.A.value

except AttributeError:
    print('Attribute Error: \'ModelComponents\' object has no attribute_
↪\'Mo_Ka\'. I(MoKa) set to \'nan\'')
    MoKa = float('nan')

try:
    NiKa = m.components.Ni_Ka.A.value

except AttributeError:
    print('Attribute Error: \'ModelComponents\' object has no attribute_
↪\'Ni_Ka\'. I(NiKa) set to \'nan\'')
    NiKa = float('nan')

```

```

if math.isnan(NiKa):
    MoLa = m.components.Mo_La.A.value
    OKa = m.components.O_Ka.A.value
    NiKb = float('nan')

    OKa_I = OKa
    NiKa_I = NiKa

    rNiMo = float('nan')
    rMoKL = float('nan')
    rNiKaKb = float('nan')

    PB_F = float('nan')

elif math.isnan(MoKa) and not math.isnan(NiKa):
    MoLa = m.components.Mo_La.A.value
    OKa = m.components.O_Ka.A.value
    NiKb = m.components.Ni_Kb.A.value

    OKa_I = OKa
    NiKa_I = NiKa

    rNiMo = float('nan')
    rMoKL = float('nan')
    rNiKaKb = NiKa/NiKb

    ##### background ratio, Total P/B (for NiKa peak)
    NiKaBG = m.as_signal(component_list=["background_order_8"])
    NiKaRange = (7.16, 7.76)
    cf = (NiKaRange[1]-NiKaRange[0])/scale
    roi = hs.roi.SpanROI(7.16, 7.76)
    B = roi(NiKaBG)
    PB = NiKa/B.integrate1D(-1).data[0]
    PB_F = cf * PB

elif not math.isnan(MoKa) and not math.isnan(NiKa):

    MoLa = m.components.Mo_La.A.value
    OKa = m.components.O_Ka.A.value
    NiKb = m.components.Ni_Kb.A.value

    OKa_I = OKa
    NiKa_I = NiKa

    rNiMo = NiKa/MoKa

```



```

rMoKL = MoKa/MoLa

rNiKaKb = NiKa/NiKb

NiKaBG = m.as_signal(component_list=["background_order_8"])
NiKaRange = (7.16, 7.76)
cf = (NiKaRange[1]-NiKaRange[0])/scale
roi = hs.roi.SpanROI(7.16, 7.76)
B = roi(NiKaBG)
PB = NiKa/B.integrate1D(-1).data[0]
PB_F = cf * PB

parameter_list = [devOKa, devNiKa, devMoKa, FWHM, FWTM_FWHM, OKa_I, NiKa_I,
↪rNiMo, rMoKL, PB_F, rNiKaKb]
parameter_list_name = ["\u0394OKa [eV]", "\u0394NiKa [eV]", "\u0394MoKa [
↪eV]", "FWHM", "FWTM/FWHM", "I(O_Ka) [a.u]", "I(Ni_Ka) [a.u]", "I(Ni_Ka)/
↪I(Mo_Ka)", "I(Mo_Ka)/I(Mo_La)", "I(Ni_Ka)/B(Ni_Ka)", "I(Ni_Ka)/I(Ni_Kb)"]

if plot_results:
    print("Calibration results for spectrum with title \"", s.metadata.
↪General.title, "\"")
    print("Theoretical values used during calibration: OKa = 0.5249, NiKa =
↪7.4781, MoKa = 17.4793")
    for i in range(len(parameter_list)):
        string = parameter_list_name[i] + ":"
        print( "{0:<18}".format(string), "{0:>15}".
↪format(round(parameter_list[i],5)))

return m, parameter_list

```

Calibration example notebook

```
[1]: %matplotlib qt
import hyperspy.api as hs
import numpy as np
import matplotlib.pyplot as plt
import import_ipynb
import DetectorCharacterize_v4 as dc #import claibration notebook
```

importing Jupyter notebook from DetectorCharacterize_v4.ipynb

```
[2]: s_3_SU9000 = hs.load("C://Users//mari//OneDrive - NTNU//V2022//TFY4905_
↳Nanoteknologi, masteroppgave//Data//03.23.22_NiOMo_calibration_SU9000//EDS//
↳Point analysis//Spectrum 3.emsa", signal_type = "EDS_TEM")
```

```
[3]: elements_SU9000 = ["Ni", "O", "Mo", "Si", "C", "Cu", "F", "Al", "Fe", "Au"]
s_3_SU9000.add_elements(elements_SU9000)
```

Calibration for only 0 tilt

```
[5]: m_SU9000, parameters_SU9000 = dc.DetectorCharacterize(s_3_SU9000)
```

Calibration results for spectrum with title " Spectrum 3 "

Theoretical values used during calibration: OKa = 0.5249, NiKa = 7.4781, MoKa = 17.4793

Δ OKa [eV]:	-4.9
Δ NiKa [eV]:	-8.1
Δ MoKa [eV]:	-59.3
FWHM:	0.13132
FWM/FWHM:	1.87346
I(O_Ka) [a.u]:	214196.34647
I(Ni_Ka) [a.u]:	339874.0157
I(Ni_Ka)/I(Mo_Ka):	94.56526
I(Mo_Ka)/I(Mo_La):	0.06964
I(Ni_Ka)/B(Ni_Ka):	889.36761
I(Ni_Ka)/I(Ni_Kb):	7.83085

Find energy scale

```
[6]: Theoretical_value = np.array([0.5249, 7.4782, 17.4793])
deviation_SU9000 = np.array([dev for dev in parameters_SU9000[:3]])
a_SU9000, b_SU9000 = np.polyfit(Theoretical_value, deviation_SU9000, 1)
scale_SU9000 = s_3_SU9000.axes_manager[0].scale
True_scale_SU9000 = round(scale_SU9000 - a_SU9000/1000*scale_SU9000, 6)
print("True scale SU9000: " + str(True_scale_SU9000))
```

True scale SU9000: 0.010033

```
[ ]:
```

A.2 Jupyter Notebook for initial inspection and editing of EDS map data

Below is a notebook that was used for preliminary inspection and editing of the EDS maps. The notebook is a collection of some of the most useful operations. This includes plotting the elemental maps, changing the axis unit, rotating the map, creating a new region of interest (ROI) and binning the map to a minimum required spatial resolution. Added to this notebook is also how to re-calibrate to the correct energy resolution and channel size in the metadata. Lastly, the new and corrected map is saved as a new .hdf5 file.

Notebook for initial inspection and editing of EDS maps

Import necessary libraries and the EDS map

```
[ ]: %matplotlib qt
import numpy as np
import hyperspy.api as hs
import matplotlib.pyplot as plt
```

```
[ ]: filepath = "C://Users//mari//OneDrive - NTNU//V2022//TFY4905 Nanoteknologi,
↳masteroppgave//Data//29.03.22_SC45GaASSb_GaAs//29.03.2022//Project 1//maps2//
↳SL4.hdf5"
s = hs.load(filepath)
```

Start by defining elements and X-ray lines in the sample and plot initial spectrum as well as individual maps of each X-ray lines.

```
[ ]: elements = ["Sb", "As", "Ga"]
lines = ['Sb_La', 'As_Ka', 'Ga_Ka']

s.set_elements(elements)
s.set_lines(lines)
```

```
[ ]: s.sum().plot(True)
intensities = s.get_lines_intensity()#plot_result=True)
hs.plot.plot_images(intensities, axes_decor='off', scalebar='all')
```

Check axes to ensure same unit for x and y axis

If it is not the same, then plotting the maps wont work correctly.

```
[ ]: s.axes_manager
```

Change y-axis to nm unit

```
[ ]: s.axes_manager[1].scale = s.axes_manager[1].scale * 1000
s.axes_manager[1].units = "nm"
s.axes_manager
```

Rotate the map 90 degrees

```
[ ]: s = s.transpose(navigation_axes=[1,0])
s.axes_manager[0].name = "x"
s.axes_manager[1].name = "y"
s.axes_manager
```

```
[ ]: s.metadata.Acquisition_instrument.TEM.Detector.EDS.energy_resolution_MnKa
```

Changing to true energy scale and energy resolution based on detector characterization

```
[ ]: E_scale_2100 = 0.01003
E_scale_SU9000 = 0.01003

s.axes_manager[2].scale = E_scale_2100 #Choose correct value for instrument

E_res_2100 = 133
E_res_SU9000 = 132

s.metadata.Acquisition_instrument.TEM.Detector.EDS.energy_resolution_MnKa = 
↳E_res_2100 #Choose correct value for instrument
```

By creating a ROI, the map can be cropped to the desired dimensions

```
[ ]: l = 90
r = 110
t = 27
b = 190

roi = hs.roi.RectangularROI(left = l, right = r, top = t, bottom = b)
sr = roi(s)
s.plot()
roi2D = roi.interactive(s, color = "blue")
```

```
[ ]: s = sr
```

Rebin the map to correct scale

Here, the rebinning is set such that the final map has the highest a pixel size without exceeding the minimum spatial resolution required of 6 nm.

```
[ ]: scale = s.axes_manager[0].scale
minimum_spatial_res = 6
rebin_scale = minimum_spatial_res // scale
s = s.rebin(scale = [rebin_scale, rebin_scale, 1])
```

Save the new edited map at the desired path

```
[ ]: filepath_new = "C://Users//mari//OneDrive - NTNU//V2022//TFY4905 Nanoteknologi, 
↳masteroppgave//Data//29.03.22_SC45GaASSb_GaAs//29.03.2022//Project 1//maps2//
↳SL4_corr.hdf5"
```

```
[ ]: s.save(filepath_new)
```

```
[ ]:
```

A.3 Jupyter notebook for Internal Composition Determination

In this appendix, the code used for ICD analysis of the EDS datasets are shown. The notebook includes the original code by J. Nilsen. The code has been modified for this specific work. Specifically, a function ICD has been written that determines which X-ray lines to use depending on the acceleration voltage and takes the reference area to be used in as a parameter. The notebook also calculates the Cliff-Lorimer concentrations for comparison and plots the profiles for visualization. Additionally, the code retrieves all relevant parameters and saves to a .csv file which comes into handy when several datasets are processed.

The dataset used in this example is of the axially heterostructured GaAsSb NW FIB sample (thickness ~ 100 nm) taken in the Hitachi SU9000 STEM at 30 kV and 8° tilt.

```
[1]: %matplotlib qt
import hyperspy.api as hs
import numpy as np
import matplotlib.pyplot as plt
from hyperspy import utils
import pandas as pd
```

```
[2]: plt.rcParams['svg.fonttype'] = 'none'
```

Load datasets

```
[3]: s_9000_30kV_8tilt_0 = hs.load("C://Users//mari//OneDrive - NTNU//V2022//TFY4905_
↳Nanoteknologi, masteroppgave//Data//04.05.2022_SCN45_SU9000//SL6_x8//
↳SL63008_corr.hdf5", signal_type = "EDS_TEM")
spectra_name = "30kV 8 tilt"
```

Define k-vector to be used in Cliff-Lorimer

```
[4]: #k_vector = {Vacc: [k_As, k_Ga, k_Sb],
#           ...
#           }

k_vector = {5: [1.183, 1.046, 9.234], #L lines fro As and Ga
            10: [1.281, 1.178, 3.280], #L lines for As and Ga
            15: [13.732, 7.534, 2.742], #K lines for As and Ga
            30: [4.618, 3.484, 2.307], #K lines for As and Ga
            200: [1.502, 1.346, 1.948]} #K lines for As and Ga
```

Code developed by J. Nilsen

```
[5]: def determine_zeta_factor(intensities, composition, dose, mass_thickness):
    """
    Determine zeta-factors from the reference area.

    Parameters
    -----
    intensities: numpy.array
        The intensities for each X-ray line in the reference. The first axis
    ↳should be the element axis.
    composition: list of float
        Composition of the elements given in wt.% in the same order as
    ↳intensities.
    dose: float
```

Total electron dose given by $i*t*N$, where i is the beam_current, t is
→the acquisition time,
and N the number of electrons per unit electric charge ($1/e$).

Returns:

The zeta factors of the reference area.

"""

```
zfactores = np.zeros_like(intensities, dtype='float')
```

```
for i, (intensity, comp) in enumerate(zip(intensities, composition)):  
    zfactores[i] = (dose * mass_thickness * comp) / intensity
```

```
return zfactores
```

```
def calculate_unknown_zeta(elements, zfactores, intensities, const_el):
```

```
'''
```

Calculates the unknown zeta factor in a system where the other zeta factors
→are known, and one of the
elements is known to be constant with respect to the concentration of the
→element with unknown zeta
factor. A good example is ternary heterostructured semiconductors where one
→of the elements is known
to be 50 at.% independently of the other two elements.

Parameters:

elements: list

The elements present in the sample, in the same order as intensities
→(alphabetical).

zfactores: list of ints

The zeta factors of the system. The unknown zeta factor is set to 0,
→same order as intensities.

intensities: numpy.array

The intensities for each X-ray line. The first axis should be the
→element axis.

const_el: str

The element with the constant concentration.

Returns:

The unknown zeta factor of the element that gives the most constant
→concentration of the element that
is known to have a constant concentration.

```
'''
```



```

unknown_zeta = zfactors.index(0)
constant_element = elements.index(const_el)
flatness = 0

while(True):

    zI = []
    for i in range(len(zfactors)):
        zI.append(zfactors[i]*intensities[i].data)

    comp_wt = []
    for i in range(len(zfactors)):
        comp_wt.append(zI[i]/sum(zI))

    comp_at = hs.material.weight_to_atomic([comp_wt[0], comp_wt[1],
→comp_wt[2]], (elements))/100
    if flatness == 0 and zfactors[unknown_zeta] == 0:
        print("Initial flatness: ", np.max(comp_at[constant_element])-np.
→min(comp_at[constant_element]))
        if (np.max(comp_at[constant_element])-np.min(comp_at[constant_element]))
→< flatness:
            print("The zeta factor for " + elements[unknown_zeta] + " was
→determined to be " +
                str(zfactors[unknown_zeta]) + " with a flatness criterion of "
                + str(round(flatness*100,2)) + " at.%.")
            break
        elif zfactors[unknown_zeta] > (10*(zfactors[constant_element])):
            flatness += 0.001
            zfactors[unknown_zeta] = 0

    zfactors[unknown_zeta] += zfactors[constant_element]/1000

return zfactors[unknown_zeta], flatness

def find_zeta_from_reference(r, intensities_ref, acquisition_time,
→probe_current, thickness, density_ref,
                            composition_ref, width, length):
    """
    Finds the zeta factors of the reference area.
    Parameters:
    -----
    r: The EDX signal of the reference area.
    intensities_ref: numpy.array
        The intensities for each X-ray line in the reference. The first axis
→should be the element axis.

```

```

acquisition_time: float
    The dwell time of each pixel (can be arbitrary)
probe_current: float
    The probe current during the acquisition (can be arbitrary)
thickness: float
    The specimen thickness of the reference area in nm (can be arbitrary)
density_ref: float
    The density of the reference area.
composition_ref: list of float
    Composition of the elements in the reference given in wt.% in the same
    ↪ order as intensities.

Returns:
    -----
    The zeta factors of the reference area.
    '''

    r.set_microscope_parameters(live_time = acquisition_time*width*length,
    ↪ beam_current=probe_current)
    intensities_ref = utils.stack(intensities_ref)
    zeta_factors = determine_zeta_factor(intensities_ref,
                                       composition_ref,
                                       r._get_dose("zeta"),
                                       thickness*1e-9*density_ref)

    return zeta_factors

def find_unknown_zeta(intensities, elements, constant_el, known_zeta, lines_ref,
    ↪ lines, constant_element):
    '''
    Calculates the unknown zeta factor based on the zeta factors found in the
    ↪ reference area and that one
    element has constant composition.
    Parameters:
    -----
    intensities: numpy.array
    The intensities of each X-ray line in the area of interest. The first
    ↪ axis should be the element axis.
    elements: list of str
    The elements to be quantified in the area of interest, in the same order
    ↪ as intensities.
    known_zeta: list of float
    The zeta factors found from the reference area.
    lines_ref: List of str
    The X-ray lines for the zeta factors of the reference area.

```

```

Returns:
-----
The zeta factors for the three elements.
'''

zfactors = [0., 0., 0.]
zfactors[lines.index(lines_ref[0])] = known_zeta[0]
zfactors[lines.index(lines_ref[1])] = known_zeta[1]
zeta_unknown, flatness = calculate_unknown_zeta(elements, zfactors,
↪intensities, const_el=constant_element)

return zfactors, flatness

def composition_thickness(s, acquisition_time, probe_current, intensities,
↪zeta_factors, width):
    '''
    Calculates the composition and thickness of the area of interest.
    Parameters:
    -----
    s: The EDX data to be quantified
    acquisition_time: float
        The dwell time of each pixel (can be arbitrary, but same as when calc.
↪zeta factors)
    probe_current: float
        The probe current during the acquisition (can be arbitrary, but same as
↪when calc. zeta factors)
    zeta_factors: list of float
        The zeta factors for the X-ray lines of the elements to be quantified.

    Returns:
    -----
    The composition and thickness of the area of interest.
    '''

    s.set_microscope_parameters(live_time=acquisition_time*width,
↪beam_current=probe_current)
    composition, pt = s.quantification(method='zeta',
                                       intensities=intensities,
                                       factors=zeta_factors,
                                       composition_units='atomic')

    p = hs.material.density_of_mixture(hs.material.
↪atomic_to_weight(composition)) * 1e3
    thickness = pt*1e9/p

    return composition, thickness

```

Modified ICD function

Below is a function “ICD” that takes in a map, and the start and end of the reference area to be used

The function also checks the acceleration voltage in the metadata, in order to extract the correct X-ray line intensities

The function returns all output parameters of interest from the ICD method

This is based on the original code from J. Nilsen (2021), and is modified to better fit this specific work where different lines are used

```
[6]: def ICD(s, ref_area_start, ref_area_end, name):
    width = s.axes_manager[1].size
    s = s.sum(axis=1)
    Vacc= s.metadata.Acquisition_instrument.TEM.beam_energy

    #####
    #                               Add these code lines for denoising:           #
    #####
    #s.change_dtype('float') #
    #s.decomposition(normalize_poissonian_noise=True) #
    #s.plot_explained_variance_ratio() #
    #PCA_index = 4 #
    #s = s.get_decomposition_model(PCA_index) #
    #####

    if Vacc > 13:
        constant_element = 'Ga' # The element for which the composition is
        →constant over the scanned area
        unknown_zeta = 'Sb' # The element for which there is no internal
        →reference
        probe_current = 0.692 # nA (Can be arbitrary)
        acquisition_time = 0.1 # s (Can be arbitrary)
        elements = ['As', 'Ga', 'Sb'] # The elements of the area of interest
        lines = ['As_Ka', 'Ga_Ka', 'Sb_La'] # The X-ray lines used for
        →quantification

        comp_ref = hs.material.atomic_to_weight([0.5, 0.5], ("As", "Ga"))/100 #
        →Composition of ref. area in wt.%
        density_ref = hs.material.density_of_mixture(comp_ref, ("As", "Ga")) *
        →1e3 # Density of ref. in kg/m^2
        lines_ref = ["As_Ka", "Ga_Ka"] # The X-ray lines used in the reference
        →area
        thickness = 45 # nm (Can be arbitrary)
```

```

    ref_area = s.inav[ref_area_start:ref_area_end] # The pixels in the data
↳set to be used as a reference area.
    length = ref_area.axes_manager[0].size
    ref_area = ref_area.sum()
    ref_area.metadata.Sample.xray_lines = lines_ref
    bw_As_ref = ref_area.estimate_background_windows(line_width=[3,1.5],
↳windows_width=1, xray_lines=['As_Ka'])
    bw_Ga_ref = ref_area.estimate_background_windows(line_width=[3.5,4],
↳windows_width=1, xray_lines=['Ga_Ka'])
    BW_ref = np.concatenate((bw_As_ref, bw_Ga_ref)) # must be in
↳alphabetical order
    #ref_area.plot(background_windows=BW_ref)
    ref_area_ints = ref_area.get_lines_intensity(lines = lines_ref,
                                                background_windows=BW_ref,
                                                integrations_windows=1.2)

    s.add_lines(lines)
    s.metadata.Sample.xray_lines = lines
    bw_1 = s.estimate_background_windows(line_width=[3,1.5],
↳windows_width=1, xray_lines=['As_Ka'])
    bw_2 = s.estimate_background_windows(line_width=[3.5,4],
↳windows_width=1, xray_lines=['Ga_Ka'])
    bw_3 = s.estimate_background_windows(line_width=[3,4], windows_width=1,
↳xray_lines=['Sb_La'])
    BW = np.concatenate((bw_1, bw_2, bw_3))
    #s.plot(background_windows=BW)
    s_ints = s.get_lines_intensity(background_windows=BW,
↳integrations_windows=1.2)

    if Vacc < 13:
        constant_element = 'Ga' # The element for which the composition is
↳constant over the scanned area
        unknown_zeta = 'Sb' # The element for which there is no internal
↳reference
        probe_current = 0.692 # nA (Can be arbitrary)
        acquisition_time = 0.1 # s (Can be arbitrary)
        elements = ['As', 'Ga', 'Sb'] # The elements of the area of interest
        lines = ['As_La', 'Ga_La', 'Sb_La'] # The X-ray lines used for
↳quantification

        comp_ref = hs.material.atomic_to_weight([0.5, 0.5], ("As", "Ga"))/100 #
↳Composition of ref. area in wt.%
        density_ref = hs.material.density_of_mixture(comp_ref, ("As", "Ga")) *
↳1e3 # Density of ref. in kg/m^2
        lines_ref = ["As_La", "Ga_La"] # The X-ray lines used in the reference
↳area

```

```

thickness = 45 # nm (Can be arbitrary)

ref_area = s.inav[ref_area_start:ref_area_end] # The pixels in the data
↳set to be used as a reference area.
length = ref_area.axes_manager[0].size
ref_area = ref_area.sum()
ref_area.metadata.Sample.xray_lines = lines_ref
bw_As_ref = ref_area.estimate_background_windows(line_width=[0.9,1.6],
↳windows_width=0.2, xray_lines=['As_La'])
bw_Ga_ref = ref_area.estimate_background_windows(line_width=[1.1,1.3],
↳windows_width=0.2, xray_lines=['Ga_La'])
BW_ref = np.concatenate((bw_As_ref, bw_Ga_ref)) # must be in
↳alphabetical order
#ref_area.plot(background_windows=BW_ref)
ref_area_ints = ref_area.get_lines_intensity(lines = lines_ref,
                                             background_windows=BW_ref,
                                             integrations_windows=1.2)

s.add_lines(lines)
s.metadata.Sample.xray_lines = lines
bw_1 = s.estimate_background_windows(line_width=[0.9,1.6],
↳windows_width=0.2, xray_lines=['As_La'])
bw_2 = s.estimate_background_windows(line_width=[1.1,1.3],
↳windows_width=0.2, xray_lines=['Ga_La'])
bw_3 = s.estimate_background_windows(line_width=[3,4], windows_width=1,
↳xray_lines=['Sb_La'])
BW = np.concatenate((bw_1, bw_2, bw_3)) # must be in alphabetical order
#s.plot(background_windows=BW)
s_ints = s.get_lines_intensity(background_windows=BW,
↳integrations_windows=1.2)

zeta_from_reference = find_zeta_from_reference(ref_area,
                                             ref_area_ints,
                                             acquisition_time,
                                             probe_current,
                                             thickness,
                                             density_ref,
                                             comp_ref,
                                             width,
                                             length)

known_zeta = []
for j in range(len(zeta_from_reference)):
    known_zeta.append(zeta_from_reference[j][0])

```

```

print("Calculating zetafactors for spectrum: " + name)
zeta_factors, flatness = find_unknown_zeta(s_ints,
                                          elements,
                                          constant_element,
                                          known_zeta,
                                          lines_ref,
                                          lines,
                                          constant_element)

composition, thickness = composition_thickness(s,
                                              acquisition_time,
                                              probe_current,
                                              s_ints,
                                              zeta_factors,
                                              width)

quant = s.quantification(s_ints, method = "CL", factors = k_vector[Vacc])
As_atomic, Ga_atomic, Sb_atomic = quant[0].data, quant[1].data, quant[2].data

return composition, thickness, quant, zeta_factors, flatness

```

Run dataset through ICD function

```
[7]: composition, thickness, quant, zeta_factors, flatness = ICD(s_9000_30kV_8tilt_0,
→0.0, 200.0, spectra_name)
```

Calculating zetafactors for spectrum: 30kV 8 tilt

Initial flatness: 0.05970087799144047

The zeta factor for Sb was determined to be 394.9271702536799 with a flatness criterion of 4.6 at.%.

Below is code to save the output parameters to a csv file if nesecary (handy when processing many datasets)

```
[8]: df = pd.DataFrame({"Parameter": ["Z As", "Z_Ga", "Z_Sb", "Sb max ICD", "Sb max_I
→CL", "Flatness"]})
df.to_csv("ICD_parameters.csv", index = False)
```

```
[9]: df = pd.read_csv("ICD_parameters.csv")
Z_As = zeta_factors[0]
Z_Ga = zeta_factors[1]
Z_Sb = zeta_factors[2]
Sb_max_ICD = max(composition[2].data)
Sb_max_CL = max(quant[2].data)
d_C_Ga = flatness
df[spectra_name] = [Z_As, Z_Ga, Z_Sb, Sb_max_ICD, Sb_max_CL, d_C_Ga]
```

[10]: df

```
[10]:      Parameter 30kV 8 tilt
0      Z As      782.427402
1      Z_Ga      499.275816
2      Z_Sb      394.927170
3  Sb max ICD      5.201364
4  Sb max CL      4.723379
5  Flatness      0.046000
```

[]:

B | Appendix

B.1 Concentration profiles from SU9000 denoised using PCA

All the EDS data from the axial GaAsSb heterostructured NWs studied in this work (see Sec. 4.2.2) were calculated again, but with denoising before applying ICD and Cliff-Lorimer analysis to the data. The results form the exact same measurement series as seen in Fig. 4.9 and 4.10 is seen below in Fig. B.1 and B.2 respectively. Additionally, all the relevant output parameters from the ICD method is seen below in Tab. B.1 for the denoised data. Here, the values calculated on the raw data from Tab. 4.3 is also given below for easier comparison.

It is observed that the concentration profiles are significantly smoother, and that the final flatness has been significantly reduced. This indicates that the implementation of a flatness criteria for a benchmark element has worked as intended compared to the noisy raw data. Additionally, the periodic variations in Ga in phase with the Sb profile as expected from J. Nilsen data is observed to some degree, especially in profiles at 30 kV. The maximum Sb concentration values are also more stable compared to the raw data, disregarding 10 kV at 8° tilt and 5 kv at 20° tilt.

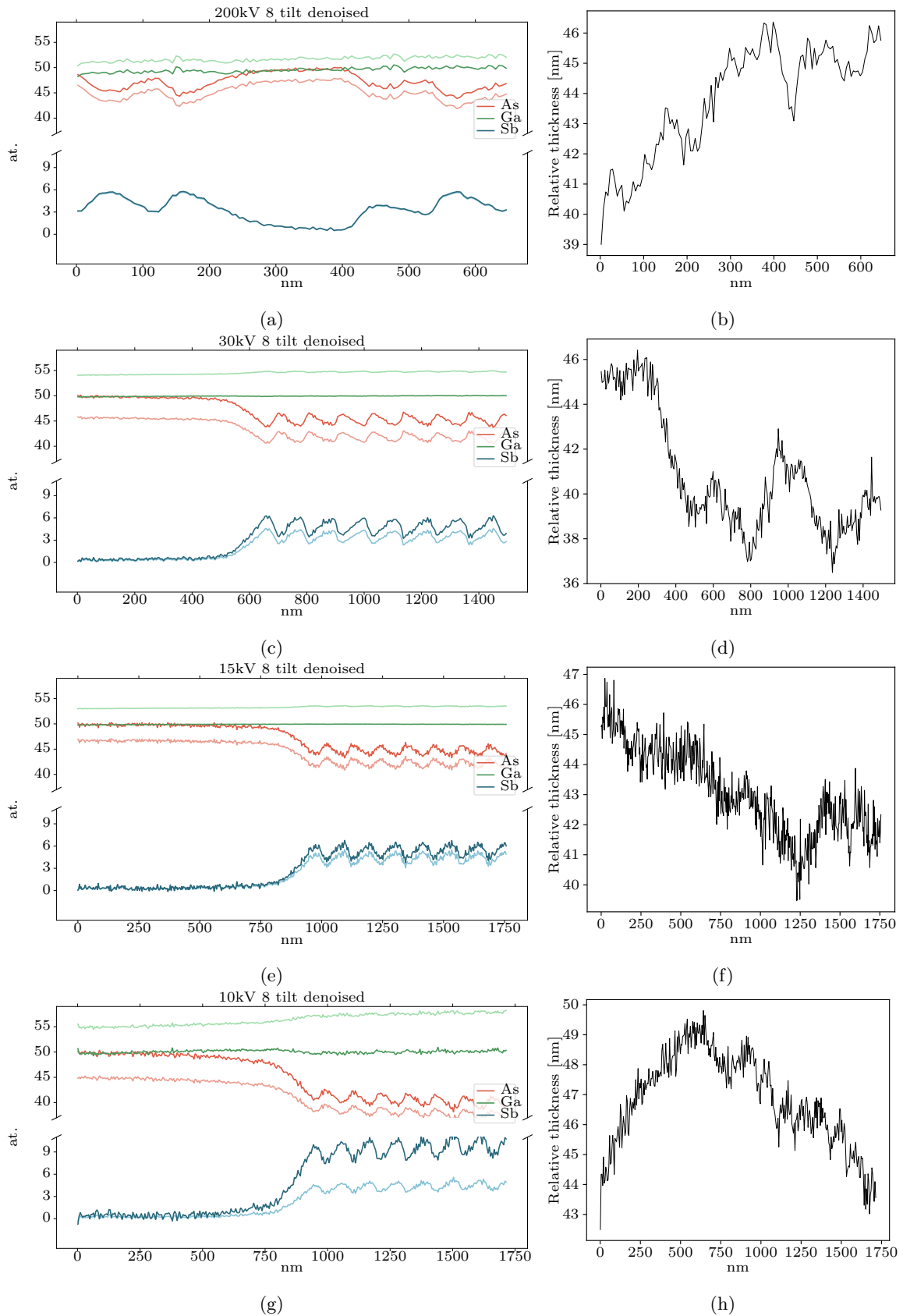


Figure B.1: Concentration profiles using the same EDS data as in Fig. 4.9, but denoised using PCA before applying ICD method. (a,c,e,g) Concentration profiles of As (red) Ga (green) and Sb(blue) for both Internal Composition determination (bold) and Cliff-Lorimer (weak). (b,d,f,h) Relative thickness profiles calculated using ICD.

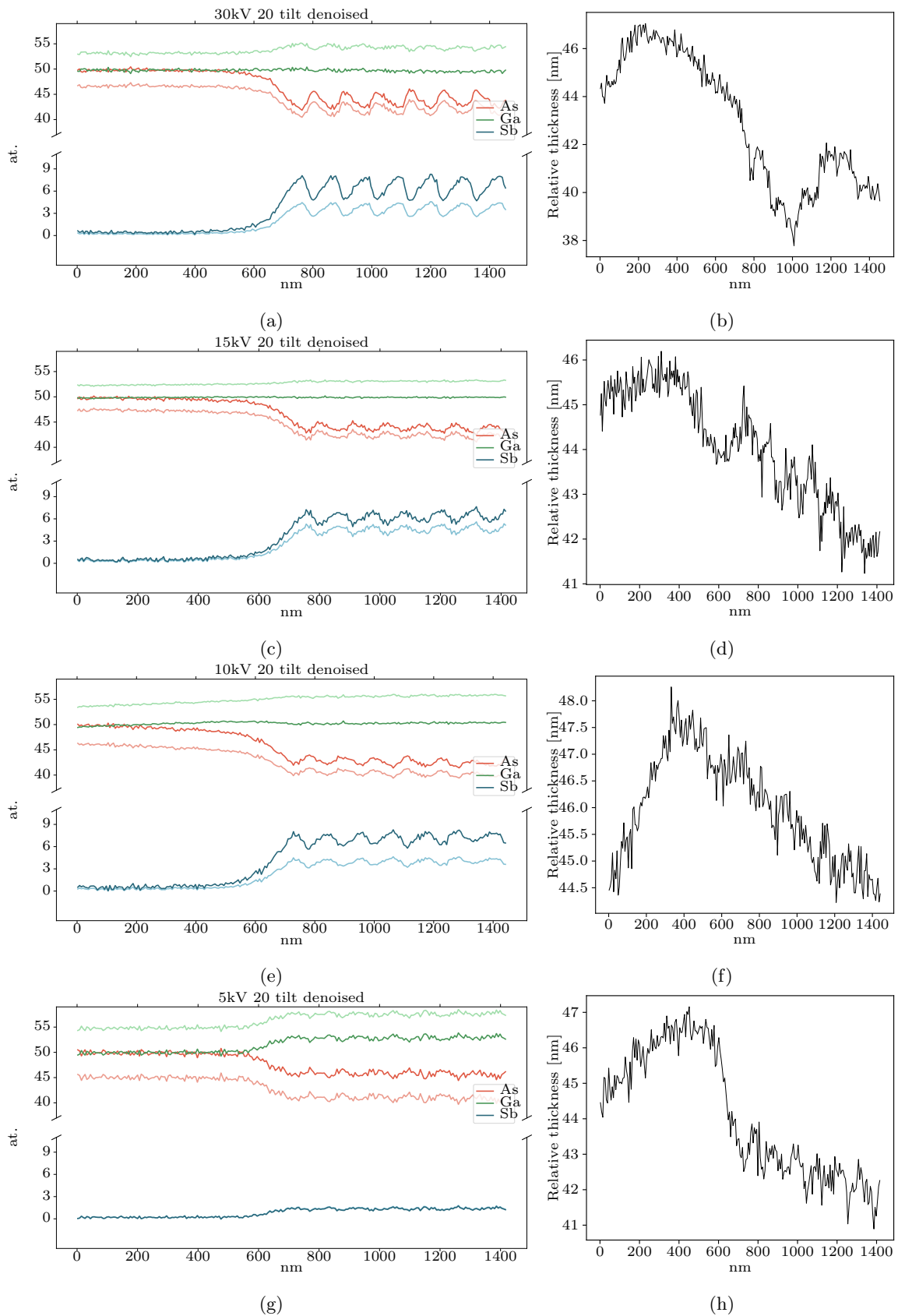


Figure B.2: Concentration profiles using the same EDS data as in Fig. 4.10, but denoised using PCA before applying ICD method. (a,c,e,g) Concentration profiles of As (red) Ga (green) and Sb(blue) for both Internal Composition determination (bold) and Cliff-Lorimer (weak). (b,d,f,h) Relative thickness profiles calculated using ICD.

Table B.1: All relevant parameters from ICD analysis of EDS maps of GaAsSb heterostructured NW, including ζ -factors for all elements, maximum Sb concentration values, C_{Sb} , for both Cliff-Lorimer and ICD, as well as final and initial flatness of benchmark element, ΔC_{Ga} and ΔC_{Ga}^0 respectively. On top is all parameters calculated on denoised data using PCA, and below are values from the raw data as presented in the main text in Tab. 4.3.

Denoised with PCA									
	0 tilt		8 tilt			20 tilt			
	30 kV	200 kV	30 kV	15 kV	10 kV	30 kV	15 kV	10 kV	5 kV
ζ_{As}	1637	152	786	6784	289	497	2775	162	393
ζ_{Ga}	1033	125	500	3275	217	329	1380	128	286
ζ_{Sb}	1178	192	501	1565	1513	436	733	707	2698
$C_{Sb}^{max,ICD}$ [at.%]	7.06	5.78	6.31	6.76	12.00	8.28	7.65	8.27	1.74
$C_{Sb}^{max,C-L}$ [at.%]	4.55	5.66	4.58	5.53	5.58	4.45	5.60	4.63	1.82
ΔC_{Ga} [at.%]	0.8	0.2	0.3	0.2	1.7	1.3	0.6	1.3	4.6
ΔC_{Ga}^0 [at.%]	4.3	3.8	3.5	3.8	7.0	5.1	4.4	5.2	5.6

Raw data									
	0 tilt		8 tilt			20 tilt			
	30 kV	200 kV	30 kV	15 kV	10 kV	30 kV	15 kV	10 kV	5 kV
ζ_{As}	1641	153	782	6785	289	495	2753	162	395
ζ_{Ga}	1028	124	499	3273	217	328	1381	128	291
ζ_{Sb}	1149	176	395	1620	1258	365	637	718	2543
$C_{Sb}^{max,ICD}$ [at.%]	7.13	5.35	5.20	7.89	10.26	7.68	6.94	9.04	3.88
$C_{Sb}^{max,C-L}$ [at.%]	4.70	5.68	4.72	6.25	5.64	4.99	5.77	5.01	4.24
ΔC_{Ga} [at.%]	6.1	3.3	4.6	8.7	4.0	4.5	8.0	3.3	6.9
ΔC_{Ga}^0 [at.%]	7.2	4.6	6.0	11.9	8.3	7.1	10.3	6.5	7.9

B.2 k-factors for Cliff-Lorimer quantification in Aztec

In order to do Cliff-Lorimer quantification in HyperSpy, the built in function requires k-factors as input parameters. k-factors are first of all material specific, but also dependent on instrument settings during data acquisition, especially acceleration voltage. If the user is not experienced with the software, these can be a challenge to find. Therefore, a tutorial of how to find calculated k-factors for all X-ray lines of interest was made during this work, and can be found below. For the X-ray lines relevant to this work, the extracted k-factors at all acceleration voltages used is seen in Tab. B.2

Table B.2: k-factors for X-ray lines relevant to this work. The values are extracted from Aztec software.

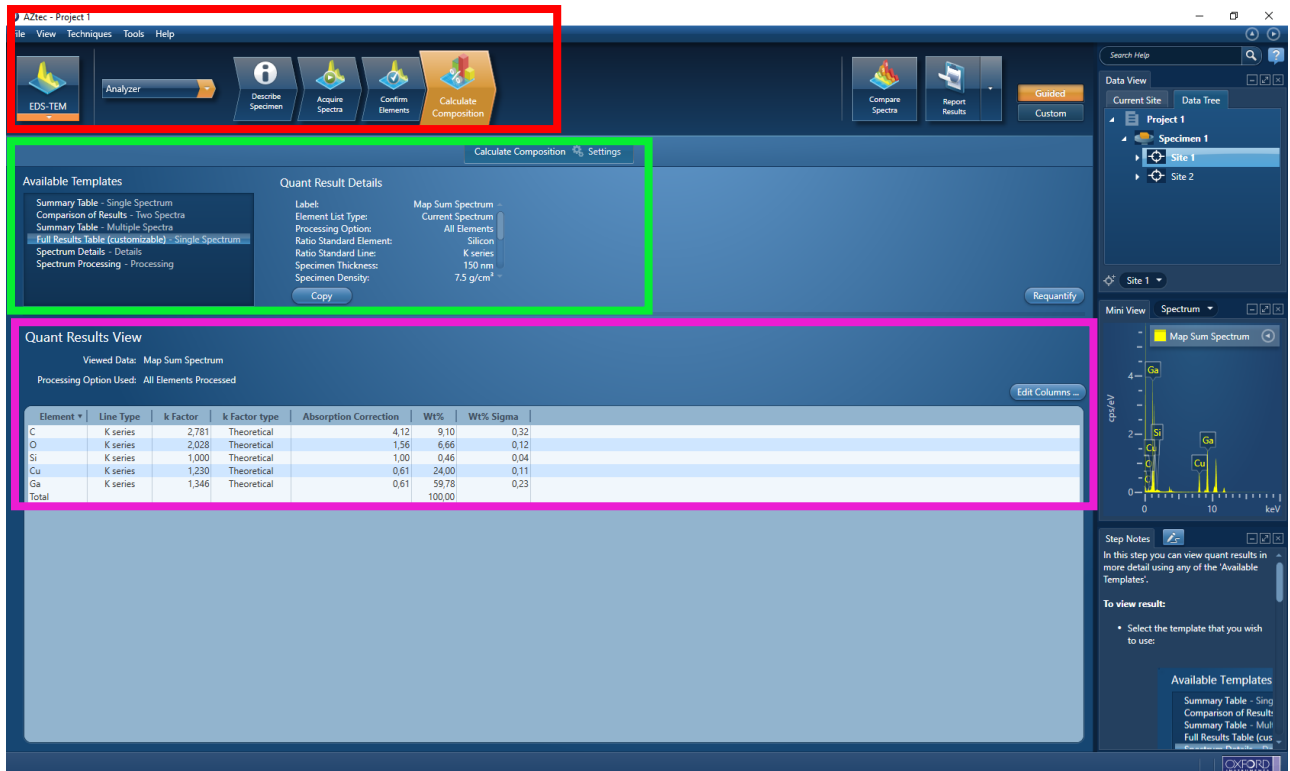
Element	Line	V_{acc} [kV]				
		200	30	15	10	5
Al	K	-	0.980	0.962	0.945	0.890
As	K	1.502	4.618	13.732	-	-
	L	-	-	-	1.281	1.183
Ga	K	1.346	3.484	7.534	-	-
	L	-	-	-	1.178	1.046
Ni	K	1.161	2.359	3.864	-	-
	L	-	-	-	1.027	0.868
O	K	2.028	1.111	1.002	0.917	0.705
Sb	L	1.948	2.307	2.742	3.280	9.234

How to find k-factors in Aztec to use in Cliff-Lorimer quantification

By Mari Sofie Skomedal as a part of Master's thesis

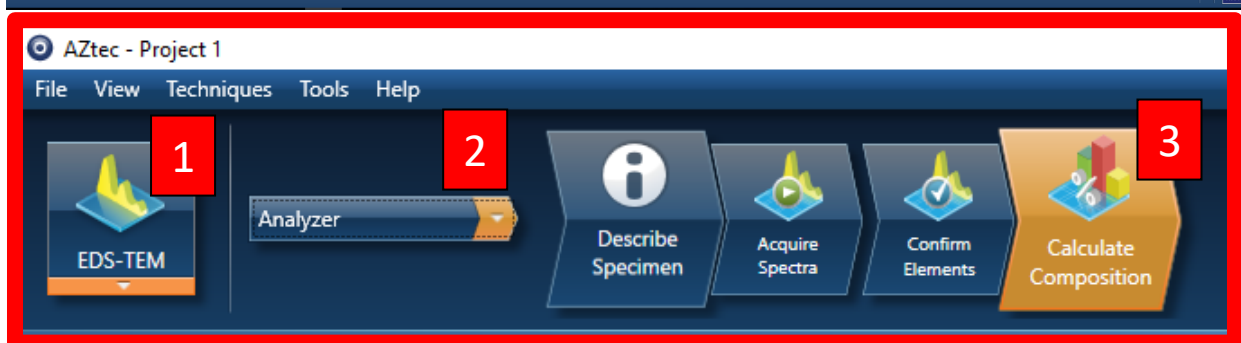
NB! k-factors are dependent on acceleration voltage. The k-factors found using this method will be correct for the acceleration voltage used to record the spectrum/map chosen in the datatree on the right side of the window.

Open a project and follow the instructions below to get k factors from the following window:



The screenshot shows the Aztec software interface. The 'Calculate Composition' window is open, displaying the 'Quant Results View' table. The table is highlighted in pink and contains the following data:

Element	Line Type	k Factor	k Factor type	Absorption Correction	WT%	WT% Sigma
C	K series	2,781	Theoretical	4,12	9,10	0,32
O	K series	2,028	Theoretical	1,56	6,66	0,12
Si	K series	1,000	Theoretical	1,00	0,46	0,04
Cu	K series	1,230	Theoretical	0,61	24,00	0,11
Ga	K series	1,346	Theoretical	0,61	59,78	0,23
Total					100,00	



The screenshot shows the Aztec software interface. The 'EDS-TEM' mode is highlighted with a red box and the number 1. The 'Analyzer' dropdown menu is highlighted with a red box and the number 2. The 'Calculate Composition' button is highlighted with a red box and the number 3.

1. Make sure the **EDS-TEM** mode is chosen. For some instruments (for example the Hitachi SU9000 STEM), the default is often EDS-SEM. Do **NOT** choose EDS-SEM as this will give k-ratios instead, which is not the same as k-factors used in Cliff-Lorimer quantification.
2. Choose **Analyzer** in the roll down menu.
3. Go to **Calculate composition**



4. Choose the **Full Results Table (costumizable)** option in the Available Templates menu
5. Click **Settings** to open the following window where you can choose elements and X-ray lines



6. If the elements of interest are not showing up using the **Current spectrum**, choose **Fixed list**. This way, you can add exactly the elements you want.
7. Click on the element you want the k-factor for.
8. Choose the X-ray line you want to use for quantification
9. Click **Include**
10. Click **Apply and Save** and then **Close** the settings window

Quant Results View

Viewed Data: M

Processing Option Used: A

11

12 Edit Columns ...

Element	Line Type	k Factor	k Factor type	Absorption Correction	Wt%	Wt% Sigma
O	K series	2,028	Theoretical	1,00	2,27	0,04
Ni	K series	1,151	Theoretical	1,00	0,00	0,00
Ga	K series	1,346	Theoretical	1,00	45,94	0,07
As	K series	1,502	Theoretical	1,00	42,74	0,07
Sb	L series	1,948	Theoretical	1,00	9,04	0,06
Total					100,00	

11. The k-factors can be seen in the Quant results view.
12. However, if the k-factors are not showing, click the **Edit Columns** button to open the window below:

Quant Table Layout Edi...

Column Name	Show Column
Line Type	<input checked="" type="checkbox"/>
k Factor	<input checked="" type="checkbox"/>
k Factor type	<input checked="" type="checkbox"/>
Absorption Correction	<input checked="" type="checkbox"/>
Wt%	<input checked="" type="checkbox"/>
Wt% Sigma	<input checked="" type="checkbox"/>
Atomic %	<input type="checkbox"/>
Oxide	<input type="checkbox"/>
Oxide %	<input type="checkbox"/>
Number of Ions	<input type="checkbox"/>
Type of Ion	<input type="checkbox"/>
Mass/Unit Area ($\mu\text{g}/\text{cm}^2$)	<input type="checkbox"/>
Mass/Unit Area Sigma ($\mu\text{g}/\text{cm}^2$)	<input type="checkbox"/>

13

13. Make sure k Factor column is chosen under **Show Column**. Choose any other columns that may be of interest.

